FORCES IN CYTOSKELETAL SYSTEMS

by

Sreeja B. Asokan

A dissertation submitted to the University of North Carolina at Chapel Hill in partial fulfillment of the requirements for the degree of Doctor of Philosophy in the Department of Physics and Astronomy.

Chapel Hill

2006

Approved by

Advisor: R. Superfine, Ph.D.

Reader: S. Washburn, Ph.D.

Reader: R. E. Cheney, Ph.D.

Reader: E. D. Salmon, Ph.D.

Reader: P. H. Tiesinga, Ph.D.

ABSTRACT

Sreeja B. Asokan: Forces in Cytoskeletal Systems (Under the direction of R. Superfine, Ph.D.)

       Force is fundamental to all biological systems, from the molecular level in cells to the complex organism. These forces are generated by the cytoskeleton alone or in conjunction with motor proteins, by utilizing ATP and GTP as fuels. This study investigates novel techniques to manipulate cytoskeletal systems to understand these forces, and, investigate the effect of physiologically relevant forces on these systems. Dielectrophoresis, the movement of polarizable particles in an electric field gradient was used to pattern the deposition of actin filaments, and, organize the random movement of actin filaments on myosin V motor protein to a collimated movement. Microfluidic channels were then used independent of the above to apply flow induced force and torque to actin filaments during motility. These experiments showed that forces significantly lower than motor forces can generate torques on the filaments and steer them during motility. Further, torque due to flow on actin filaments was shown to be capable of polarizing randomly aligned filaments during motility. Finally, we investigate a new approach of using rod shaped particles as microrheological probes. Viscosity of Newtonian fluids measured with nano rods were in good agreement with expected viscosity values and hence validate this approach. In complex

solutions, the measured values deviated from expected values leading us to conclude that there is a shape and size dependant interaction between the mesh network of complex fluids and rod shaped particles. This has implications to how the cytoplasm, a complex fluid, affects cytoskeletal and organelle organization, restricts DNA mobility during gene delivery and motility of rod shaped pathogen within cells.

To my parents,

Dr. and Mrs. Padmanabhan

and my husband, Aravind Asokan

for their love, encouragement, and support

ACKNOWLEDGEMENTS

The successful completion of this thesis required the support and encouragement of many. First, I would like to express my deep and sincere gratitude to my advisor, Dr. Richard Superfine for his support and advice. His rigor and passion for science will have a permanent influence on my approach to life. I am also indebted to my committee members, Drs. Washburn, Salmon, Cheney, and Tiesinga for their guidance and encouragement. It is an honor to have worked under the combined mentorship of experts in different aspects of science. I also wish to thank the faculty and staff of the department of Physics and Astronomy, especially, Ms. Maggie Hudson for their support.

I wish to extend my sincere thanks to the network of support I relied on throughout grad school – the members of the Nano Science Research group. In particular, I want to thank Jeremy Cribb, Adam Hall, Lloyd Carroll, Lolo Jawerth, Atsuko Negishi, Jay Fisher and Ben Wilde for all the scientific discussions and fun times.

Finally I would like to thank my family: my mother Usha, whose boundless energy inspires me, my father Raju who taught me how to balance work and play, my siblings (Krishnan and Poornima) for encouraging me and my dear husband Aravind for supporting and guiding me through my entire graduate life.

TABLE OF CONTENTS

CHAPTER

CHAPTER I

INTRODUCTION

1. Introduction

Motility is one of the crowning achievements of evolution. This motion, at all length scales, from a molecule to the organism, is due to forces. Primitive cells probably relied on diffusion to distribute metabolites. But as the cell evolved to perform more elaborate and sophisticated functions, the need for a well developed transportation system to move materials within the cell grew. Molecular forces generated by filaments and motor proteins control biochemical traffic inside the cell and connect the cell with the outside through the membrane. Cells exhibit dramatic changes in their morphology by pushing against their own membranes to form microvilli and filopodia, peeling and pulling against surroundings to search and defend the body against foreign organisms, swimming with engineered actuating structures like cilia. The replication of a cell, involving chromosomes and filaments, arises from the coordinated movement between the restructuring affects of molecular forces and the biochemical force sensors that stop and start different stages of cell division. The concerted and synchronized movement of thousands of molecular motors within the cilia oscillates it to cause the flow of the pulmonary barrier fluid over long distances. Within organisms, cells cause fluids to flow transporting nutrients and flushing barrier layers. The organization and motion of tissue is dictated by the motion of cells, and their ability to generate and respond to forces.

Movement is a manifestation of mechanical work, which requires a fuel (ATP) and a mechano-chemical enzyme that converts the energy to motion. Also, a very important player in motility is the cytoskeleton, a dynamic system of fibers that form the structural framework of the cell, act as tracks along which organelles and motor proteins move, and by themselves generate forces by polymerization.

2. Actin microfilaments

The cytoskeleton is a network of 3 types of fibers: microfilaments, intermediate filaments and microtubules. Actin microfilaments are central to almost every type of motility from cell migration to cytosol transport. Actin filaments serve many cellular functions including transmitting internal stresses, providing mechanical strength to the cell cortex, regulating enzymatic activities, and spatially organizing the cytoplasm and signal transduction pathways (Elson, 1988; Evans, 1993; Janmey, 1998). Actin was first identified as part of the acto-myosin protein complex responsible for producing the contractile force in skeletal muscle (Straub, 1942). One of the earliest recognized functions of actin is to assemble into linear polymers that in muscle form the thin filaments of the sarcomere. In other cell types actin assembles into a variety of structures including isotropic networks of filaments within the cytoskeleton, contractile actin filament bundles often called stress fibers, highly organized parallel arrays of filaments in such structures as microvilli and the thin protrusions of hair cells in the cochlea, as well as small oligomeric or monomeric particles and protein complexes in the cytoplasm.

Actin exists as a globular monomer called *G-actin* and a filamentous polymer called *F-actin*. G-actin has a MW of 43 kDa and X-ray diffraction studies of G-actin reveal that the monomer is asymmetric and contains two lobes separated by a cleft that consists of an ATP and Mg_2^+ binding site. The assembly of G-actin to F-actin is accompanied by the hydrolysis of ATP to ADP and P_i, ATP hydrolysis, however is not necessary for polymerization to occur, but does affect the kinetics. It is the presence of ions (Mg_2^+, K^+, Na^+) in a solution of G-actin that triggers the polymerization process to form F-actin filaments (figure 1.1).
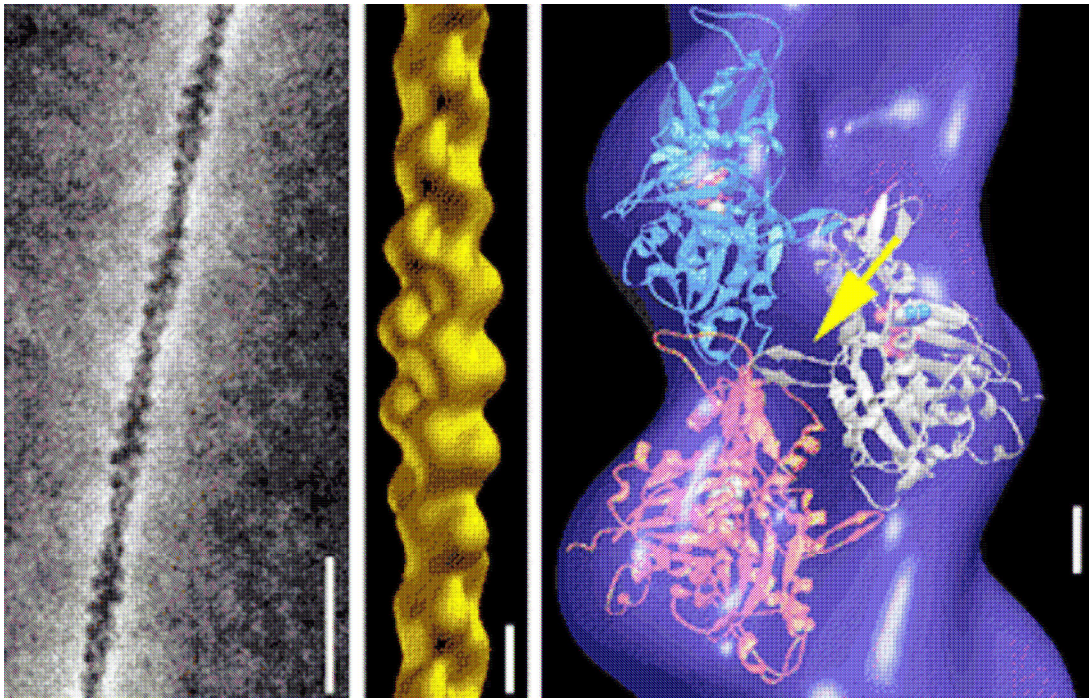
Figure 1.1. The structure of the actin monomer obtained from the actin-DNAse-1 crystal is superimposed on the density map of the actin filament derived from X-ray diffraction and EM. Derived from www.mih.unibas.ch/Homepages/stoffler/Slides/Actin/Actin.html.

The above process can be reversed by reducing the ionic strength of the solution and it is this reversible assembly that lies at the core of many forms of motility. The structural asymmetry of the monomer and the head-to tail polymerization ensure the filament is asymmetric and has a structural polarity. This feature was first recognized by the appearance in EM of F-actin bound to saturation by the myosin S1 fragment. Such S1 decorated filaments have an arrowhead appearance in negative stain preparations and from this appearance the terms barbed and pointed end were derived to identify the two filament ends. Under conditions where ATP-actin polymerizes, the net rates of addition and dissociation are different at the two ends. G-actin containing ATP binds to the preferred filament end, and the ATP is hydrolyzed to ADP with phosphate still bound to the actin, followed by release of the

phosphate to form a mixture of ADP-actin and ADP-Pi actin subunits within the filament. At the end of the filament with lower affinity for polymerization, actin subunits contain primarily ADP, and at steady state, the net rate of disassembly matches the rate of assembly at the barbed end. Observing the growth of actin from the two ends of decorated filaments where the two ends could be discerned showed that the barbed filament end is the preferred end for assembly (Kondo and Ishiwata, 1976) and in the presence of ATP has a 12 fold higher affinity for actin subunits that the pointed end (Wegner and Isenberg, 1983). X-ray diffraction and Electron microscopy of F-actin filaments have revealed that this long flexible filament is of 7-9 nm diameter and is a helix with a repeat length of 36 nm.

F-actin filaments *in vivo* and *in vitro* are typically micrometers long, and therefore have a high aspect ratio. A filament can hence have many physical deformations at scales far above the monomeric scale. To model these deformations, one can neglect the helical character of the filament and model it as a semi flexible homogeneous cylinder. Even though the conformation of least elastic energy for the semi flexible filament would be completely straight, at finite temperatures the average conformation of the molecule is curved due to the random thermal forces exerted by the solvent. An important feature of microscopic structures such as actin in aqueous solutions is thermally excited motions. The conventional measure of the degree of thermal flexing of a polymer is the persistence length (Landau et al., 1980). The persistence length lp is defined by the correlation function (Eq. 1.1) as the characteristic distance along the polymer chain over which the directions of unit vectors u (s) drawn tangent to the polymer contour become uncorrelated.

$$\langle u(s) \bullet u(0) \rangle = e^{-\frac{s}{l_p}} \ [1.1]$$

where $<>$ denotes the time average over thermal fluctuations, and s is the distance along the contour of the chain, measured from some arbitrary point $s = 0$ (figure 1.2).
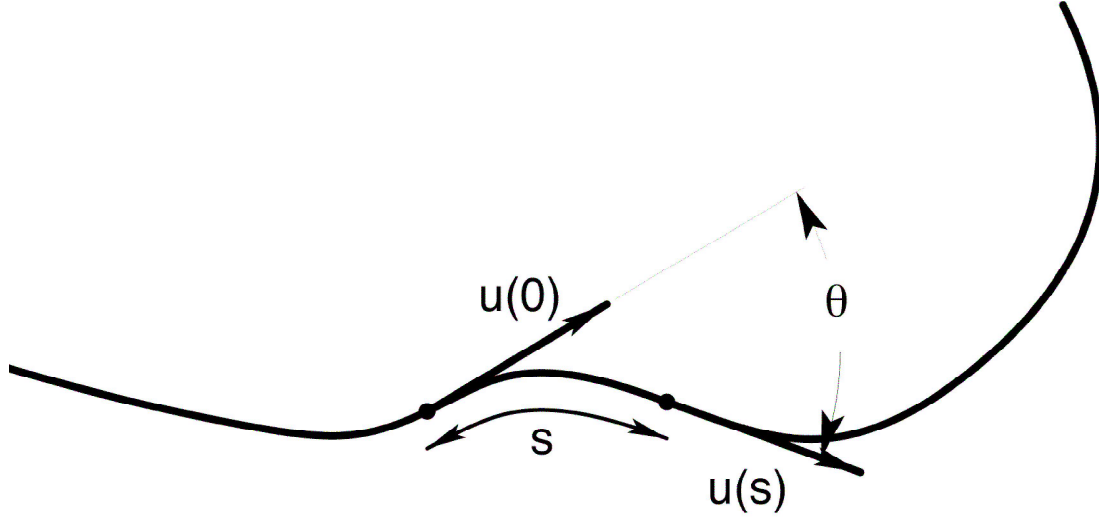
Figure 1.2. Unit vectors u (s) drawn tangent to the polymer contour. Persistence length is the characteristic length beyond which the tangent vectors become uncorrelated.

The persistence length is also related to the Young's modulus of the filament (Eq. 1.2).

$$l_p = \frac{EI}{k_B T} \quad [1.2]$$

Here, E is the Young's modulus of the filament, and I is the moment of inertia, k_B the Boltzmann constant and T the temperature. Conversely, the persistence length is roughly the length over which a filament appears straight. Most measures of lp for F-actin are in the range of 3-18 μm (Gittes et al., 1993), and the typical length of an actin filament in vitro is from 1 - 20 μm compared to a diameter of 8 nm.

Not only does actin provide a lattice to support the plasma membrane, its ability to polymerize is harnessed by the cell to generate many forms of motility. The force generated

within the cell by polymerization and depolymerization of actin alone results in several types of cell movements. Actin polymerization at the leading end of migrating cells produces changes in the position of the plasma membrane causing the cell to move. In addition, the actin filaments are rapidly cross-linked into bundles and networks at the leading edge in the filopodia and lamellipodia. These structures prevent the membrane from retracting by forming stable contacts with surfaces.

3. Myosin: Actin activated ATP-ase

Actin does not function alone to perform some important types of motility. Myosin, an actin activated ATPase that moves along actin filaments is known or hypothesized to play fundamental roles in many forms of eukaryotic motility such as cell crawling, cytokinesis, phagocytosis, growth cone extension, maintenance of cell shape, and organelle/particle trafficking. Members of the myosin superfamily are defined by the presence of a heavy chain with a conserved ~80 kDa catalytic domain. In most myosins, the catalytic domain is followed by an α-helical light chain-binding region consisting of one or more IQ motifs. Most myosins also have a C-terminal tail and/or an N-terminal extension thought to endow class-specific properties such as membrane binding or kinase. Phylogenetic analysis has so far identified eighteen distinct classes of myosin based on their activity (figure 1.3) (Berg et al., 2001).
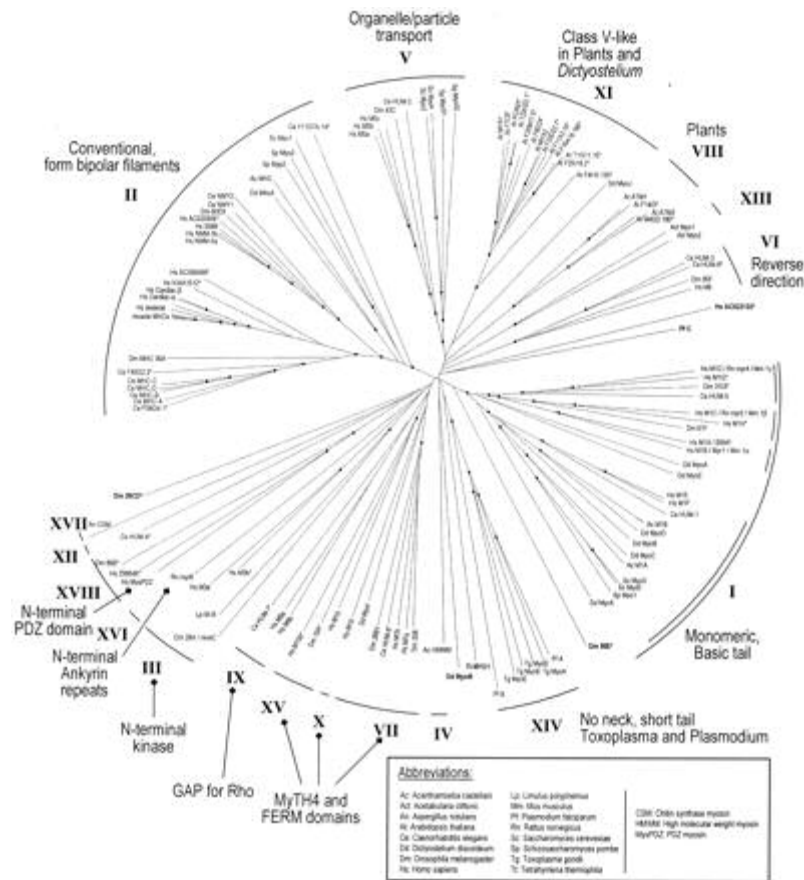
Figure 1.3. An unrooted phylogenetic tree of the myosin superfamily. This tree was assembled using myosin head domain protein sequences from all currently known or predicted myosins in humans, *Drosophila*, *C. elegans*, *Dictyostelium*, *Arabidopsis*, *S. cerevisiae*, and *S. pombe*, as well as selected myosins from other organisms. (source: Berg et al., 2001)

Myosin II, the conventional myosin which was the first one discovered is responsible for skeletal muscle contraction. The characteristic feature of these myosins is their helical coiled coil tails that self assemble to form a variety of filament structures (bipolar or side polar filaments) that are essential for their function. In muscle cells, it is myosin II that is responsible for producing the contractile force. Here, the long coiled-coil tails of the individual myosin molecules join together, forming the thick filaments of the sarcomere. The

force-producing head domains stick out from the side of the thick filament, ready to walk along the adjacent actin-based thin filaments in response to the proper chemical signals. Apart from muscle contraction, myosin II is required for cytokinesis, cell motility, cell polarity/chemotaxis, maintaining cell architecture and development in nonmuscle cells.

3.1 Myosin V

Myosin V was first identified in actomyosin precipitates from brain tissue as a 190 kDa calmodulin-binding protein that exhibits all of the expected enzymatic properties of a myosin molecule, in that it has actin-stimulated Mg-ATPase activity and is a barbed-end-directed motor capable of moving actin filaments at rates of up to 400 nm/s. Myosin V is actually an oligomer comprising of two ~190 kDa 'heavy chain' subunits and twelve low molecular weight subunits (light chains). The light chains bind to six IQ motifs in the neck region of each heavy chain, and the heads of the heavy chains are correspondingly elongated relative to those of myosin II. The tail region of the myosin V heavy chain has a central coiled-coil domain that presumably promotes dimer formation followed by a globular domain. Unlike myosin II, myosin V does not appear to form filaments. Myosin-V molecules consist of two heads attached to a ~30 nm stalk that ends in a globular region. Myosin V HMM was observed by Walker et al. using EM (Figure 1.4).
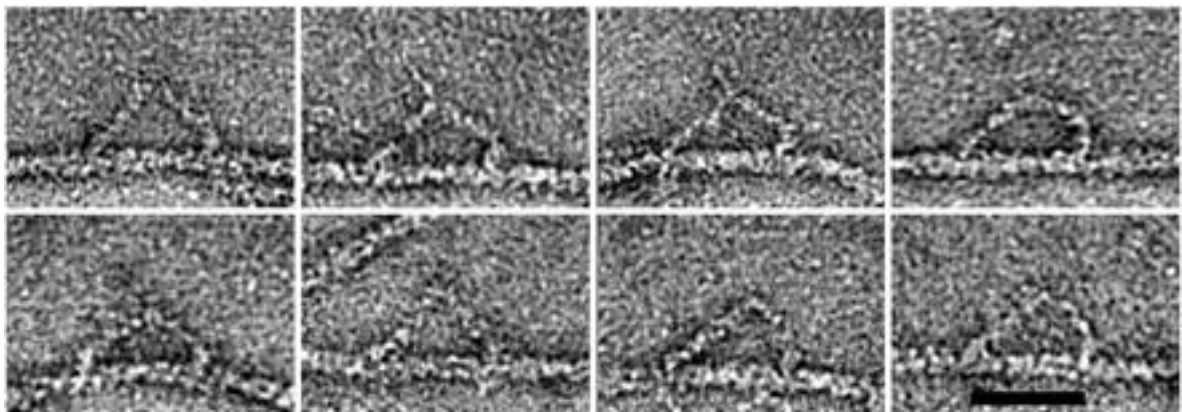
**Figure 1.4.** Single myosin V HMM "walking" on actin filaments seen by EM (source: Walker et al., 2000).

AFM imaging of myosin V estimates the motor to extend to ~ 120 nm in height (Ando, 2001). Each myosin-V heavy chain is associated with approximately four calmodulin light chains as well as two less abundant proteins of 23 and 17 kDa (Cheney et al., 1993). Mehta et al. in 1999 observed that myosin-V is a processive actin-based motor just like Kinesin (Mehta et al., 1999). Processivity means that the motor undergoes multiple catalytic cycles and coupled mechanical advances for each diffusional encounter with its track. This allows single motors to support movement of an organelle along its track. It can move in large steps approximating the 36 nm pseudo-repeat of the actin filament applying force of 3 pN per motor. This step size is much higher when compared to the 8nm step size for kinesin. Recently Yildiz et al. showed that myosin V moves in a hand-over-hand model of motility, not an inchworm model (Yildiz et al., 2003).

3.2 Motility assay

The properties of biomotors are typically studied by performing invitro motility assays of the motor and its associated filament. There are two orientations in which these motors can sustain motility. In one, the filaments are attached to the surface and the motors usually bound to beads move along the filaments similar to that in vivo. This is termed the 'bead assay'. The motor can be manipulated by applying force to the bead through a laser or magnetic trap. In the other configuration, the motors are adsorbed to the surface and the filaments slide on the lawn of motors. This is termed the 'gliding filament' or the 'sliding filament assay'. We used the second configuration in our experiments and describe it in detail in the methods section of the later chapters.

4. Microtubules

The microtubule is another important cytoskeletal filament responsible for cell movements like beating of cilia and flagella, transport of membrane vesicles, cell division and axonal growth. All these movements are a result either of microtubule dynamics alone or produced in conjunction with associated motors like kinesin and dynein. Microtubules are polymers of heterodimers of globular α-tubulin and β-tubulin monomers which have a molecular mass of about 50,000. During polymerization, GTP bound to β-tubulin is hydrolyzed (David-Pfeuty et al., 1977; MacNeal & Purich, 1978). α -tubulin also binds GTP, but this GTP is not hydrolyzed during polymerization (Spiegelman et al., 1977). Within a MT, tubulin heterodimers are arranged in linear protofilaments that associate laterally to form 24 nm wide hollow cylindrical polymers. MT's in vivo have predominantly 13 protofilaments (Evans et al., 1985) (figure 1.5). MTs are polar structures formed by the head-to-tail association of αβ-heterodimers (Amos and Klug, 1974). The different polymerization rates of the two ends of the MT are a consequence of this polarity; the faster growing end is referred to as the plus end and the slower growing end as the minus end (Allen and Borisy, 1974). The polarity of the MT lattice is also central to the function of MT motor proteins of the kinesin (Vale and Fletterick, 1997) and dynein (Hyams and Lloyd, 1994) families, which utilize the energy of ATP hydrolysis to move unidirectionally along the MT.
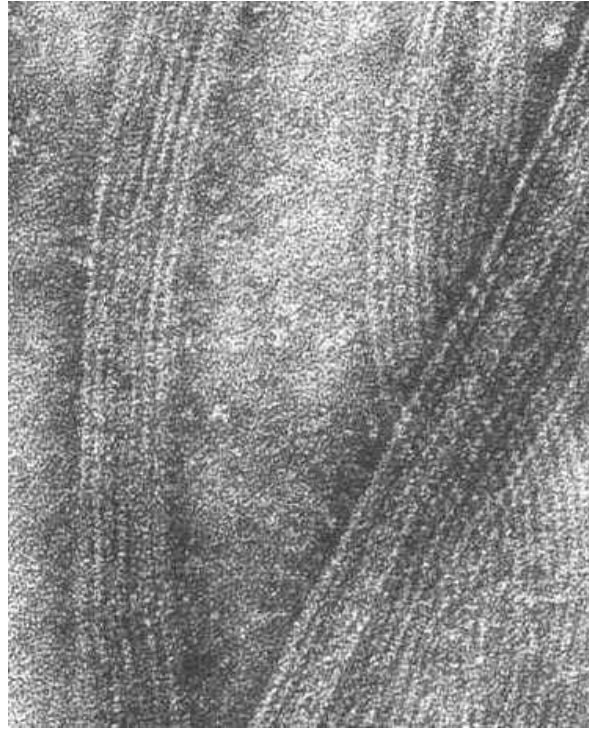
Figure1.5. Microtubules can be seen in a bundle in this negatively stained preparation. Then heavy metal stain is deposited around the structures, delineating their structure. This preparation may allow you to see the tubulin molecules in the protofilaments. (Taken from Bloom and Fawcett; Textbook of Histology)

Within each protofilament, αβ heterodimers are oriented with their β-tubulin monomer pointing toward the plus end of the MT. Therefore, β-tubulin is exposed at the plus end and α-tubulin is exposed at the minus end of the MT. Microtubules show dynamic instability. Individual microtubules exhibit alternating phases of elongation and rapid shortening. Transitions between these phases are abrupt, stochastic, and infrequent in comparison to the rates of tubulin association and dissociation at the microtubule ends. This property is extremely important in processes like cell division, where, microtubules go from the polymerizing phase to the depolymerizing phase thereby separating the sister chromatids. Microtubules can grow up to hundreds of microns long in vivo. They are much stiffer than

the actin filaments because of their tube like construction. Their persistence length has beenmeasured to be as high as 5 mm (Gittes et al., 1993)

5. Force technologies

For studying biology at the molecular scale, there is a need to develop new force technologies, data analysis and interpretation techniques, and new model building with data comparison. Several techniques have been developed for measuring the forces generated by specific molecular mechanisms, and for measuring the general rheological properties of media that determine their response to these forces. For force measurements involving molecular motors, spindles or flagella, techniques used include laser tweezers and microneedles. Laser tweezers have provided remarkable insight into single molecule force generation, but is limited by the inability to focus the trap tightly in microscale systems, and its application in biological fluids where the trap can be loaded by extraneous proteins and macromolecules. Microneedles can be limited by their invasiveness and the lack of general applicability. High sensitivity is usually limited to single direction. Atomic Force Microscopy has been used to image atoms of hard surfaces, has 1 nm resolution on packed arrays of proteins and long molecules. In addition to imaging, AFM has been applied to measure the force response of single biological molecules, including titin, fibronectin and DNA. Recently, magnetic traps have been used to measure the viscoelastic properties of cells and actin networks with demonstrated forces of over 8 nN.

5.1 Dielectrophoresis

We first used dielectrophoresis to apply forces and torques to actin filaments by themselves, and during sliding motility on myosin V (**Chapter II**). Dielectrophoresis (DEP), the motion of polarized particles in a non-uniform electric field was first discovered by Pohl (Pohl 1958, 1978). In the presence of an electric field gradient, polarized particles move

along field lines to higher field regions. If the applied field is AC, the particles show a frequency dependant movement. At low frequencies particles move toward high field regions and at high frequency they move toward the low field regions. This cross over in direction of movement happens at a frequency determined by the dielectric properties of the particles as well as the medium they are in. The advantages of using AC field are reduction in electrokinetics, fluid heating and most importantly, exploitation of the frequency dependent dielectric behavior of particles. Using DEP we were able to probe the dielectric property of actin, pattern actin deposition, and also control the random movement of filaments during motility using moderate force and torque. Not only is DEP a novel technique to probe force in the context of biology, it has many applications in the field of nanotechnology. Advancement in the fields of microelectronics and microfluidics has influenced the development of miniaturized devices, where all necessary parts and methods to perform a chemical analysis are integrated. These micro total analytical systems (μ-TAS) will function as integrated sensing, actuating and synthesizing systems, with various uses. Development of such lab-on-a-chip requires integration of microsensors and microactuators on a single chip. This becomes challenging due to the lack of actuating structures with dimensions less than a micron. Molecular motors, as autonomous transporting and sensing systems, may play an important role in such nanoscale technologies. Integrating biomotors with nanoscale devices enables the use of ATP as an energy source to yield energy efficient systems capable of operating as pumps, valves and vehicles. Dielectrophoresis is a convenient technique to combine molecular motors with silicon electronics including the patterning of their position and the controls of motion for complete integration of molecular motors into μ-TAS.

5.2 Drag forces and torques

Physiologically relevant force probes might prove to be better techniques to study biological forces. For example, the effect of Brownian fluctuations and viscous drag on the organization of motile cytoskeletal filaments has widespread relevance to cell biology including cell motility and morphology, cellular transport and cell division. By incorporating the sliding motility assay of actin/myosin V into a microfluidic system, we were able to control and quantify flow effects on the system (**Chapter III**). Moderate flow applied to actin filaments steered and directed the filaments during motility. The organization of cytoskeletal filaments and motor proteins within the cell is crucial to many cellular processes including the transport of vesicles by motor proteins along oriented filament pathways, mitotic spindle formation during cell division and formation of filopodia and pseudopodia for cell migration. This assembly and movement takes place in the cytoplasm, a highly viscous medium (Valberg and Albertini, 1985) that exerts a drag force on all moving systems within the cell (Huang et al., 1999; Holzwarth et al., 2002). Therefore, it is important to study the effects of shear stress and viscous drag on cytoskeletal filaments coupled to motors. Microfluidic channels made of poly-dimethylsiloxane offer advantages such as the controlled delivery of reagents, regulation of fluid velocity and maintenance of laminar flow conditions (Whitesides, 2003). In addition, the response of motor-filament systems to physiologically relevant drag forces and torques may find a role in determining device geometries in integrated biomolecular devices that have proposed to use biomotors in micro total analytical systems (μ-TAS). More over, from a nanotechnology perspective there is an increasing interest towards building on-chip, integrated, biomotor-based analytical system (Montemagno and Bachand, 1999; Limberis and stewart, 2000; Soong et al., 2000). In the "lab-on-a-chip" or micro-total analytical system (μ-TAS) motif, a single device consists of

control electronics, chemical and physical barriers, all typically integrated in microfluidic channels.

5.3 Brownian motion

Motility and transport processes within biological systems takes place due to the coordinated efforts of cytoskeletal filaments and motor proteins. However, all this work is done in highly viscous and viscoelastic fluids against drag forces. The diffusion coefficient of a particle is related to the drag coefficient through the generalized Stokes- Einstein equations (**Chapter IV**). Therefore, by observing the thermal motion of particles in a fluid, the drag forces acting on the particle can be obtained. To study these drag forces inherently affecting the mobility of biological particles, rod-like particles in particular, we observed the thermal motion of gold nanorods and microtubules in Newtonian and complex fluids. This is the first example of macrorheology studies performed using rod-like particles as probes. Thermal motion in complex fluids is dependant not only on the viscoelastic properties but also on the length scale of the mesh network. Due to their small diameter, rods encounter mesh networks less frequently when they move axially and normally. However, due to their length, their rotational motion is restricted by the mesh. This could mean that microtubules, actin, organelles like mitochondria, pathogens like Tobacco mosaic virus and Listeria are all restricted in their rotational motion within the cytoplasm more than axial or normal motion. This has implications to cytoskeletal and organelle organization, restriction of DNA mobility for gene delivery applications and pathogen motility within cells. The observations presented in chapter IV could also have implications in the efficacy of using rod like particles in drug delivery.

CHAPTER II

DIELECTROPHORETIC MANIPULATION OF ACTIN-MYOSIN SYSTEM

This chapter includes the original publication:

Two-dimensional manipulation and orientation of actin-myosin systems with dielectrophoresis (2003). **Asokan SB**, Jawerth L, Carroll RL, Cheney RE, Washburn S, Superfine R , NANO LETTERS 3 (4): 431-437.

PREFACE

Molecular motors, as autonomous transporting and sensing systems, may play an important role in nanoscale technologies such as analytical and electromechanical systems. For this purpose, it is important to establish control over the patterning of deposition of filaments and their molecular motor-induced transport. Application of electrical signals to control motor motility is necessary for their integration with silicon electronics. We have applied dielectrophoretic (DEP) forces with quadrupole electrodes to pattern actin on a substrate. In addition, DEP torque(s) directed the motion of actin on myosin substrates along electric field lines. These are our first steps towards building an on-chip, integrated, biomotor analytical system.

1. Introduction

Biomolecular systems have been harnessed for many nanotechnology purposes including kinesin/microtubule system for linear transport (Limberis et al. 2001, Limberis et al. 2000) and F1-ATPase, which has been used for the construction of rotary biomotor-powered nanodevices (Montemagno and Bachand 1999; Soong et al. 2000). Mechanicaly defined grooves on substrates and lithographically defined channels in photoresist have proven useful in patterning molecular motors (Suzuki et al., 1997). Engineered tracks have been shown to direct the movement of filaments over motor substrates (Hess et al., 2001). For the dynamic control of molecular motor motion, light-controlled molecular shuttles capable of carrying cargo have been built (Hess et al., 2001; Dennis et al. 1999). In this chapter, we demonstrate the patterning of deposition and the control of motility of the actin/myosin motor system using dielectrophoresis (DEP). Using DEP we were able to probe the dielectric properties of actin, pattern actin deposition, and also control the random movement of filaments during motility using moderate force and torque. The properties of actin/myosin motor systems as a transportation system parallel those of the kinesin/microtubule system. However, the actin filament flexibility may allow finer definition of filament pathways and capability to turn corners in the fluidic channels of a μ-TAS, while the step size may offer greater ability for motor shuttles to cross from one filament to another. Laser traps have been used to study the mechano-chemical properties of single motor proteins (Visscher et al., 1999). However, building optical traps with the necessary tight focusing of light within a micro-scale system poses many difficulties. Electric fields at low frequencies have been used to apply weak forces on charged actin to direct the motion of actin filaments (Riveline et al., 1998). Through DEP, forces and torques were

applied to actin filaments using AC electric fields. Applying high frequency AC fields reduces electroosmosis and fluid heating in the buffer (Ramos et al., 1999). In addition, the frequency dependent dielectric behavior of particles may be exploited. In the following we describe the forces and torques generated by DEP on actin filaments, and their application to respectively, the deposition of filaments and the control over their motility.

Dielectrophoresis,(Pohl, 1978; Jones, 1995) the force experienced by a polarized particle in an electric field gradient, has been shown to manipulate and trap sub-micron particles(Washizu and Kurosawa 1990; Green and Morgan 1999). When particles are subjected to an electric field, a dipole moment is induced in them. In a non-uniform field a polarized particle experiences a net force, which can translate the particle to high or low field regions termed positive and negative DEP respectively. This movement depends on the polarizability of the particle relative to that of the medium. In an AC field, positive and negative DEP can be achieved by choosing appropriate frequencies .The frequency at which there is no force acting on the particle is the crossover frequency. A dipole aligns itself along the field lines in response to a torque, which is termed electro-orientation (EO). In structurally asymmetric particles EO can be used to align the particle axis with the electric field lines (Miller and Jones, 1993). Actin deposition on a substrate can be patterned using dielectrophoretic forces and orientation torques. Actin collected in the high field regions of the electrode geometry in response to DEP forces. The polarized filaments aligned their principal axes along field lines. Further, the torque on actin filaments acted as an aligning force during motility. The normally random movement of actin on myosin substrate was regulated to a collimated movement by alignment of the filaments parallel to field lines. This is a novel technique for bulk control of nanoscale motor transport.

2. Dielectrophoresis

The dielectrophoretic force on a particle in an electric field is given by,(Pohl 1978; Jones 1995)

$$F_{dep} = G_\alpha \varepsilon_m \, \text{Re}\{f_{CM}(\omega)\}_\alpha \left(\nabla E_{rms}^2\right) \, [1]$$

For a sphere

$$G_\alpha = 2\pi r^3 \, [2]$$

$$\{f_{CM}(\omega)\}_\alpha = \frac{\widetilde{\varepsilon}_p - \widetilde{\varepsilon}_m}{\widetilde{\varepsilon}_p + 2\widetilde{\varepsilon}_m} \, [3]$$

For a rod

$$G_\alpha = \frac{\pi}{6} r^2 l \, [4]$$

$$\{f_{CM}(\omega)\}_\alpha = \frac{\widetilde{\varepsilon}_p - \widetilde{\varepsilon}_m}{\widetilde{\varepsilon}_m} \, [5]$$

Where r is the particle radius, l the length, ε_m is the real permittivity of the suspending medium, ∇ is the gradient operator, E_{rms} is the local RMS electric field, and $\text{Re}\{f_{CM}(\omega)\}$ is the real part of the Clausius-Mossotti factor at a frequency of applied AC electric field. $\widetilde{\varepsilon}_p$ and $\widetilde{\varepsilon}_m$ are the complex permittivities of the particle and the medium respectively. The complex permittivity is given by $\widetilde{\varepsilon} = \varepsilon - i(\sigma/\omega)$ where $i = \sqrt{-1}$, ε is the real permittivity, and σ is the conductivity of the material. The real permittivity ε is a material property and can be written as a product of the relative permittivity of the material and permittivity of free space ε_0 (8.85x10^{-12} C^2/N.m^2). The direction of the DEP force, positive or negative, depends on the sign of the $\text{Re}\{f_{CM}(\omega)\}$. Obtaining both positive and negative DEP allows maximum versatility in the control of a mobile load. Ideally, in order to design the electronic control of

actin, we require its dielectric properties, Clausius-Mossotti factor and geometry. In the following we estimate the range of the complex permittivity of actin. We can further use this estimation to evaluate the forces and torques applied to actin filaments by AC electric fields.

2.1 Dielectric property of actin

Actin can be modeled as a rod shaped particle of 8 nm diameter, (Lodish et al., 1995) and it can polymerize into strands a few microns long *in vitro*. In solutions, they carry high surface charge (Tang and Janmey, 1996) and consequently are surrounded by a cloud of counter-ions. Application of an electric field distorts this counter-ion cloud. The presence of permanent dipoles along with charge-induced polarization should lead to high values of polarizability similar to that for DNA.(Asbury et al., 1998; Takashima and Fishman, 1977) Actin therefore, is expected to have higher polarizability than the medium at lower frequencies and consequently the DEP force is expected to be towards the high field region (positive DEP). The complex permittivity of actin has not previously been determined. The value of real permittivity ε for proteins has been estimated to range from $10\varepsilon_0$ to $36\varepsilon_0$ (King et al., 1991; Smith et al., 1993). We have assumed ε for actin to lie in this range. The imaginary part of the permittivity is the conductivity σ of actin. In the following we estimate this from the surface charge of actin. The surface charge density of a particle is known to affect its dielectrophoretic behavior, best explained in terms of Maxwell-Wagner interfacial polarization (Pohl 1978; Jones 1995). The total conductivity of a particle is the sum of its intrinsic conductivity and its surface conductivity (Green and Morgan, 1999).

$$k_p = k_{\text{int}} + k_s \ [6]$$

The surface conductivity of the particle is attributed to the movement of counter ions to the surface charge of the particle (Miles and Robertson, 1932; Fricke and Curtis, 1937; O'Konski, 1960). For a particle with a surface charge density σ, and counter ion mobility μ,

the surface conductance is given by $\lambda = \sigma\mu$. The linear charge density of actin at pH 7.2 is known to be approximately 6.4×10^{-19} C/nm (4 e/nm) (Tang and Janmey, 1996). Assuming a diameter of 8 nm, we expect actin to have a surface charge density of 0.025 C/m^2. In a buffer with predominantly potassium as the counter ion (mobility $\mu_K = 7.6 \times 10^{-8}$ m^2/Vs) the surface conductance for actin (λ) can be calculated to be 0.19×10^{-8} S. For an ellipsoid with axes a>>b=c, the surface conductivity is given by (O'Konski, 1960)

$$k_s = \frac{2\lambda}{b} \quad [7]$$

Using the above equation, we can calculate the surface conductivity of actin to equal 0.95 S/m. By assuming a negligible internal conductivity k_{int} for actin, the particle conductivity of actin from (Eq. [6]) is 0.95 S/m. With a conductivity of 0.95 S/m and permittivity ranging from $10\varepsilon_0$ to $36\varepsilon_0$, we obtain an approximate value of Clausius-Mossotti factor for actin. Figure 2.1 shows a plot of the Clausius-Mossotti factor for actin in M-buffer with $\varepsilon_m = 78\varepsilon_0$, $\sigma_m = 0.56$ S/m, as measured for M-buffer, $\varepsilon_p = 10\varepsilon_0$ and $36\varepsilon_0$, $\sigma_p = 0.95$ S/m, as calculated for actin. Also superimposed on this graph is the Clausius-Mossotti factor for 500 nm beads in Phosphate buffer (P-buffer) and M-buffer. For the beads the values used were $\varepsilon_p = 2.55\varepsilon_0$, $\sigma_p = 0.01$ S/m,[18] for P-buffer $\varepsilon_m = 78\varepsilon_0$, and $\sigma_m = 0.001$ S/m. The surface conductivity for the bead in M-buffer is not expected to change significantly from that in the phosphate buffer due to identical pH (7.2) and counter ions (potassium). Beads undergo both positive and negative DEP in P-buffer. The permittivity and conductivity values of beads are lower than that of M-Buffer, and thus the Clausius-Mossotti factor for beads is negative and a constant of −0.545 at all frequencies. Beads undergo only negative DEP in M-buffer.
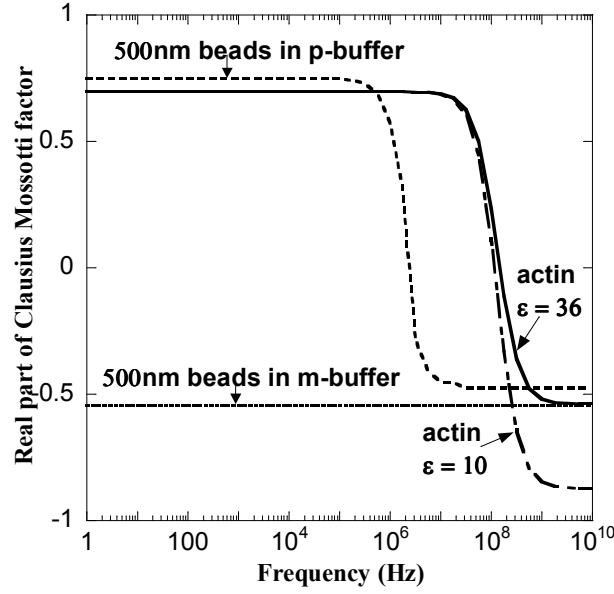
Figure 2.1. Plot of real part of Clausius-Mossotti factor versus frequency for actin in M-buffer and 500 nm beads in P-buffer and M-buffer. The values of dielectric constants used in the graph are, for actin $\varepsilon_p = 10\varepsilon_0 \& 36\varepsilon_0$, $\sigma_p = 0.95$ S/m, for the beads $\varepsilon_p = 2.55\varepsilon_0$, $\sigma_p = 0.01$ S/m, for P-buffer $\varepsilon_m = 78\varepsilon_0$, $\sigma_m = 0.001$ S/m, for M-buffer $\varepsilon_m = 78\varepsilon_0$, $\sigma_m = 0.56$ S/m. 500 nm beads in P-buffer have a cross over frequency of 1 MHz. Actin is expected to experience positive DEP at all frequencies < 100 MHz and negative DEP at all frequencies >100 MHz in M-buffer. 500 nm beads on the other hand experience only negative DEP in M-buffer.

From Figure 2.1, for the buffer used in our experiments, the $\text{Re}\{f_{CM}(\omega)\}$ for actin is approximately 0.7 for frequencies less than 1 Mhz and reduces to zero at around 100 Mhz. This range of values will be assumed for all further calculations.

2.2 Dielectrophoretic trapping and electro orientation

The DEP force is proportional to the size of the particle. For small particles the DEP forces are overpowered by thermal motion. To successfully trap a particle, the DEP potential

has to exceed thermal energy. A dipole in a field has an energy given by (Washizu, 1994)

$$E_{dep} = \frac{\pi}{6} r^2 l \varepsilon_m \, \text{Re}\{f_{CM}(\omega)\} E_{rms}^2 \quad [8]$$

The condition for trapping is given by

$$\frac{\pi}{6} r^2 l \varepsilon_m \, \text{Re}\{f_{CM}(\omega)\} E_{rms}^2 \geq \frac{3}{2} kT \quad [9]$$

$$E_{rms} \geq \sqrt{\frac{\frac{3}{2} kT}{\frac{\pi}{6} r^2 l \varepsilon_m \, \text{Re}\{f_{CM}(\omega)\}}} \quad [10]$$

A dipole in an electric field orients with its axis parallel to the field lines. The torque that acts on the dipole to align it is given by

$$T^e = P \times E \quad [11]$$

In rectilinear coordinates, the x component of the torque is given by

$$T_x^e = \frac{1}{2} \text{Re}\left[(P_{eff})_y E_{0,z}^* - (P_{eff})_z E_{0,y}^*\right] [12]$$

For an isotropic ellipsoid of dimensions a > b > c (Figure 2.2), the axial components of the effective dipole moment due to the dielectric ellipsoid is (Stratton, 1941; Jones, 1995)

$$(P_{eff})_x = \frac{4\pi abc}{3} \varepsilon_m \left[\frac{\widetilde{\varepsilon}_p - \widetilde{\varepsilon}_m}{\widetilde{\varepsilon}_m + (\widetilde{\varepsilon}_m - \widetilde{\varepsilon}_p) L_x}\right] E_x \quad [13]$$

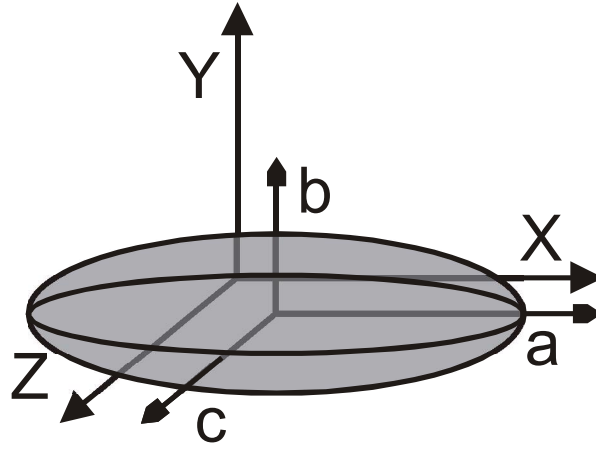Where L_x is the depolarization factor defined by an elliptical integral

$$L_x = \frac{abc}{2} \int_0^\infty \frac{ds}{(s + a^2)\left(\sqrt{(s + a^2)(s + b^2)(s + c^2)}\right)} \quad [14]$$

25

$$W = \int_{\theta}^{0} 4\pi r^2 l\varepsilon_m \, \text{Re}\left(\frac{(\widetilde{\varepsilon}_p - \widetilde{\varepsilon}_m)^2}{(\widetilde{\varepsilon}_m(\widetilde{\varepsilon}_p + \widetilde{\varepsilon}_m))}\right) E_0^2 \, Sin\, 2\theta d\theta \quad [15]$$

The $(P_{eff})_y$ and $(P_{eff})_z$ are of similar form. Combining these equations, the x component of torque equals

$$\langle T^e \rangle_\alpha = \frac{2}{3}\pi abc\, \varepsilon_m (L_z - L_y) E_{0,y} E_{0,z} \, \text{Re}\left[\left(\frac{\widetilde{\varepsilon}_p - \widetilde{\varepsilon}_m}{\widetilde{\varepsilon}_m + (\widetilde{\varepsilon}_p - \widetilde{\varepsilon}_m)L_y}\right)\left(\frac{\widetilde{\varepsilon}_p - \widetilde{\varepsilon}_m}{\widetilde{\varepsilon}_m + (\widetilde{\varepsilon}_p - \widetilde{\varepsilon}_m)L_z}\right)\right] \quad [16]$$

Figure 2.2. Elliptical particle with axes a > b > c aligned along the coordinates.

The torque equations reveal that the particle will attain equilibrium if any of its axes is aligned with the electric field as the torque acting on the particle becomes zero. However, stable equilibrium is when the energy of the dipole in the field is a minimum. For particles with no dielectric loss, the stable equilibrium is when the longest axis is aligned parallel to the electric field. For a homogenous dielectric particle with loss, the axis of stable equilibrium is dependent on frequency. For a prolate spheroid like actin (a >> b = c; a = half the length and b = c = r) the torque acting on the particle to align the longest axis (x) parallel

to the electric field can be calculated to be (Stratton, 1941; Talbott and Stefanakos, 1972; Jones, 1995)

$$\langle T^e \rangle_{prolate} = 4\pi r^2 l \varepsilon_m \, \mathrm{Re}\left[\left(\frac{(\tilde{\varepsilon}_p - \tilde{\varepsilon}_m)^2}{[\tilde{\varepsilon}_m + (\tilde{\varepsilon}_p - \tilde{\varepsilon}_m)L_{\parallel}](\tilde{\varepsilon}_p + \tilde{\varepsilon}_m)}\right)\right] E_{rms}^2 \, Sin\, 2\theta \quad [17]$$

Where

$$L_{\parallel} = \frac{4r^2}{l^2}\left[\ln\left(\frac{2l}{r}\right) - 1\right] \quad [18]$$

r and l are the radii and the length respectively. For a needle shaped particle like actin where l >> r, $L_{\parallel}$ << 1. The expression for torque reduces to

$$\langle T^e \rangle_{prolate} = 4\pi r^2 l \varepsilon_m \, \mathrm{Re}\{K(\omega)\} E_{rms}^2 \, Sin\, 2\theta \quad [19]$$

$$\mathrm{Re}\{K(\omega)\} = \mathrm{Re}\left(\frac{(\tilde{\varepsilon}_p - \tilde{\varepsilon}_m)^2}{(\tilde{\varepsilon}_m(\tilde{\varepsilon}_p + \tilde{\varepsilon}_m))}\right) \quad [20]$$

For the buffer used in the experiments and the previously calculated values of dielectric properties of actin, Re{K(ω)} is a constant till 10 MHz and equal to 0.2. The work done by the torque in aligning the particle parallel to the field is given by

$$W = \int_{\theta}^{0} \langle T_e \rangle_{prolate} \, d\theta \quad [21]$$

Where, θ is the angle of inclination of the dipole with the electric field. Integrating and applying maximum limits of θ = π/2 to θ = 0, we get

$$W = 4\pi r^2 l \varepsilon_m \, \mathrm{Re}\left(\frac{(\tilde{\varepsilon}_p - \tilde{\varepsilon}_m)^2}{(\tilde{\varepsilon}_m(\tilde{\varepsilon}_p + \tilde{\varepsilon}_m))}\right) E_{rms}^2 \quad [22]$$

To produce a torque capable of aligning the filaments, this work must exceed the thermal energy of 1/2kT per degree of freedom. Since we are applying torque to actin filaments

bound to myosin on a surface, the filaments are allowed only one degree of freedom and hence

$$4\pi r^2 l \varepsilon_m \, \text{Re}\left(\frac{(\tilde{\varepsilon}_p - \tilde{\varepsilon}_m)^2}{(\tilde{\varepsilon}_m(\tilde{\varepsilon}_p + \tilde{\varepsilon}_m))} \right) E_{rms}^2 \geq \frac{1}{2} kT \quad [23]$$

$$E_{rms} = \sqrt{\frac{\dfrac{kT}{2}}{4\pi r^2 l \varepsilon_m \, \text{Re}\left(\dfrac{(\tilde{\varepsilon}_p - \tilde{\varepsilon}_m)^2}{(\tilde{\varepsilon}_m(\tilde{\varepsilon}_p + \tilde{\varepsilon}_m))} \right)}} \quad [24]$$

3. Materials and Methods

3.1 Electrode Fabrication

Quadrupole microelectrodes (Huang and Pethig, 1991) were fabricated on glass slides using standard photolithography techniques. Clean glass coverslips are rinsed with acetone and methanol and blow dried with a stream of nitrogen and plasma cleaned for ~15 minutes. Su-8 photoresist is spin coated onto the glass at 4000 rpm and for 60 seconds, then placed on a hotplate set at 115 C for 1 min. The samples are then exposed to UV light in the mask aligner loaded with the chrome mask. A mixture of 2:1 1813 developer to water is prepared in a beaker and the samples are waved gently in it for 1 min, rinsed with water and gently dried with nitrogen. A 10 nm chrome seed layer followed by a 100 nm gold layer is evaporated onto the samples in the thermal evaporator. The samples are then soaked in acetone for 15 mins and sonicated until clean. Figure 2.3 shows a transmission optical micrograph of the electrodes in bright-field.
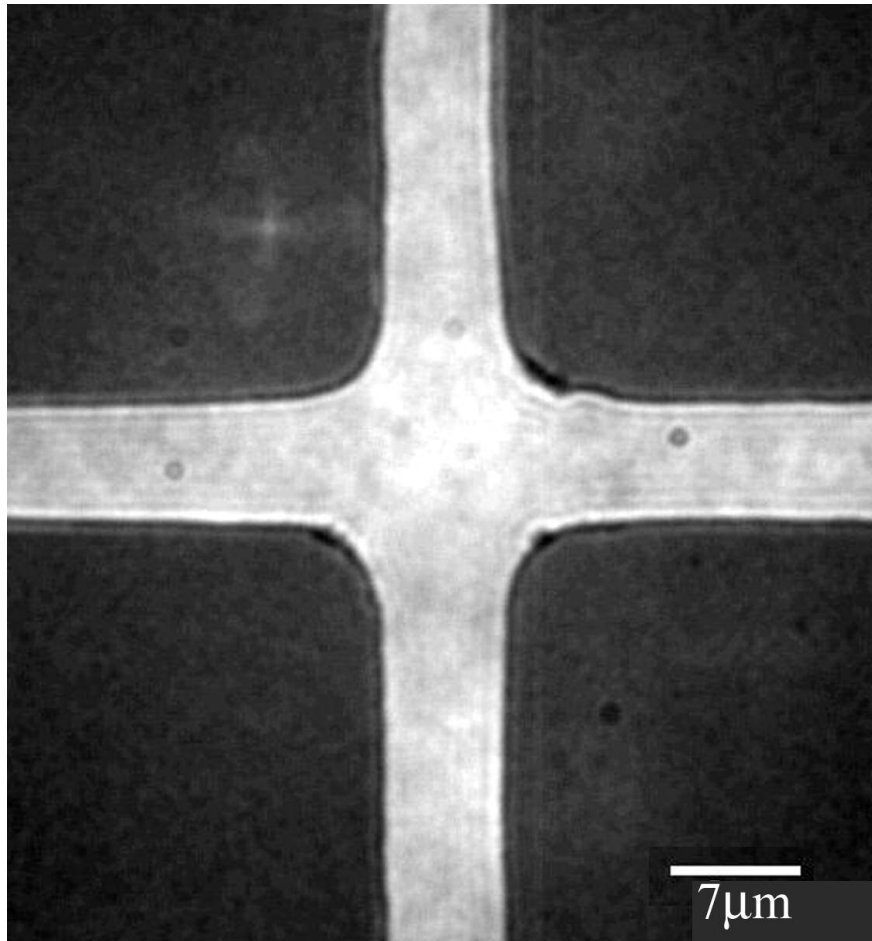
Figure 2.3. Bright field transmission micrograph of quadrupole electrodes fabricated on glass (100x objective). The metal electrodes appear dark. Distances between adjacent electrodes were 7 μm and the diagonal electrode separation was 12 μm.

Electric field simulations of the electrode geometry were performed using FEMLAB (Comsol Group) with MATLAB (Mathworks). Figure 2.4A shows a side view of gradient of the square of the electric field in a 30micron volume above the electrodes. Figure 2.4B shows the field distribution just above the electrodes. In both simulations two of the opposing electrodes were grounded and the other two were maintained at 10V.
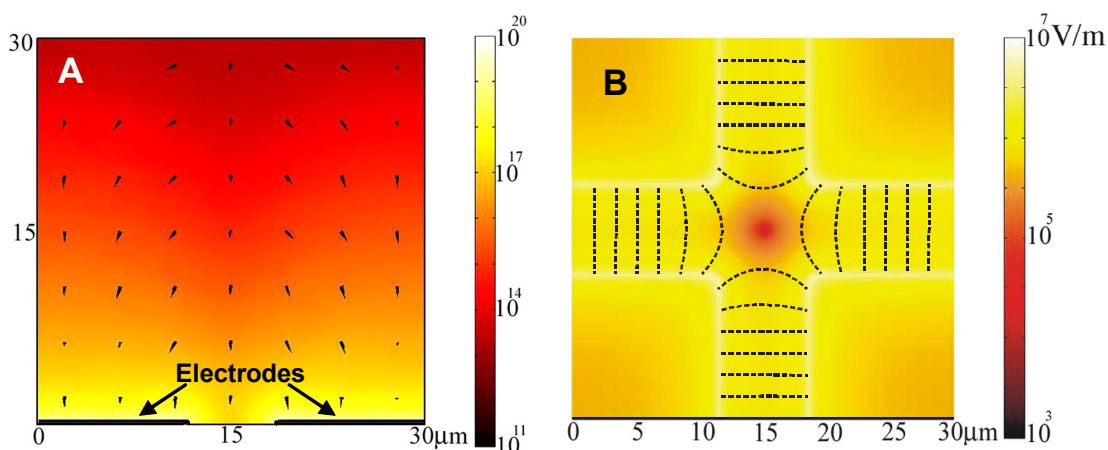
Figure 2.4. A. The simulated electric field square gradient ($\propto$ force) in V^2/m^3 in YZ plane at the edge of the electrodes. Simulations were performed in a 30 micron volume above the 200 nm thick electrodes. The arrows point in the direction of the DEP force indicating that particles will be pulled down towards the electrode tips **B.** The simulated electric field strength (V/m) in the XY plane just above the electrodes. This simulation shows high field around the electrode edges and a low field minimum at the center of the geometry. When particles experience positive DEP they are trapped at the edge of the electrodes. When they experience negative DEP, they collect at the center of the geometry. The dotted lines indicate field lines. When actin filaments are trapped, they align parallel to these field lines.

3.2 Preparation of proteins

G-actin and Myosin V(Cheney 1998; Cheney et al., 1993) were stored at -77^0 C. The globular monomer (G-actin) was polymerized by mixing G-actin and high salt concentration M-buffer in a 1:1 ratio by volume. F-actin (filamentous actin) was then labeled with fluorescently tagged Alexa-phalloidin 488 (Molecular Probes). Myosin V was in concentrations varying from 200-500 μg/ml and was diluted down to 1-2 μg/ml for

experiments. All proteins were diluted to required concentrations in M-buffer consisting of 10 mM MOPS, 75 mM KCl, 2.5 mM MgCl2, 2 mM DTT, 1 mM EGTA, adjusted to pH of 7.2 with KOH. The conductivity of the buffer was measured using Acumet Basic AB30 conductivity meter, and found to be 0.56 S/m. 500 nm carboxylate modified polystyrene beads (Molecular Probes) were also diluted to 1 in 40000 by volume in the M-buffer.

3.3 Experimental setup

Flow chambers (22 mm x 22 mm x 60 µm) were constructed on the electrode slides with PDMS spacers and a cover slip. AC fields were generated by connecting the electrodes to Tenma 2 MHz sweep function generator for frequencies below 2 MHz and a Fluke 6039A frequency generator for frequencies in the range 2-30 MHz. The experiments were observed using a Nikon Diaphot 200 inverted microscope with epi-fluorescence attachment. Images were collected using a Spot 2 cooled-CCD camera (Diagnostic instruments inc.).

3.4 Motility assay

Globular monomeric actin (G-actin) and myosin V were purified by previously described methods (Cheney, 1998) and were stored at –77 C. G-actin was polymerized by mixing G-actin and M-buffer in a 1:1 ratio by volume. F-actin (filamentous actin) was then labeled in a 1:1 ratio with fluorescently tagged Alexa 488-phalloidin (Molecular Probes). Myosin V was stored in concentrations varying from 200-500 µg/ml and was diluted to required concentrations before experiments. All proteins were diluted to required concentrations in M-buffer consisting of 10 mM MOPS, 75 mM KCl, 2.5 mM MgCl$_2$, 2 mM DTT, 1 mM EGTA, adjusted to pH of 7.2 with KOH. Assays are performed in flow chambers made by placing double stick tape as spacers between 2 coverslips. This allows us to flow in the different proteins in the following order. First, low concentrations of BSA (10 µg/ml) to pre block the surface, followed by myosin V (2 µg/ml), and then high

concentration of BSA (2 mg/ml) to completely block the surface. Filamentous actin at (10 nM) is flowed in next. Finally, ATP at 2 mM is flowed in to start motility. A free radical scavenging system consisting of dextrose, glucose oxidase and catalase was added to the ATP to reduce photobleaching.

4. Results

4.1 Patterning of Actin

40 μl of 10 nM actin was flowed into the chamber and the electrodes were energized. Two of the opposing electrodes were grounded and the other two connected to a 10 $V_{peak-peak}$ (7V_{rms}) AC source. DEP of actin was observed from 100 KHz up to 30 MHz. At these frequencies and voltage, the actin filaments underwent positive DEP and collected in the high field regions of the quadrupole geometry. The actin filaments were oriented with the long axis parallel to field lines. No other axial alignment was observed in the frequency range of these experiments. We also observed actin filaments aggregating end to end. Figure 2.5 shows actin filaments collecting at the electrodes in an aligned manner at 1 MHz and 7 V_{rms}. We note that shorter filaments did not collect at the electrodes, although, they could be seen undergoing Brownian motion in the solution above the electrodes. To compare the dielectric properties of actin with that of polystyrene beads, DEP of beads and actin were observed from 100 KHz to 30 MHz and 7 V_{rms}. In this frequency range, actin filaments underwent positive DEP while the beads underwent negative DEP (Figure 2.6).
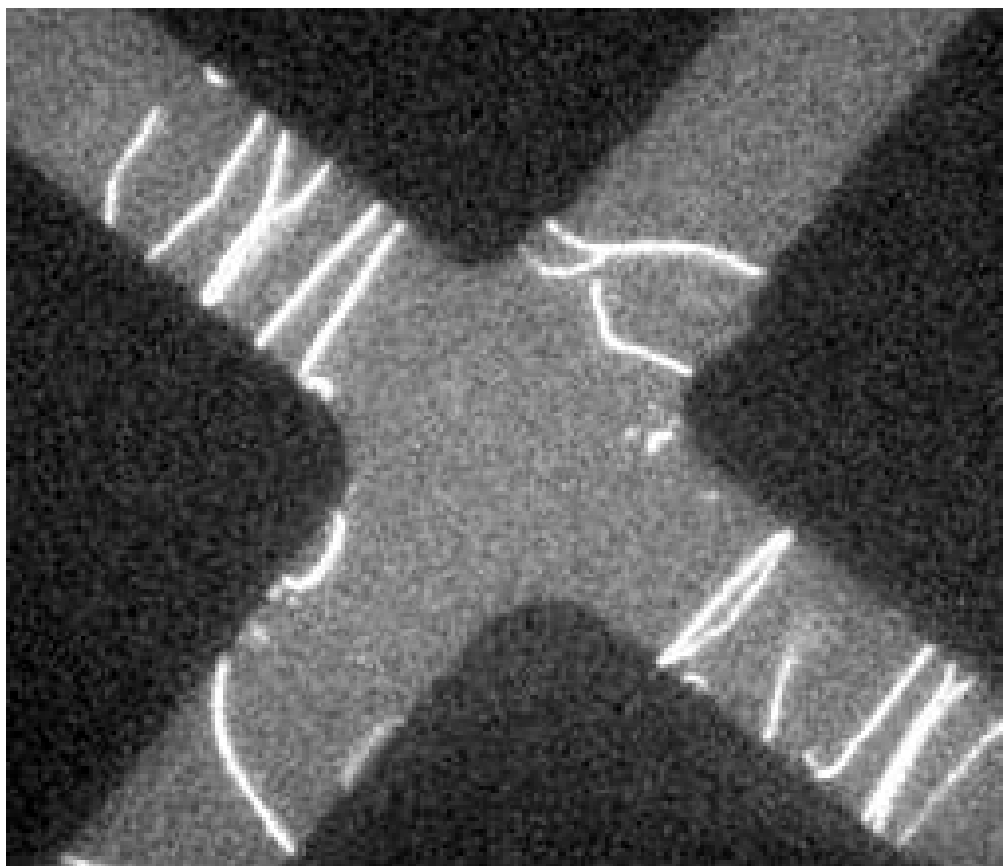
Figure 2.5. Fluorescently labled actin filaments (appear bright) are seen collecting at the electrode edges (appear dark), the high field region of the quadrupole geometry. The applied frequency is 1 Mhz and the voltage is 7 V_{rms}. These filaments are deposited in the absence of motors. As expected, the actin filaments orient themselves parallel to the field lines.
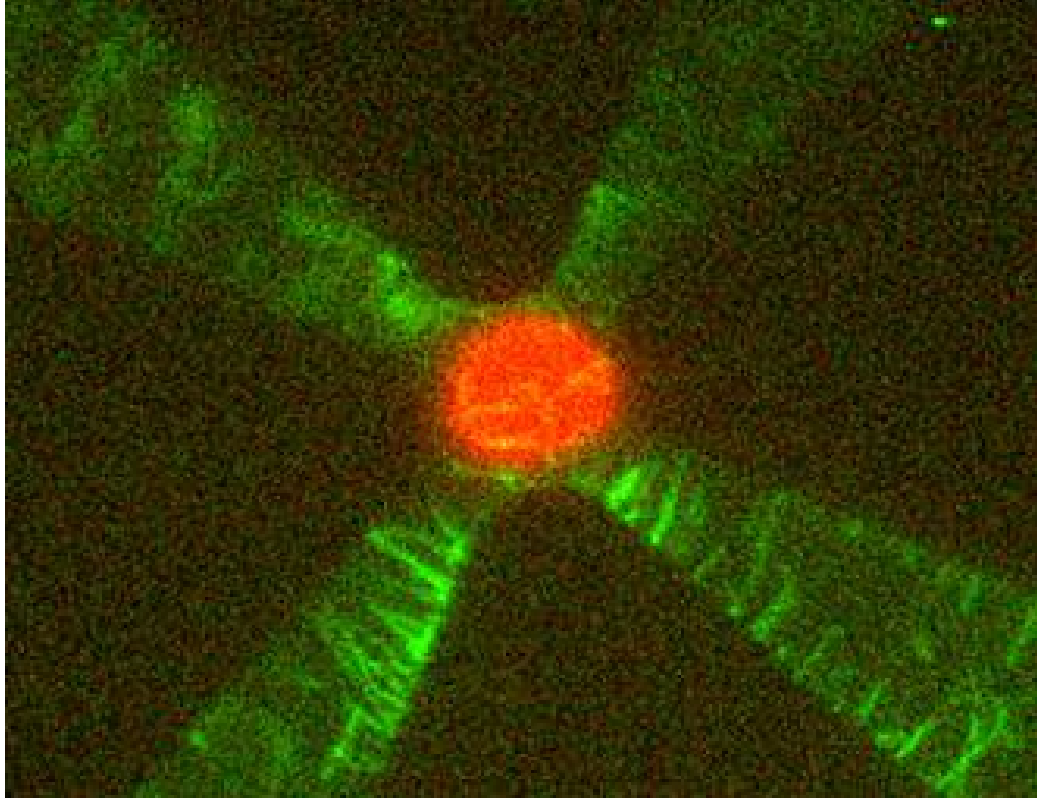
Figure 2.6. Epifluorescence image of actin filaments (green fluorescence) attracted to high field regions (positive DEP) and beads (red fluorescence) attracted to low field region (negative DEP) in M-buffer. The electrodes appear dark. The AC field was at 2 MHz and 7 V_{rms}. This is consistent with our theoretical prediction plotted in figure 2.1.

4.2 Actin alignment during motility

The motility assay (Cheney, 1998; Cheney et al., 1993) of actin on myosin substrate under the influence of DEP forces at 1 MHz and 7 V_{rms} was also observed in the same quadrupole electrode setup. Actin was deposited on random myosin substrate prior to energizing the electrodes. After the introduction of ATP, when the filaments started motility, the electrodes were energized. The filaments began to align along the field lines during

motility. They continued to glide on the myosin in an aligned manner as long as the field was on. The torque on actin maintained the parallel alignment of the filaments. The random movement of actin on the substrate changed to a collimated movement between electrode edges (Figure 2.7A). When the DEP force was turned off the actin filaments continued random motion over the myosin bed (Figure 2.7B).
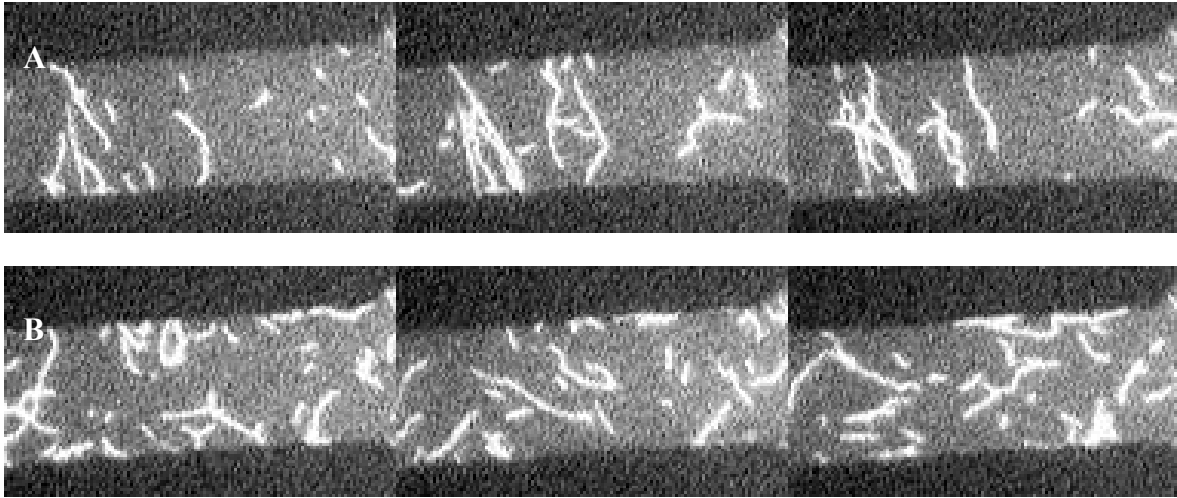

Figure 2.7. Epi fluorescent images of actin motility between quadrupole electrodes. One of the four sections of adjacent electrodes is shown above. Electrodes appear dark. The figure on top shows actin motility on myosin substrate when the electrodes are energized. Longer filaments are aligned perpendicular to the electrode edges during motility. The figure on the bottom shows actin motility on myosin substrate when the electrodes are turned off. Filaments undergo motility in random directions. Each image in the sequence is 15secs apart.

5. Discussion

Filaments can be trapped only if their potential due to DEP forces exceeds thermal energy. To estimate the electric field required to trap actin filaments of a given length, we compared the electric potential energy for actin to its thermal energy. The Figure 2.8 shows

the result of this comparison. With field strengths of approximately 1.5×10^6 V/m as applied in our experiments, it is theoretically possible to trap actin filaments of length greater than 1 μm. This is consistent with what was observed. When AC fields of frequency ranging from 100 KHz to 30 MHz and 7 V_{rms} was applied to polystyrene beads in M-buffer, they underwent negative DEP where as actin underwent positive DEP (Figure 2.6). This is consistent with our calculation that the dielectric properties of actin are much higher than that of polystyrene beads. The theoretical plot of Clausius-Mossotti factor for actin and beads in Figure 2.1 also supports the experimental results. Actin filaments can be successfully trapped using dielectrophoresis. With field strengths of 1.5×10^6 V/m applied in our experiments, it is possible to trap filaments of length greater than 1 μm (Figure 2.8).
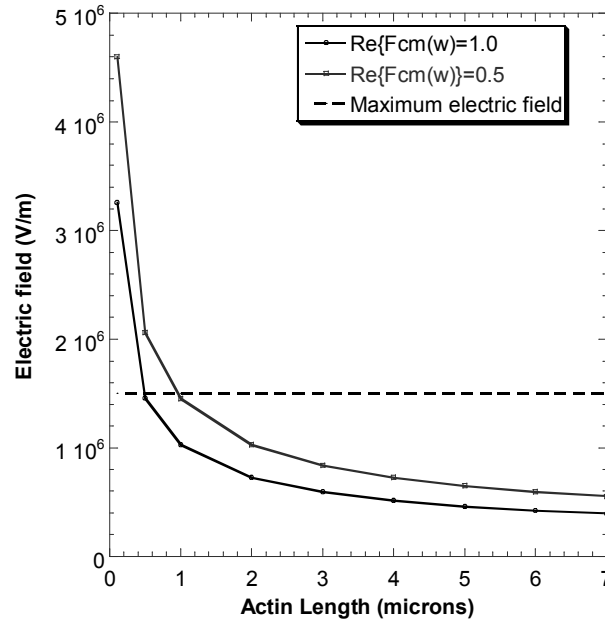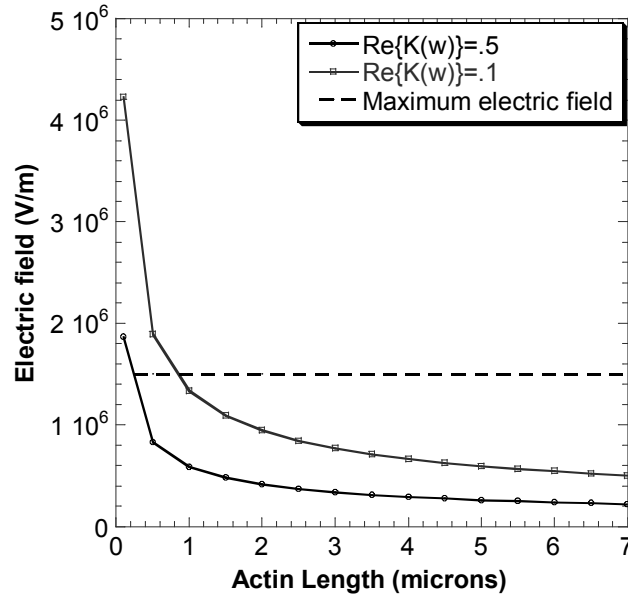

Figure 2.8. Plot of minimum electric field required to trap actin filaments of different lengths. At a frequency of 1 Mhz, The real part of Clausius-Mossotti factor ranged from 0.5 to 1.0. The maximum electric field strength obtained using the quadrupole geometry equals

1.5×10^6 V/m indicated by the dotted line. Filaments shorter than a micron require field strengths greater than 1.5×10^6 V/m, therefore they cannot be trapped.

We also observed actin filaments aggregating end to end, possibly due to dipole-dipole interactions. Potentially, this could be used as a method to build very long tracks of actin. According to our calculations where we presumed a high surface charge (figure 2.1), actin is a polyelectrolyte with high polarizability, more polarizable than polystyrene beads. This theoretical prediction is supported by our observation that actin underwent positive DEP in M-buffer while the beads underwent negative DEP (Figure 2.6). Consequently, negative DEP of actin was not observed within the frequency range of the experiment. Frequencies higher than 30 MHz might be necessary and are not within the range of our instruments. Further, these experiments demonstrate the capability to separate particles of different dielectric properties by DEP (Morgan et al., 1999).

Even on a random myosin substrate the motility of actin filaments can be patterned by electro orientation due to the torque acting on the filaments. The shorter filaments however, did not respond to the field induced torque and continued to move in random directions (figure 2.7). To estimate the field strength required to align actin filament of a given length, the energy required to align a filament was compared to the thermal energy of the filament. Figure 2.9 shows a plot of this calculation. With the field strengths applied in our experiments, it is possible to align actin filaments longer than 1μm. From Figure 2.4A the simulated value of the gradient of the electric field at the electrode edges is equal to 10^{20} V^2/m^3. At this gradient, the positive DEP forces acting on actin filaments of 1 micron length can then be calculated to be ~0.4 pN. The stalling force for myosin V during motility assay is

known to be 3 pN (Mehta et al., 1999) Therefore, DEP forces are not expected to be capable of stalling motility. However, DEP torque was observed to align actin during motility.

Figure 2.9. The minimum electric field strength required to align actin filaments of different lengths along field lines during motility. The values of torque calculated are for actin filaments initially inclined at a 90^0 angle to field lines. The calculated $K(\omega)$ value for actin at 1Mhz ranges from 0.1 to 0.5. The maximum electric field strength obtained using the quadrupole geometry equals 1.5×10^6 V/m indicated by the dotted line. Filaments shorter than a micron require field strengths greater than 1.5×10^6 V/m, therefore they cannot be aligned.

The torque acting on the filaments reduced the randomized movement of actin on myosin substrate to a collimated motion. Actin moves on a myosin substrate with its structurally negative end as the leading end. During motility, the filament length beyond the last bound myosin is free to undergo Brownian fluctuations. Hence the next myosin that the leading edge binds to lies anywhere in the area swept by the free end. Normally this leads to random motion of actin on a myosin substrate. When the electrodes were energized during

motility, the torque on the filament suppressed Brownian fluctuations of the free end. Theoretical calculations show that the work done by the torque to align filaments longer than 1 μm is greater than Brownian motion and the filaments were forced to move on myosins that lie along the field lines (Figure 2.7).

6. Conclusion

So far, positive DEP and electro-orientation torques were observed to align actin parallel to field lines. To exert greater control over patterning and motility, negative DEP and perpendicular alignment of filaments would be required. Kriegmaier et al. (Kriegmaier et al., 2001) have observed different electro-orientations of fission yeast at varying frequency of applied fields. Higher frequencies are expected to be necessary for both these experiments. Not only is DEP a novel way to manipulate actin filaments, it offers many practical utilities. Substrate patterning of actin by DEP to lay pathways for motor motility can be achieved by designing electrodes that generate appropriate electric field patterns. Dielectrophoresis as a technique for patterning and maneuvering filaments is an important step towards biomolecular integration with NEMS. DEP can be combined with physical and chemical barriers for actin/myosin movement and to direct their motion in microfluidic channels. Alternatively, motors can be manipulated in these channels by polarizing the cargo they carry, as they move over fixed filaments. Beads have been attached to myosin, actin and other motor proteins successfully. Coating these beads with therapeutic drugs and using motor proteins to deliver them to cells by using endogenous ATP to fuel the system would be a practical application.

CHAPTER III

STEERING MOTILE ACTIN FILAMENTS IN MICROFLUIDIC CHANNELS

PREFACE

Force technologies involving electric fields, lasers and microneedles have proved useful in answering many biological questions. But, physiologically relevant force probes might prove to be better techniques to study biological forces. For example, the affect of Brownian fluctuations and viscous drag on the organization of motile cytoskeletal filaments has widespread relevance to cell biology including cell motility and morphology, cellular transport and cell division. To quantify such response, sliding filament assays of actin sliding on a lawn of motor protein myosin V under the influence of external flow were observed inside microfluidic channels. In these channels, drag forces due to flow significantly lower than the motor stall force generated torques large enough to efficiently steer the actin filaments. Filaments that initially followed a random path started to move down stream when flow was introduced. Further analysis of filament distribution showed an increase in their alignment with an increase in flow rate. The competition between flow-induced torques and thermal fluctuations is described using a simple physical model. Flow induced alignment of motile filaments is discussed in the context of biological flows especially cytoplasmic streaming. In addition to its relevance to biology, the response of motor-filament systems to physiologically relevant drag forces and torques may find a role in determining device geometries in integrated biomolecular devices that have proposed to use biomotors in micro total analytical systems (μTAS).

1. Introduction

The effects of viscous drag in biological systems have been measured previously by performing motor motility assay in viscous solutions (Hunt et al., 1994), applying fluid shear stress on lamellipodia (Hu et al., 2002), analyzing flow effects on microtubule rigidity (Venier et al., 1994) and regulating platelet adhesion to fibrinogen (Litjens et al., 2003). The latter three have been studied under quantified flow conditions. Additionally, Spudich *et al* observed the movement of myosin-coated beads on fixed actin filaments whose orientation was determined by flow during attachment (Spudich et al., 1985). Stracke et al have aligned motile microtubules in a flow cell using fluid flow (Stracke et al., 2000). However, a quantitative analysis of fluid flow and its effects were not performed. To observe and quantify effects of force and torque due to drag on such systems, *in vitro* motility assays with actin filaments on motor protein myosin V under controlled flow conditions was performed. These experiments showed that drag forces significantly lower than motor forces can generate torques on the filaments and steer them during motility. Flow reduces the extent of thermal fluctuations of actin due to the preferential orientation imposed by the torque acting on them. Combined with motors, flow can thus polarize an initially random distribution of filaments, and in the process may aid in organization of the cytoskeleton.

We used microfluidic channels made of poly-dimethylsiloxane to apply flow forces to and observe the effect of these forces on actin – myosin motor systems. These channels offer advantages such as the controlled delivery of reagents, regulation of fluid velocity and maintenance of laminar flow conditions (Whitesides, 2003). More over, from a nanotechnology perspective there is an increasing interest towards building on-chip, integrated, biomotor-based analytical system (Montemagno and Bachand, 1999 ;Limberis

and Stewart, 2000;Soong et al., 2000). In the "lab-on-a-chip" or micro-total analytical system (μ-TAS) motif, a single device consists of control electronics, chemical and physical barriers, all typically integrated in microfluidic channels. Further integration of biomotor functionality in microfluidics and control electronics may play an important role in using filaments as transport, separation and force sensing systems in μ-TAS.

In a modeling study performed by Duke and coauthors, their simulations predict that the dynamics of the filaments depend on the motors (surface concentration) and filaments (length and rigidity) (Duke et al., 1995). Their model predicts the physical relationship between experimentally observable quantities like the persistence length of the filament path and the motor density and filament rigidity. Simulated results were compared with experimental observations of a kinesin and microtubule sliding motility assay (Howard et al., 1989). In the following work we show that the statistics of the filament path depends on external conditions like force and torque due to flow. In this context, we require a model for flow alignment to understand the dynamics of the filaments in the presence of flow. During a sliding filament assay, myosin V adsorbed to the surface move towards the barbed end of actin thereby propelling the filaments with their pointed end as the leading end. When a filament attaches to multiple motors, its conformation is constrained at the motor binding sites. The filament only moves along its contour, acquiring new motors at its leading end while losing motors at the trailing end. In this case, especially at small inter-motor spacing, bending fluctuations of actin are very small leading to linear motion. At times when only a single motor binds the filament, it gains freedom to pivot about that motor as it propels forward. In this case however, a pure diffusive rotational motion of the filament can be

assumed due to the low torsional stiffness of molecular motors (Hunt and Howard ,1993; Mehta et al., 1999). The path of a filament is thus characterized by periods of linear motion (when bound to multiple motors) and rotational diffusion (when bound to a single motor) and the filament becomes uncorrelated in alignment when bound to a single motor. When external flow is present, a restoring torque acts on the actin filaments and reduces (Kapitein et al., 2005) the amplitude of oscillations due to rotational diffusion. The extent of the flow alignment for a particular assay depends on both the filament properties like average length and rigidity as well as inter-motor spacing.

In the following work, we present a model for the flow alignment of filaments by analyzing the torque due to flow acting on filaments (rods) rotating on motors (pivots). Our experimental results show that drag forces significantly lower than motor forces can generate torques on the filaments and align them during motility and that the filament alignment increases with an increase in flow rate. We reason that filaments are more susceptible to flow alignment when bound to a single motor and our model is based on this assumption.

2. Materials and methods

2.1 Microfluidic flow cell

The microfluidic channels were made by consecutive steps involving rapid prototyping, lithography, replica molding and sealing (McDonald et al., 2000; Duffy et al., 1998). The channel was designed using the CorelDraw (Corel) computer drawing package. The design was printed on transparency using a commercial high-resolution printer (Pageworks, Inc., Cambridge MA). A positive relief of a thick photoresist (SU-8 2050) was generated on silicon wafers using the transparency as a mask and standard photolithographic

procedures. Microfluidic channels were produced by curing liquid poly-dimethylsiloxane (PDMS, Dow-Corning Sylgard 184) against the photolithographed master (Figure 3.1).
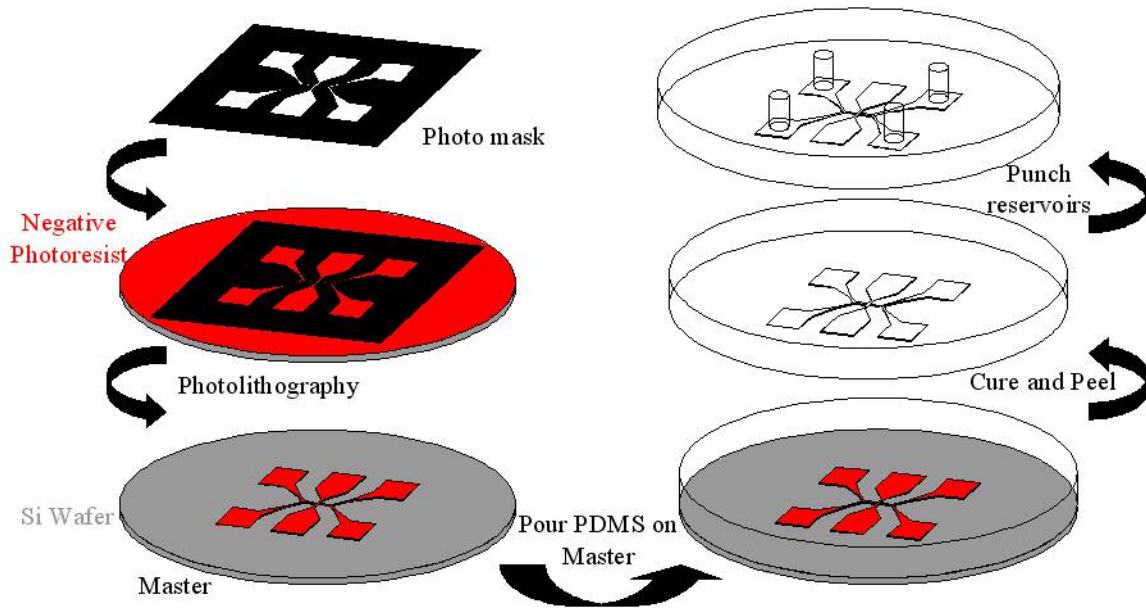
Figure 3.1. Steps to generate microfluidic channels involved Photolithography, replica molding and sealing. The Photomask was designed using the CorelDraw (Corel) computer drawing package printed on transparency. Standard photolithographic procedures were used to generate a positive relief of a thick photoresist (SU-8 2050) on silicon wafers. Microfluidic channels were produced by curing liquid poly-dimethylsiloxane against the master. The channels were peeled out and fluidic connections were punched out of the PDMS with a sharpened metal tube.

The channel used in the experiment was 750 μm wide and 60 μm tall. Fluidic connections were punched out of the PDMS with a sharpened metal tube. 24 x 50 mm, #1-1/2 coverslips were rinsed with water and ethanol and blown dry with N_2. The PDMS was cleaned with Americanbrand[TM] ultrasonic liquid detergent, rinsed with de- ionized water and blown dry with N_2. The coverslip and the PDMS channels were exposed to oxygen plasma for 30

seconds with the channel side facing up. Upon removing them from the plasma, we placed

the PDMS and the coverslip immediately into contact to form an irreversible seal. Teflon

tubing was inserted into the punched out reservoirs and connected through Teflon 4 port

micro valves to a syringe operated by a syringe pump. The fluid circuit was set up as shown

in Figure 3.2. When port 1 and 2 are connected, fluid flows into the channel through

reservoir 1 (R1), then out to waste through ports 3 and 4. To reverse the direction of flow in

the channel the knob of the 4-port valve is rotated 90 degrees. This connects port 1 to port 4,

and fluid flows through reservoir 2 (R2) into the other end of the channel, reversing the flow

back out through ports 2 and 3.
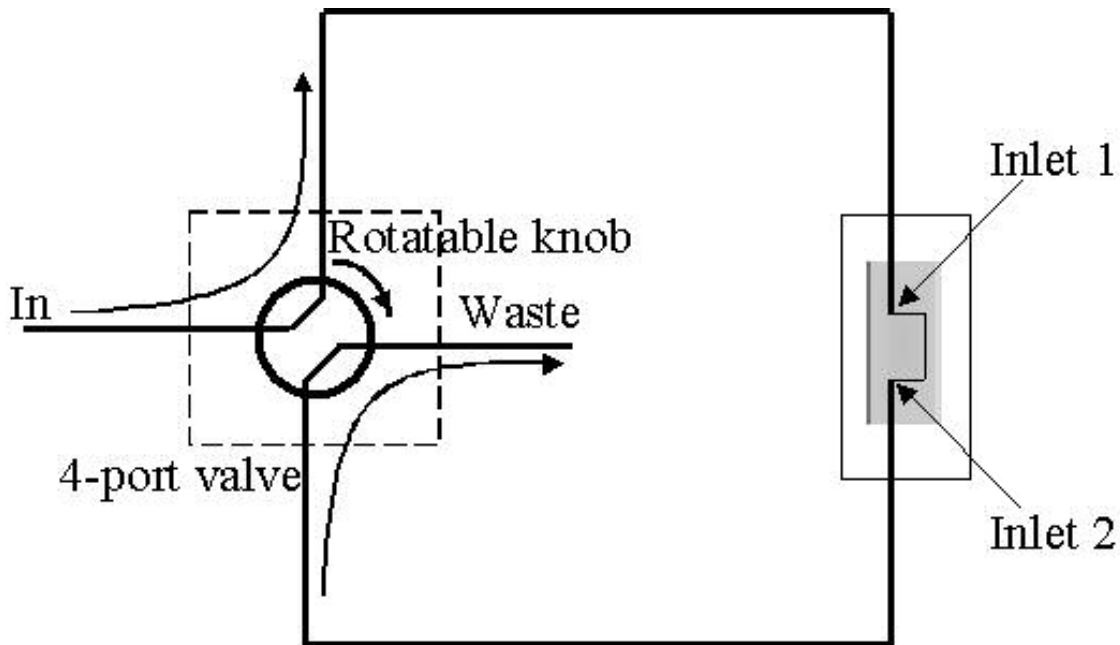
Figure 3.2. Schematic of the fluidic circuit. In this configuration, fluid flows into the

channel through inlet 1. To reverse flow, the rotatable knob is turned by 90 degrees and fluid

flows through inlet 2.

The Reynolds number (Re), a dimensionless quantity provides information on whether the flow in the channel is laminar or turbulent (Guyon et al., 2001). We calculated Re using the formula $Re = \dfrac{\rho D_h U_{avg}}{\eta}$ to be of order unity for density $\rho=1000$ kg/m^3, viscosity $\eta= 10^{-3}$ Ns/m^2 for water, the highest average flow velocity $U_{avg} = 9*10^{-3}$ m/s and the hydraulic diameter of our rectangular channel $D_h =111$ μm. This is far less than the critical Reynolds number of 2300 below which laminar flow conditions are maintained in the channel. The velocity profile for laminar flow in the channel is given by $U_y = \dfrac{6U_{avg}}{D^2} y(D-y)$ [1], where U_y is the velocity at a height y in the channel in terms of the average velocity in the channel (U_{avg}) and height of the channel (D)(Guyon et al., 2001). We observe that upon stopping the flow with our valve system, the fluid velocity becomes zero faster than our data acquisition rate. This fast shutoff ensures that the fluid velocity is zero for the subsequent movie frames and is important for our calculation of persistence time of filament orientation.

2.2 Preparation of surfaces

Sliding motility assays of myosin V and actin (Cheney, 1998) were performed in the microfluidic channels. Proteins were injected to the channel using a syringe pump at a volumetric flow of 40 μl/min in the following order. Low concentrations of BSA (10 μg/ml) to pre block the surface, myosin V (2 μg/ml), high concentration of BSA (2 mg/ml) to completely block the surface. Actin (10 nM) was injected more slowly at 10 μl/min to avoid shredding the filaments. Upon injection of ATP (2 mM) at different flow rates (Table 3.1) myosin motors moved toward the positive end of actin and in the process "slide" the filaments with its negative end as the leading end.

Channel Average Velocity(mm/s)	Local velocity at 120nm (μm/s)	Local velocity at 20nm (μm/s)	Drag force ∥ at 20nm (pN)	Drag force ⊥ at 120nm (pN)
1.85	24.2	4.0	0.012	0.081
3.7	48.4	8.0	0.024	0.16
5.55	72.7	12.1	0.036	0.24
7.4	96.9	16.1	0.048	0.32
9.25	121.2	20.0	0.06	0.40

Table 3.1. The above table shows the drag force on a 1.1 micron long filament aligned parallel and perpendicular to flow at different flow rates. The average velocities are calculated from our measured volumetric flow rate using our channel dimensions (60 μm height, 750 μm wide). The local velocities are calculated assuming laminar flow in the channel, at the indicated height above the surface.

2.3 Estimation of surface motor density

It is important to know the surface density of the myosin motor proteins on the surface to gain insight of the dynamical model of the motility assay. To set a bound on this quantity, we injected pre block BSA and myosin into the channel as explained in the methods section. The channel was then flushed three times with 100 μls of buffer to remove non-adherent proteins. The proteins bound to the channel surfaces were then eluted with high concentrations of SDS and the outflow was collected. A western blot of 2μl samples of the outflow from concentration ranging from 1:1 to 1:1024, at 1-1/2 serial dilutions were performed against myosin V antibody on a nitrocellulose membrane. A positive control of 2μl samples of myosin V from 1 μg/ml to 1 ng/ml, at 1-1/2 serial dilutions and a negative control of BSA was blotted on the same membrane. The signal from the outflow, on comparison with the signal from known concentration of myosin V, gave an estimate of 10^{10}

myosin V dimers in the channel which equates to a motor density of $280/\mu m^2$. Since some of the motors, upon contact to the surface, lose their enzymatic activity, the over all density of working motors might be significantly lower than our estimate of $280/\mu m^2$ through Western blot.

2.4 Data acquisition and analysis

The experiments were observed using a Nikon Diaphot 200 inverted microscope with epi-fluorescence attachments, and images were collected using a Spot 2 cooled-CCD camera. MetaMorph (Universal Imaging Co.) was used to operate the camera, perform image processing and analysis. Frame capture rate of our camera was one frame every 3 seconds. A Matlab code custom written in our lab was used to obtain the angular alignment of filaments. The program allows the user to choose 2 points in the image. An output file is generated with the length and angle subtended by the line joining these 2 points. The angle subtended by the straight line joining the tail end and the leading end was measured as the angular alignment of the filament. Flow direction was taken as the reference for $\theta = 0$.

3. Theory

3.1 Theoretical analysis of sliding filament assay

The trajectory followed by the filaments in a sliding motility assay resembles that of a random walk. The path of a filament is characterized by periods where it is bound to multiple motors and therefore undergoes linear motion, and periods when it is bound to a single motor exhibiting rotational diffusion. The filament orientation becomes uncorrelated in alignment due to rotational diffusion when bound to a single motor (Duke et al., 1995; Faretta and Basetti, 1998). The path of the filament is dependant on the surface motor concentration and filament length and rigidity. To estimate the surface concentration of working motors, we

49

perform an analysis on the assay similar to Duke et al's analysis of the kinesin- MT motility assay. The motors are assumed to be randomly deposited on the surface with a surface concentration of σ. The motors are assumed to be capable of reach isotropically over a distance $w = 60$nm (half height of m5) to interact with the actin filaments. The actin filaments are considered to have a persistence length of $L_p=17$ µm (Gittes et al., 1993), filament length of $L=1.1+/-0.2$ µm, and an average speed $v=276\pm70$ nm/s and diffusion parameter $\gamma=kT/\eta$. Here k is the Boltzmann constant, T, the temperature and $\eta$the viscosity of the fluid. Suppose that the length of the leading end of the filament beyond that last bound motor is l, and explores an area $A(l)$ of the surface to bind motors. (*i*) For short l, there is no appreciable bending and only motors in the path w of the filament bind to it and hence the area $A\sim wl$. (*ii*) For intermediate l the filament can bend due to thermal agitation given by θ_{eq} $\sim (l/L_p)^{1/2}$, such that $A\sim l^2\theta_{eq} \sim l^{5/2} L_p^{-1/2}$. (*iii*) For long l the end can bind a motor and advance forward before it bends to θ_{eq} and thus $A \sim l^2\theta \sim (\gamma/v)^{1/2}l$. For the three regimes, the mean distance d is specified by the condition $\sigma A(l = d) = 1$. The d values for the three regimes are

$$
d \sim \begin{cases} \sigma^{-1}w^{-1}, \sigma >> \sigma*, \\ \sigma^{-2/5}L_p^{1/5}, \sigma* >> \sigma >> \sigma**, \\ \sigma^{-1}(\gamma/v)^{-1/2}, \sigma** >> \sigma, \end{cases}
$$

The boundary values for the regimes are $\sigma*\sim w^{-5/3}p^{-1/3} = 86/\mu m^2$ and $\sigma**\sim(\gamma/v)^{-5/6}p^{-1/3}$ $=0.04/\mu m^2$ for our assay. When a single pivot is positioned anywhere on the filament of length L with equal probability, the area $A = \frac{1}{3}L^2\langle\Delta\theta\rangle$. For a given inter motor spacing d, the mean angle of swivel (bound to single motor) and the mean distance the filament travels

between successive rotations (when bound to multiple motors) can be calculated using the

formulas $\langle \Delta\theta \rangle = 3\sigma^{-1}L^{-2}$ and $s = \dfrac{L+2d}{L+3d}\dfrac{d^2}{L}\left(e^{\frac{L}{d}}-1-\dfrac{L}{d}\right)$ respectively. The persistence

length P of path of the filament can be calculated as $P = \left(L_p^{-1} + \dfrac{\langle \Delta\theta \rangle^2}{s}\right)^{-1}$. Four time scales

can be defined for the motility of an actin filament, τ_{linear}, τ_{rot}, τ_{diff} and, τ. We can define the

path of a motile filament in terms of the time required for each of the individual steps. The

time duration of linear motion of a filament (τ_{linear}) is the time of linear motion or travel

between successive rotations. The filament is bound to multiple motors during this time. The

time for rotational motion (τ_{rot}) is the time that the actin filament is bound to a single motor

and undergoes rotational diffusion before binding more motors. The rotational correlation

time (τ_{diff}) is the time required for an actin filament bound to a single motor to become

uncorrelated via free diffusion in the absence of motors nearby. The persistence time (τ) is

the time taken by the filaments to become uncorrelated, or lose memory of their previous

alignment. These time scales provide useful information about the motors and filaments and

the assay in particular.

τ_{linear} is the time of travel between successive rotations and equals $\tau_{linear} = \dfrac{s}{v}$ [3]. According to

the differential law for Brownian motion, the mean square angular random deviation of the

infinitesimal angle $\Delta\theta$ by which a vector bound to a particle rotates in a plane during the

time interval Δt is given by $\langle \Delta\theta^2 \rangle = 2D_{rot}\Delta t$, where, the rotational diffusion coefficient is

given by $D_{rot} = \dfrac{3kT}{4\pi\eta(L_1^3 + L_2^3)}Cosh^{-1}\left(\dfrac{h}{r}\right)$ for a rod of radius r height h above the surface and

pivoted at a distance L_1 from one end.. The mean angle of swivel when fastened to one motor

equals $\langle \Delta\theta \rangle = 3\sigma^{-1}L^{-2}$. Hence, the time ($\tau_{\text{rot}}$) that the actin filament is bound to a single motor

and undergoes rotational diffusion before binding multiple motors is given by

$\tau_{rot} = \dfrac{9}{2}\sigma^{-2}L^{-4}D_{rot}^{-1}$ [4]. The anisotropy of an initially oriented population of particles, decays

exponentially with a rotational correlation time τ_{diff} (Carrington and McLachlan, 1967) given

by $\tau_{diff} = \dfrac{1}{3D_{rot}}$ for one degree of rotational freedom [5].

3.2 Alignment energy of filaments

The energy of alignment of a filament is a sum of the energy of state of motors

attached to it, energy of bending of filament and the drag force acting on the filament. Motors

can be considered as springs with very low torsional spring constants and hence the energy

due to motors can be neglected. The average length of filaments in our assay equaled 1.1µm,

well below the persistence length of actin (17µm). Hence thermally induced filament shape

fluctuations are minimal. The bending rigidity of the filament is higher than the rotational

rigidity of the motor. When a torque is applied to a filament bound to a single motor, it will

rotate about the frictionless pivot like a rigid rod. Thus, for the purpose of our model, when a

filament is bound to a single motor, we can consider the filaments to be rigid and assume

alignment takes place due to motor rotation rather than due to filament bending.

3.2.1 Energy of a filament bound to single motor

When the filament is attached only to one motor, filament energy at an angle θ can be

equated to the work done by the filament against drag to rotate to an angle θ. The work done

is given by

$$W = \int_{\theta}^{0} \tau(\theta) d\theta$$

where, τ is the torque acting on the rod. Assuming the drag force acts at the center of mass of a uniform rod, the torque about the pivot point is $\tau(\theta) = F \times \dfrac{L}{2}$, where F is the drag force and L is the length of the rotating end of the rod. When a rod pivots about a point such that L_1 and L_2 are the length of the subunits, the clockwise and counter clockwise torques equal $\tau_1(\theta) = F_1 \times \dfrac{L_1}{2}$ and $\tau_2(\theta) = F_2 \times \dfrac{L_2}{2}$. The net torque equals $\tau = \tau_1 - \tau_2$. The drag coefficient of a cylinder at a height h above the surface with its long axis perpendicular to direction of motion

$$F_D = \frac{4\pi\eta L}{\cosh^{-1}\left(\dfrac{h}{r}\right)}$$

The velocity perpendicular to filament is $v \sin\theta$. The torque on a rod about its pivot is then equal to

$$\tau(\theta) = \frac{2\pi\eta v \sin\theta (L_1^2 - L_2^2)}{\cosh^{-1}(\dfrac{h}{r})}$$

The work done against flow while rotating to an angle θ is given by

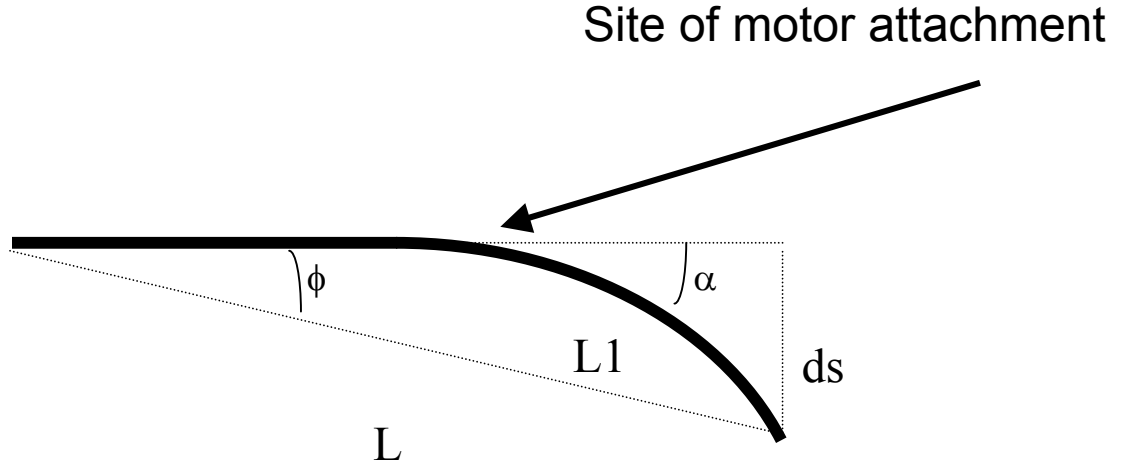$$W = \int_{0}^{\theta} \frac{2\pi\eta(L_1^2 - L_2^2)v\sin\theta}{\cosh^{-1}(\dfrac{h}{r})} d\theta$$

$$W = E^f(\theta) = \frac{2\pi\eta(2LL_1 - L^2)v(1 - \cos\theta)}{\cosh^{-1}(\dfrac{h}{r})} \quad [6]$$

where, L is the length of the rod.

3.2.2 Energy of a filament bound to multiple motors

When a filament attaches multiple motors, it is pinned down at motor locations and the leading end of the filament is susceptible to thermal fluctuations (figure 3.3).

Figure 3.3. Schematic of a filament of length L bent an angle α. The length of the subunit beyond the last point of motor attachment is L_1.

Its energy is the sum of elastic restoring force of bending as well as drag. The elastic energy of the filament is given by $E_s = \frac{1}{2}k(ds)^2$ where k is the spring constant of the filament and ds

the deflection. $k = \frac{3L_p KT}{L_1^3}$ where, L_1 is the length of bending end the filament, Lp is the persistence length and K is the Boltzmann constant, T the temperature and $ds = L\sin\phi$.

$$E_s = \frac{3L_p kTL^2 \sin^2 \phi}{2L_1^3} \quad [7].$$

Using eqn. [7] we can calculate that a 1 micron actin filament pinned at the center will bend by a maximum angle of 2^0. The drag force acting on L1 equals

$$E_d = \frac{2\pi\eta L_1^2 v(1 - \cos\theta)}{\cosh^{-1}(\frac{h}{r})}$$

The total energy equals

$$E^f(\theta) = \frac{3L_p kTL^2 \sin^2 \phi}{2L_1^3} + \frac{2\pi\eta L_1^2 v(1 - \cos\theta)}{\cosh^{-1}(\frac{h}{r})} \quad [8]$$

If the filament were flow aligned before bending, then $\phi = \theta$.

4. Results

Actin filaments in the channel adhered to the myosin substrate and were motile in the presence of ATP. Individual actin filaments (n~15) were tracked with MetaMorph imaging software. The average filament velocity was found to be 276 ± 70 nm/s, equal to the processive motor velocity of myosin V as previously observed at this ATP concentration of 2mM (Mehta et al., 1999). When external flow was applied at velocities given in table 3.1, the filaments continued motility at normal velocities (Figure 3.4). The flow in the channel did however orient the actin filaments and steer them in the direction of the flow (Figure 3.5). The filaments that started to move against flow were observed to turn in the direction of the flow and continue directed motility in the flow direction.
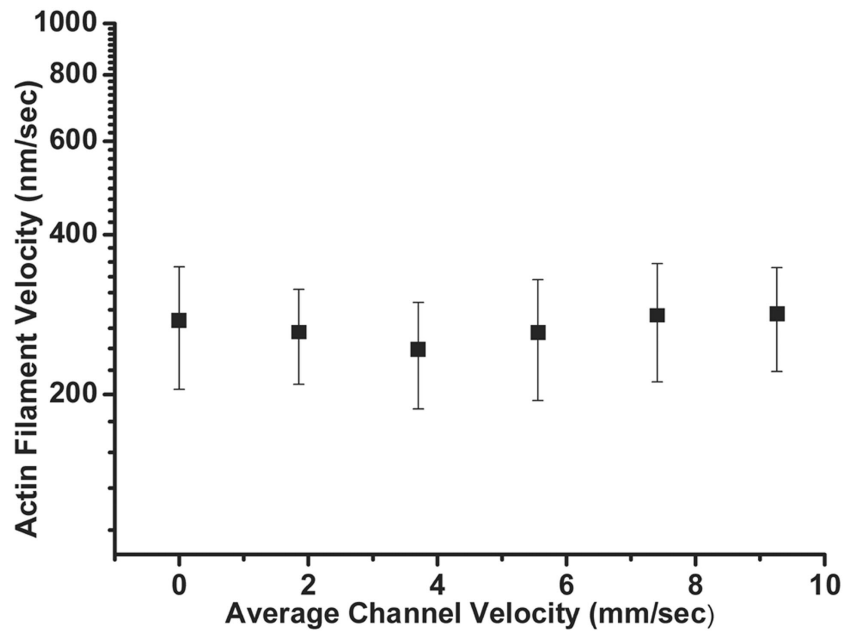
Figure 3.4. Sliding velocity of actin filament measured at varying average buffer velocities applied in the channel. The velocity of filaments does not change with the external flow indicating that flow does not affect motor velocity.
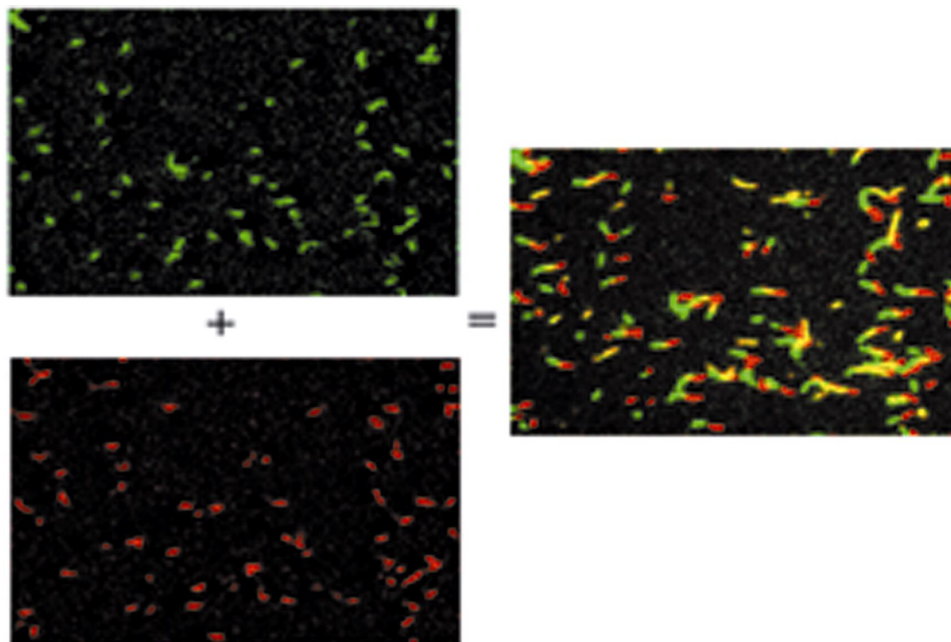
Figure 3.5. The top left image, colored green, shows the fluorescent actin filaments in one frame (t=0), while the image below, colored red, is the filament image one frame later (t=3s). The composite, color combined image shown at right, is an overlay of these two images. The motile actin filaments are seen as colored green to yellow to red and non-motile filaments are entirely yellow in color. The red end is the leading end and the green end the trailing end of a filament. A large percentage of the filaments have their leading end pointing downstream. This shows that flow aligns motile filaments downstream.

We generated histograms of the distribution of the filament alignment at different flow rates (Figure 3.6).
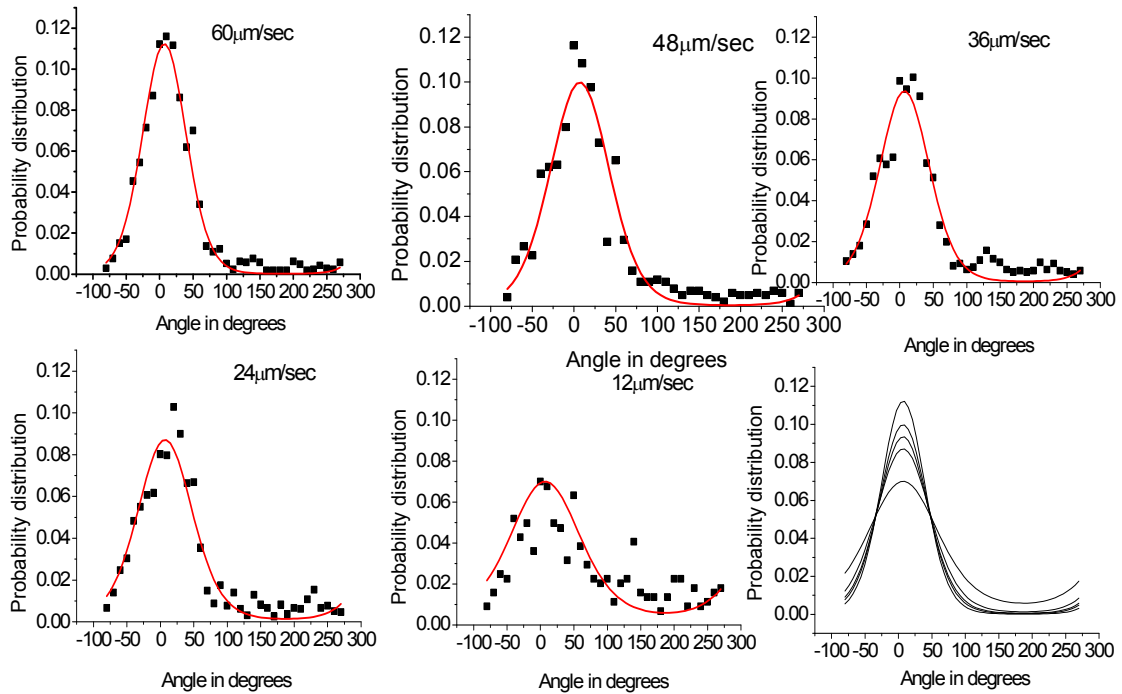

Figure 3.6. The probability distribution of alignment of filaments measured from experiments for different flow rates is plotted above (squares). The solid lines are curve fits of equation 6 to the experimental data. The histograms of filament alignment have a peak at

zero degrees clearly indicating that filaments align downstream. The width of the filament distribution decreases with increasing flow rates. This shows that filament alignment improves with higher flow rates.

The width of the filament distribution narrows with an increase in the flow velocity. This shows a direct correlation between external flow and filament alignment. Higher flow velocities generate higher torque on the filaments, align the filaments more successfully reducing the width of the distributions in figure 3.6. We reversed the flow multiple times during the experiment. Upon flow reversal, the filaments turned around to undergo motility in the reverse direction. Figure 3.7 compares the histograms of the filament distribution before and after the flow reversal.
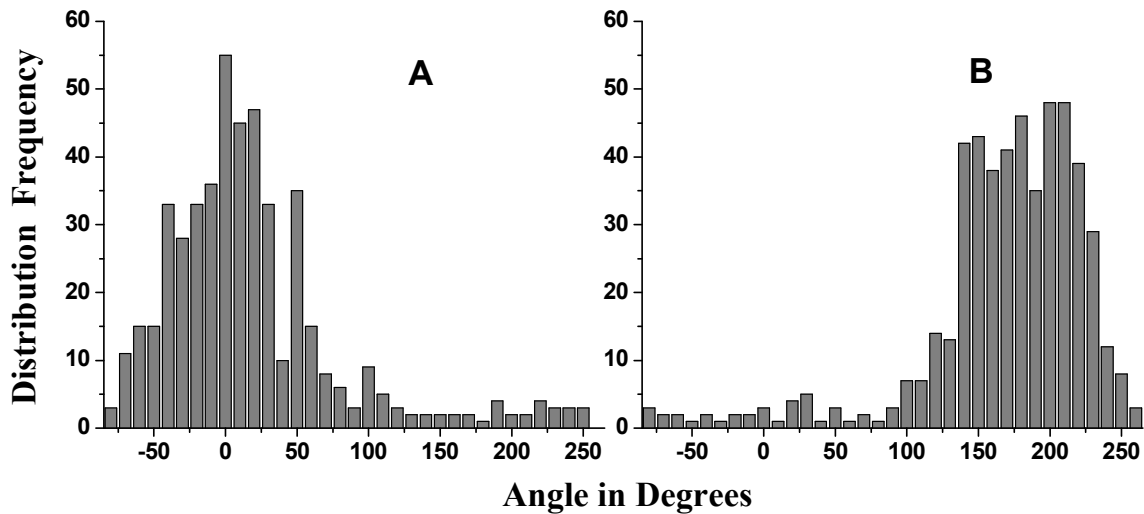
Figure 3.7. Reversal of filament motility direction by switching flow direction: Figure A shows majority of filaments with a 0^0 alignment when flow direction was towards 0^0. In figure B, when the flow was reversed, majority of filaments turned to align with flow at 180^0. The applied flow rate at a height of 60nm equals 28µm/sec.

After the external flow was stopped, the filaments lost their alignment and resumed a random motion. The angle of alignment of actin filaments (n=101) was measured over five consecutive movie frames. The first frame (t_0=0s) was the flow-aligned state and flow was absent in the consecutive frames (t=3s, 6s, 9s, 12s). The covariance or time correlation of alignment of the system of filaments at the initial time t_0 to a later time t is given by $\sigma_{0t}(t) = \langle \theta(0)\theta(t) \rangle - \langle \theta(0) \rangle \langle \theta(t) \rangle$. Here, $\theta(0)$ and $\theta(t)$ are the angular alignments of filaments at times zero seconds and t seconds respectively. Correlations of the angular alignment of filaments at times t_0 = 0s to t = 3s, 6s, 9s and 12s were calculated. This correlation decays with time as the filaments lose their original alignment. The graph of correlation Vs time for t = 0 to t = 12s plotted in figure 3.8 shows a decay in the correlation with time.

$$y = A1*\exp(-x/\tau)$$
$$\tau = 7.2 \pm 0.93s$$
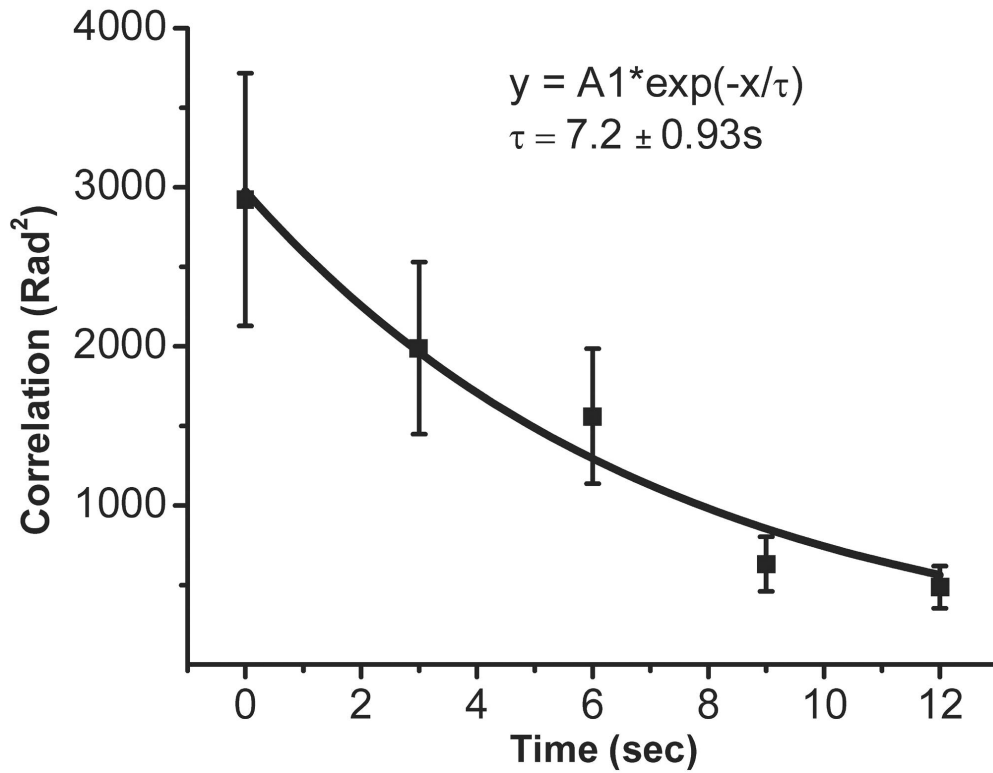
Figure 3.8. The graph of correlation in alignment Vs time (t = 0 to t = 12s) plotted here for hundred filaments shows a decay in the correlation with time. An exponential decay curve fit to this plot provides the value for persistence time for the system (τ = 7.2 +/- 0.93 s).

5. Discussion

5.1 Drag force on the filament

From our results (figure 3.4), we see that the velocity of the filaments moving in the flow direction was unaffected by the drag force. This result is not surprising, as, external forces are not expected to increase step velocity of processive motors. The motor velocity is determined by the step size and the catalytic rate of the motor protein. The absence of velocity increase in a processive motor in the presence of a forward load has been observed previously in the case of kinesin using laser tweezers (Block et al., 2003). The drag force acting on the filaments can be calculated as $F = C_D v$, where C_D is the drag coefficient and v is the velocity of the object, or in our case the flow outside a stationary cylinder. The C_D of a cylinder of length L, radius r and at a height h above the surface in a fluid of viscosity η, aligned with its long axis parallel to the direction of motion (or flow) and perpendicular to motion (or flow) are respectively given by (Landau and Lifshitz, 1987; Hunt et al., 1994)

$$C_{\parallel} = \frac{2\pi\eta L}{Cosh^{-1}\left(\dfrac{h}{r}\right)} \; ; \; C_{\perp} = \frac{4\pi\eta L}{Cosh^{-1}\left(\dfrac{h}{r}\right)} \quad [9]$$

The drag force on an actin filament with an average length L was calculated using Eq.[9] and tabulated in table 3.1. AFM imaging of myosin V estimates the motor to extend to ~ 120nm in height (Ando et al., 2001) which was taken to be the maximum height h at which filaments can undergo myosin V motility. The velocity of fluid in the channel at this height h = 120 nm

was calculated using Eqn.[1]. This would be the maximum velocity that actin filaments experience in our channel. The average length of $L = 1.1+/-0.2$ µm (measured) and radius $r = 4$ nm were used for the actin filaments. A values of $\eta = 10^{-3}$ Ns/m^2 was used for the viscosity of water as the experiments were performed in aqueous buffer. The maximum drag force acting on a 1.1 µm long filament at a fluid velocity of 120 µm/s is calculated as 0.40 pN (table 3.1). Since the stalling forces measured for myosin V are approximately 3 pN (Mehta et al., 1999), these values of drag forces are not expected to be capable of stalling the motion of actin or detaching the filament from the motor. In fact, we observe the filaments that initially move upstream never stall and eventually turn around to continue motility down stream. Thus, flow polarizes a randomly oriented set of motile actin filaments.

5.2 Dynamics of the filament

As discussed previously in section 3.1. Four time scales can be defined for the motility of an actin filament, τ_{linear}, $\tau_{rot,}$ τ_{diff} and, τ. Persistence time τ of a system can be defined as the time over which the system retains memory of its original alignment at t = 0. The distance P that the filament travels in this time is the persistence length of its path. We calculated τ from the graph of correlation vs time of angular alignment of filaments (figure 3.8). This correlation decays with time according to $Ae^{(-t/\tau)}$, where τ is the correlation time or persistence time(Gardiner, 1983;VanKampen, 1981). An exponential decay curve was fit to the graph of correlation vs time and we obtained a persistence time of 7.2 ± 0.93 s. The persistence length of the path P, which is the mean distance traveled by the filament in this time is calculated to be $P = 1.98 \pm 0.55$µm. Using the information about filament properties (length and rigidity) we can calculate the motor density from persistence time (Duke et al, 1995). Given that the measured average filament length is 1.1±0.2 µm and the persistence

length of phalloidin labeled actin filaments is 17.7 ± 1.1 μm (Gittes et al., 1993) we calculate the motor density to range from $\sigma = 2/\mu m^2$ to $\sigma = 8/\mu m^2$. This large range is due to the range in filament length as well as the error in persistence length. The mean motor density of $\sigma = 5/\mu m^2$ will be used for subsequent calculations and discussions. The motor density in our assay falls in the range $(\sigma^* \sim w^{-5/3} p^{-1/3} = 86/\mu m^2) > \sigma = 5/\mu m^2 > (\sigma^{**} \sim (\gamma/v)^{-5/6} p^{-1/3} = 0.04/\mu m^2)$. The average inter-motor spacing equals $d = \sigma^{-2/5} L_p^{1/5}, \sigma^* \gg \sigma \gg \sigma^{**}$ which equals 0.9μm. As suspected, the concentration of functional motors is around 3% of the total motor concentration in the channel. The estimation of the density of functional motors obtained via western blot includes denatured proteins and motors that orient themselves in configurations that do not sustain actin motility (Mehta et al., 1999; Howard et al., 1989). This surface density suggests that a filament during motility is bound to multiple motors a majority of its time interspersed with short time periods when it is bound to a single motor. The diffusive rotational correlation time (τ_{diff}) is the time required for the filament to become uncorrelated by rotational diffusion. For a 1 micron long rigid rod, rotating at its center about a stationary pivot, $\tau_{diff} = 33$ ms (Eqn. [5]). If all the filaments were bound only to single motors, it would take the filaments only 33 ms to become uncorrelated. A persistence time much longer than the diffusive rotational correlation time shows that the filaments spend a majority of their time bound to multiple motors following a linear path. We proceed to calculate the mean time spent by an actin filament bound to multiple motors (τ_{linear}) and single motor (τ_{rot}) for a surface motor density of $\sigma = 5/\mu m^2$. A 1.1 μm long filament will be bound to multiple motors and undergo linear motion for approximately $\tau_{linear} = 2.34$s (Eqn. [3]). After this time it loses contact with its second motor and is singly bound. It is now free to rotate diffusively till it comes into contact with a second motor through rotation. At our motor density, a rigid

actin filament will undergo rotational diffusion and turn through an angle of $\langle\Delta\theta\rangle = 0.5$ radians before contacting a second motor. The average time required for the filament to rotate by diffusion through this angle can be calculated as $\tau_{\text{rot}} = 12.2$ ms (Eqn. [4]) which is less than the diffusion correlation time for a free rotor $\tau_{\text{diff}} = 33.0$ ms. It is interesting to note that the filament needs ~ 3 rotational steps to become uncorrelated. Since the path of a filament is characterized by periods of linear motion and rotational diffusion, the filament would have taken a total of 3 linear steps and the time it takes is given by $3 \times \tau_{linear} + 3 \times \tau_{rot} \sim 7s$ which is approximately equal to the measured persistence time.

5.3 Analysis of filament distribution

5.3.1 Orientation of filaments

Application of an external flow changes the dynamics of the filaments. Drag forces work against the diffusive motion of the filaments and align them along the flow direction. This probability distribution of alignment can be represented by a classical Maxwell-Boltzmann distribution in terms of the energy of the system. We expect the probability of a non-motile actin filament to align at an angle θ to equal $p(\theta) = Ne^{\frac{-E(\theta)}{kT}}$, where, N is a normalization constant, *E(θ)* is the energy of the filament at an angle of alignment *θ*, k is Boltzmann constant and T is the temperature. We consider the energy *E(θ)* of the filament to depend on the mechanical properties of the filament and bending constraints imposed by the motors that are bound to the filament.

Considering the case when a filament binds multiple motors, filament conformation is pinned at the location of the motors. The only bending mode available to the filament is the subunit extending beyond the last bound motor bends due to thermal energy. The alignment energy

of the filament in this case is due to the elastic restoring force of bending, given by,

$$E_s(\theta) = \frac{3L_p kTL^2 \sin^2 \theta}{2L_1^3}$$ (Eqn. [7]), where, L is the length of the filament, L_1 is the length of

the filament extending beyond the last bound motor, Lp is the persistence length of actin, k is

the Boltzmann constant, and T is the temperature. Here, the initial alignment of the filament

with the pointed end aligned with $\theta = 0$ is considered as the reference angle. With this energy

term, we calculate using Matlab the orientation probability distribution of the pointed end for

a set of n = 100 filaments with length distribution of 1.1+/-0.2 μm, initial orientation $\theta = 0$

and motor positions distributed with equal probability along the length of the filament. The

distribution obtained had a sharp peak with a FWHM of 5 degrees. This is consistent with

our understanding that when bound to multiple motors, thermal forces have to bend the short

filament subunit and therefore fluctuations are minimal. Hence the path of the motile

filament when bound to multiple motors is predominantly linear. When external flow is

applied, the restoring force increases due to the additional torque imposed by flow. The

alignment energy term in this case equals

$$E^f(\theta) = \frac{3L_p kTL^2 \sin^2 \theta}{2L_1^3} + \frac{2\pi \eta L_1^2 v(1 - \cos\theta)}{\cosh^{-1}(\frac{h}{r})}$$ (Eqn. [8])

Where, η and v, are the viscosity and velocity of fluid in the channel. The variable h is the

height at which actin filaments are held in the channel and r, is the radius of the actin

filament. Here, flow direction is taken as the reference angle $\theta = 0$. Calculations were done in

Matlab as before to obtain probability distribution of the pointed end of n =100 filaments,

originally aligned with their pointed end downstream and held by myosin V at a height of 60

nm (half height of myosin) above the surface. At the maximum flow rate applied, the FWHM

of the probability distribution reduced to 4 degrees. There is only a 1 degree increase in filament alignment when flow is introduced. Thus, when bound to multiple motors, the elastic restoring force of the filament alone is capable of maintaining filament alignment and additional torque due to flow does not effect alignment substantially.

Considering the next case, when bound to a single motor, filaments gain another degree of freedom and can rotate diffusively about its pivot (motor) through an angle of 360 degrees. Upon introducing external flow, rotation is suppressed and the filaments align with flow. The energy of the filament is now given by (Eqn. [6])

$$E^{f}(\theta) = \frac{2\pi\eta(2LL_1 - L^2)v(1 - \cos\theta)}{\cosh^{-1}(\frac{h}{r})}$$

L is the length of the filament, L_1 is the length of the leading subunit extending beyond the bound motor, and $L_2 = L - L_1$ is the trailing subunit. We can now express the probability distribution of alignment by the exponential $P(\theta) = Ne^{-\frac{(1 - \cos\theta)}{\delta}}$, where N is a normalization constant and $\frac{1}{\delta} = \frac{C_\perp(2L_1 - L)v}{2k_BT}$. Using Matlab, orientation distributions of the pointed ends of n=100 non –motile actin filaments attached to a single pivot (motor) in the presence of external flow was obtained. The length of the filaments was 1.1+/-0.2 μm. Motor positions were distributed with equal probability along the length of the filament. Here, flow direction is taken as the reference angle θ = 0. We obtain from our calculations two equal distribution peaks, one at zero degrees downstream and another at 180 degrees upstream. This means that the pointed end of the set of filaments aligns downstream or upstream with equal probability. This is contrary to the single peak at zero degrees that we observe with filaments pointing

down stream. This symmetry in peaks is due to the distribution of motor positions on the filament. Looking back at the energy equation (eq [6]), when $L_1 > L/2$, the energy $E^f(\theta) \propto (1 - \cos\theta)$, when θ tends to zero, the energy is minimum and the probability $P(\theta)$ tends to the maximum value resulting in a peak at zero. Filaments align with their pointed end downstream. But when $L_1 < L/2$, the energy $E^f(\theta) \propto (\cos\theta - 1)$, when θ tends to 180^0, the energy is minimum and the probability $P(\theta)$ tends to the maximum value resulting in a peak at 180^0. When the length of the leading end of the filament L_1 is greater than L_2, the filament aligns with its pointed end pointing down stream resulting in a peak at zero. In our calculations, filaments are stationary and the motor binding site can be anywhere along the filament length with equal probability, such that, $L_1 > L/2$ and $L_2 > L/2$ are equally probable. When a dynamic filament is considered, the motor binding site moves toward the barbed end as the filament is propelled forward and the leading end becomes longer. This travel of the motor attachment site increases the probability of $L_1 > L/2$, resulting in the asymmetry of the peaks in our experiments. It is therefore necessary to consider the dynamics of the filament to improve the current model. In the following section, using the current model we describe the increase in filament alignment with increasing flow rates and calculate the average value for length L_1 of the filament subunit.

5.3.2 Narrowing of the width of filament distribution

Apart from the filaments aligning with flow, we also observe that the peak of the distribution becomes narrower with an increase in the flow rate. In the probability distribution function $P(\theta) = Ne^{-\frac{(1-\cos\theta)}{\delta}}$, the width of the filament distribution is determined by the alignment factor δ. The FWHM for the distribution in our experiments ranged from

125^0-75^0 for the range of flow rates used (figure3.6). The orientation distribution equation

$$P(\theta) = Ne^{-\frac{(1-\cos\theta)}{\delta}}$$ was fit to the experimentally obtained angular distributions at different

flow rates (Figure 3.6). From the curve fits, we obtained value of fitting parameter δ for different flow velocities. The width of filament distribution δ reduced with increasing flow indicating better alignment at higher flow rates. Parameter δ was plotted against v, the channel velocity at 60 nm (Figure3.9).
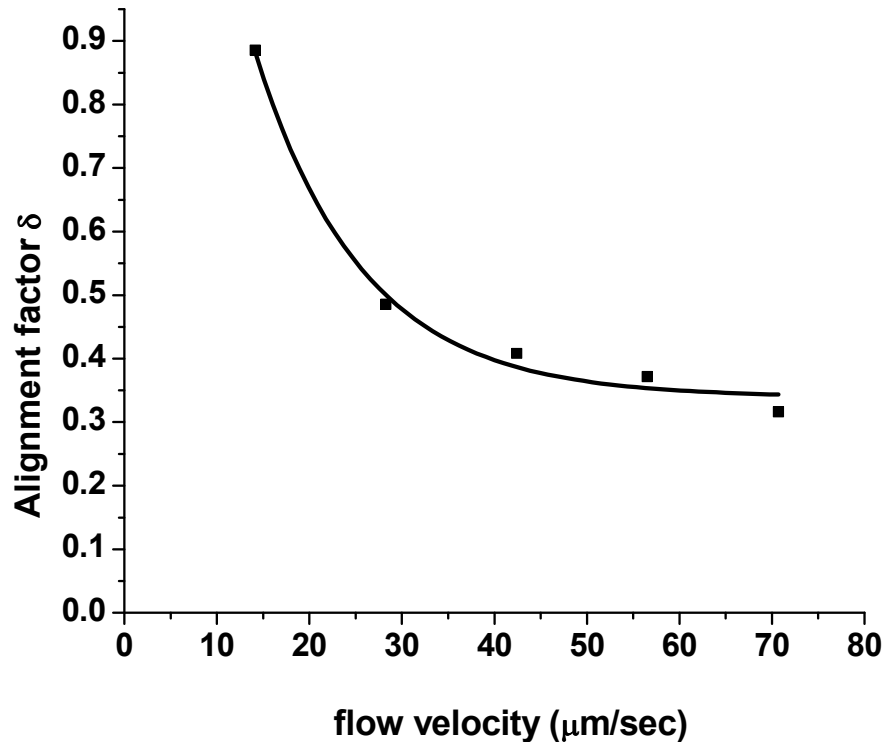
Figure 3.9. Alignment factor δ plotted against v, the channel velocity at 60nm. The width of the distribution decreases with increasing flow rate but saturates after velocity of $\sim$ 60μm/sec.

From the plot we can see that filament alignment increases with increasing flow rates but saturates at higher flow rates indicating that there is an inherent randomness to the system.

We then plot Parameter δ against 1/*v*, the inverse channel velocity at 60nm and fit to a line (Figure 3.10).

$$\delta = \delta min + S*1/v$$
$$\delta min = 0.17494 \pm 0.02221$$
$$S = 9.85929 \pm 0.58044$$
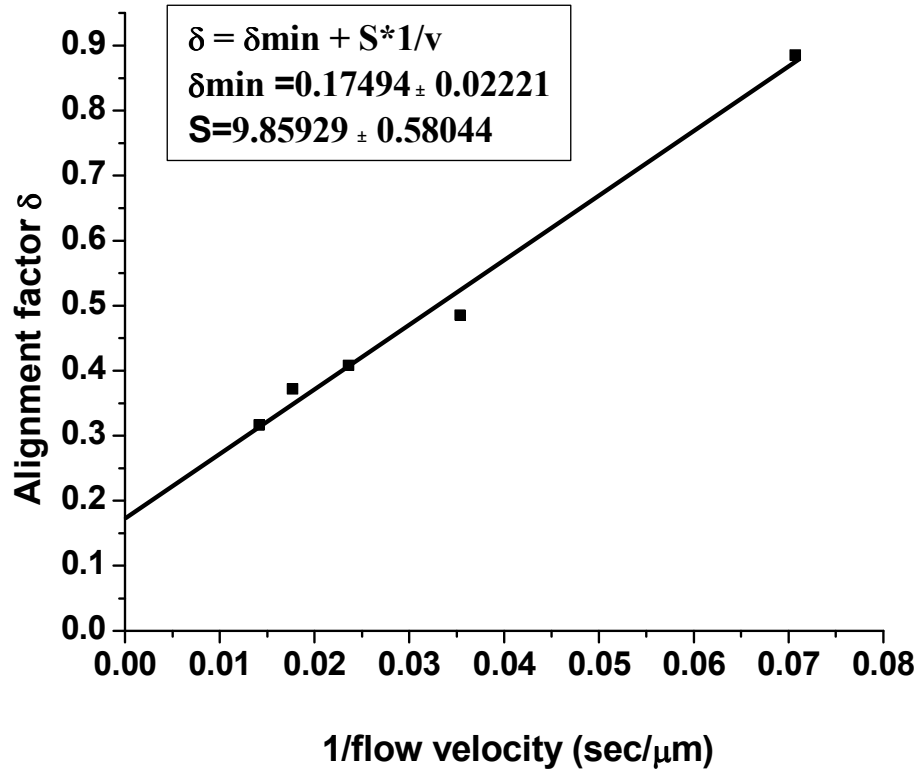
Figure 3.10. Alignment factor δ plotted against 1/*v*, the channel velocity at 60nm is fit to a line. This indicates that filament alignment increases with increase in flow rate but saturates at high flow rates due to the inherent randomness of the system. The intercept of this line δ_{min} indicates this randomness.

The intercept δ_{min} = 0.17 from the fit indicates the inherent randomness of the system, implying that at infinite fluid velocity, the width of the distribution δ does not become zero. Value of δ = 0.17 corresponds to a FWHM of 50^0, the narrowest possible filament distribution for this assay. Alignment parameter δ is a function of viscosity, square of

filament length, average channel velocity, height of filament above the surface and length of the leading subunit extending beyond the bound motor. From the slope in figure 3.10, assuming known value of $\eta = 10^{-3}$ Pas for viscosity of water, measured average actin filament length of 1.1 μm for actin, L_1 the average length of the leading subunit extending beyond the bound motor can be calculated to be 0.64 μm.

6. Conclusions

6.1 Flow forces in the Cytoplasm

Our observation of filament alignment and directed motility by flow in vitro opens up the possibility that drag forces might be crucial in the organization of cytoskeletal filaments and motor proteins within the cell. Drag forces can act on filaments when they are transported and arranged by motors (mitotic spindle formation) or due to cytoplasmic flow (formation of pseudopodia). We observe that for effective flow induced alignment in vitro, flow velocities greater than 50 μm/s producing torques greater than 100 pN nm on a micron long filament is required. We note that it is the product of velocity and viscosity that gives rise to the drag and torque. In our channel at a maximum velocity of 70 μm/s, the product of velocity and viscosity has a value of $7X10^{-5}$ pN/nm. Flow velocities in vivo are lower than the flow velocities used in our experiments, but in vivo viscosities are much higher. The highest motor velocity in vivo has been measured to be approximately 15um/sec (Kural et al., 2005). Plasma streaming in large internodial cells of Characeae is measured to be around 60 μm/s (Kersey et al., 1976;Wanka and Van Zoelen, 2003). Measurements of intracellular viscosities provide values that range from 38.2 Ns/m^2 to 210 Ns/m^2 (Bausch et al, 1998),(Yamada et al., 2000).The values for the velocity-viscosity product in the cytoplasm range from $3.8X10^{-2}$ to $21.0X10^{-2}$ pN/nm. These values are up to 3 orders of magnitude

higher than in our in vitro experiments. Therefore, lower flow rates in the cytoplasm can apply higher drag forces and could bring about the same phenomena of filament orientation. Future experiments will include observing effective steering at lower velocities and higher fluid viscosity by adding methyl cellulose to our buffer. Cytoplasm is a complex fluid whose viscosity is a result of high protein concentration as well as the mesh network of cytoskeletal filaments. As a result, the viscosity is most likely length scale and frequency dependant. A smaller particle might be more mobile than a larger particle in a viscoelastic fluid and hence "feel" a lower viscosity. A rod like particle which has two length scales, diameter and rod length, might probe a complex fluid in a different manner than a spherical particle. To try to answer what viscosities microtubules and actin feel, we undertake in the next chapter a study of rod diffusion in viscous and viscoelastic fluids.

CHAPTER IV

Diffusion of Cylindrical Particles in Viscous and Viscoelastic Fluids

PREFACE

Motility and transport processes within biological systems takes place due to the coordinated efforts of cytoskeletal filaments and motor proteins. However, all this work is done in highly viscous and viscoelastic fluids against drag forces. The diffusion coefficient of a particle is related to the drag coefficient through the generalized Stokes- Einstein equations discussed in detail in this chapter. Therefore, by observing the thermal motion of particles in a fluid, the drag forces acting on the particle can be obtained. To study these drag forces inherently affecting the mobility of biological particles, rod-like particles in particular, we observed the thermal motion of gold nanorods and microtubules in Newtonian and complex fluids. Complex fluids contain colloidal structures with a characteristic length scale which give rise to the elasticity of the fluid. The complex fluid can be treated as a continuum around a particle only if the length scales of the colloidal structures are smaller than the size of the particle. Thermal motion in complex fluids is therefore dependant not only on the viscoelastic properties but also on the length scale of the mesh network. Due to their small diameter, rods encounter the mesh network less frequently when they move axially and normally. However, due to their length, their rotational motion is restricted by the mesh. This could mean that microtubules, actin, organelles like mitochondria, pathogens like Tobacco mosaic virus and Listeria are all restricted in their rotational motion within the cytoplasm more than axial or normal motion. This has implications to cytoskeletal and organelle organization, restriction of DNA mobility for gene delivery applications and pathogen motility within cells. The observations presented in this chapter could also have implications in the efficacy of using rod like particles in drug delivery.

1. Introduction

Biological filaments like actin, microtubules, cilia, fibrin, are all under the influence of highly viscous and viscoelastic fluids like cytoplasm, blood and serum. Ion transport, muscle contraction, cell division, molecular motor motility, and mucociliary clearance, are affected by viscous drag and thermal motion. Understanding the thermal motion and via the Stokes-Einstein equation, the drag on cylindrical particles becomes particularly interesting due to the role played by rod-like particles in biology. In this study we observe the thermal motion of gold nanorods and microtubules in Newtonian and complex fluids. Their translation and rotational diffusion coefficients were calculated from the mean square displacements of the particles. The experimental diffusion coefficients in 2M sucrose solution used as the standard Newtonian fluid were in good agreement with that of the theoretical values obtained by the Stokes Einstein equations and the hydrodynamic friction coefficients of thin cylinders (Tirado et al., 1979, 1980). By observing diffusion of rods in viscoelastic fluid like DNA solution, we were able to conclude that rods are less restricted in their normal and axial motion than rotational motion. This is due to the complex interaction between the length scales of the mesh network and the particle.

The thermal motion of spherical particles has been studied extensively and well documented over the years. In fact, micron sized spherical tracers are commonly used in microrheology (Mason and Weitz 1995; Mason et al., 1997; Schmidt, 1997) to probe the properties of both Newtonian and complex fluids. Though theories on diffusion and drag on rod like particles have existed for decades (Perrin 1936; Tirado and Garcia de la Torre, 1979, 80, 81) experimental observations have been few. Cush and Russo (Cush and Russo, 2002) observed the self diffusion of a concentrated solution of Tobacco mosaic virus to study how probe

interactions affect probe dynamics. Giardini and Theriot (Giardini and Theriot, 2001) have characterized the actin-based motility of the bacterial pathogen *Listeria monocytogenes* in normal mouse fibroblasts and in fibroblasts lacking intermediate filaments. The apparent diffusion coefficient of *L. monocytogenes* was two-fold greater in mutant fibroblasts than in wild-type fibroblasts, indicating that intermediate filaments significantly restrict the Brownian motion of bacteria. Dauty and Verkman observed a size dependant thermal mobility of rod like DNA in the cytoplasm during gene delivery. Upon disassembly of the actin cytoskeleton, this size dependant difference in mobility disappeared (Dauty and Verkman, 2005). An increased interest in biological motility has necessitated our studies on diffusion of cylindrical particles and their use as rheological probes. Moreover, these observations will provide novel techniques to probe the rheological properties of complex fluids like the cytoplasm from the stand point of particles closely resembling biological polymers. There is also an increasing interest in using cylindrical nano particles as drug delivery vehicles. Studying the motion of cylindrical particles fluids might elucidate the disadvantages and advantages of using nanorods in drug delivery applications.

The thermal motion of particles in a viscoelastic fluid is very different from their diffusive motion in a purely viscous fluid. The *mean square displacement* of tracer particles in a Newtonian fluid grows linearly in time, with a growth rate given by the diffusion constant. In a purely elastic medium, the tracer particles move due to thermal motion, but never actually diffuse through the sample. In fact, the amount of motion they can achieve is directly linked to the elasticity of the medium. Over time, the particle energy can be converted into stored elastic energy. The amplitude of the motion in a purely elastic medium approaches a constant value for large time. Thus, the elastic moduli of the material can be measured from the *msd*

for large time. Viscoelastic fluids display both of these behaviors. They contain colloidal structures which store and dissipate energy when deformed by a perturbative shear. Particles suspended in the fluid exhibit subdiffusive motion or may even be locally bound. In general the mean square displacement has nontrivial dependence on time, and this reflects the fact that the viscoelastic moduli are frequency dependent.

We used DNA solution as the viscoelastic standard. Rheological properties of DNA solutions have been studied quite thoroughly (Goodman et al. 2002, Chen et al. 2003). Using information about the contour length of individual DNA strands in a solution, concentration, and persistence length, the approximate mesh size can be calculated. Other advantages to using DNA solutions are the ability to regulate the length of the strands and change the interaction between strands by manipulating the base pairs at the ends. The effect of the viscoelastic properties of cytoplasm on the assembly and arrangement of cytoskeletal components like actin, microtubules and the motors associated with them is important to obtain a better understanding of cellular processes. Xenopus egg extract has been used for many studies pertaining to cell biology from actin tail polymerization (Theriot et al., 1994; Cameron et al., 1999; Taunton et al., 2000) to mitotic spindle assembly (Desai et al., 1999). The mechanical properties of Xenopus egg extract change with cell cycle, very possibly similar to those in vivo (Rankin and Kirschner, 1997). These extracts mimic the cellular cytoplasm and offer a unique environment in which to investigate the role of cytoplasmic mechanics without the complication of pre-organized cellular structures. Valentine et al. (Valentine et al., 2005) have characterized the rheology of crude interphase extracts using rheometer as well as multiple particle tracking of 1 micron beads. Here, we probe the rheology of cytoplasm with 1 micron beads as well as gold rods. The behavior of asymmetric

rod shaped particles in the extract could provide information of how microtubules possibly navigate the cytoplasm without the help of motors and microtubule associated proteins. These studies are also relevant to the movement of rod shaped pathogens like TMV and Listeria.

2. Theory

2.1 Diffusion coefficient for a spherical particle

The diffusion coefficient of a particle in a fluid equals

$$D = \frac{kT}{\gamma} \quad [1]$$

where, k is the Boltzmann constant and T is the temperature and γ is the drag coefficient of the particle in the fluid. The drag and diffusion coefficient of a spherical particle therefore equals

$$\gamma_s = 6\pi\eta a \quad [2]$$

$$D_s = \frac{kT}{6\pi\eta a} \quad [3]$$

where, η is the viscosity of the fluid and a is the radius of the sphere. The diffusion coefficient of a particle is related to the mean square displacement and time as shown below.

$$D_{n=1,2,3} = \frac{\langle x^2 \rangle}{2n\tau} [4]$$

Here, n, is the number of degrees of freedom for the particle. The diffusion coefficient of a spherical object in a plane ($n=2$) with radial mean square displacement (msd) of $<r^2>$ during a time interval τ equals

$$D_s = \frac{\langle r^2 \rangle}{4\tau} = \frac{kT}{6\pi\eta a} \quad [5]$$

Though the bead is free to move in the x, y and z directions, we cannot track the z motion and therefore $n = 2$.

2.2 *Diffusion coefficient for cylindrical particles*

For a cylindrical object (L/2r>1), the drag and diffusion coefficients parallel to its axis (axial), perpendicular to its axis (normal) and for angular rotation (rotational) is respectively given by (Tirado and Garcia de la Torre, 1979, 1980)

$$\gamma_{\parallel} = \frac{2\pi\eta L}{\ln(L/2r) - v_{\parallel}} \quad [6]$$

$$D_{\parallel} = \frac{kT\left(\ln(L/2r) - v_{\parallel}\right)}{2\pi\eta L} \quad [7]$$

$$\gamma_{\perp} = \frac{4\pi\eta L}{\ln(L/2r) + v_{\perp}} \quad [8]$$

$$D_{\perp} = \frac{kT\left(\ln(L/2r) + v_{\perp}\right)}{4\pi\eta L} \quad [9]$$

$$\gamma_{r} = \frac{\frac{1}{3}\pi\eta L^3}{\ln(L/2r) - v_{r}} \quad [10]$$

$$D_{r} = \frac{kT\left(\ln(L/2r) - v_{r}\right)}{\frac{1}{3}\pi\eta L^3} \quad [11]$$

Here, the out of plane movements of the rods cannot be tracked and hence $n = 1$ for all the above mobilities. The coefficients $v_{\parallel}$, $v_{\perp}$, v_{r} are the end effect corrections for cylindrical models derived from closed form solutions of ellipsoid and therefore are dependant on the aspect ratio of the rod (Table 4.1).

77

(L/2r)	$v_{\parallel}$	$v_{\perp}$	v_r
∞	-0.20	0.84	-0.66
50	-0.18	0.84	-0.61
5	-0.02	0.88	-0.48
2	+0.25	0.99	-0.21

Table 4.1. In the equation for drag coefficient of a cylinder as derived by Tirado and Garcia de la Torre, the constants for end correction for the cylinder $v_{\parallel}$, $v_{\perp}$, v_r, depend on the aspect ratio (L/2r) of the rod. The above table gives the values for end correction for rods of varying aspect ratio.

The mean square displacement of a cylinder parallel and perpendicular to its axis, and the mean square angular rotation relates to the diffusion coefficients via the following equations.

$$D_{\parallel} = \frac{\langle x_{\parallel}^2 \rangle}{2\tau} = \frac{kT\left(\ln(L/2r) - v_{\parallel}\right)}{2\pi\eta L} \quad [12]$$

$$D_{\perp} = \frac{\langle x_{\perp}^2 \rangle}{2\tau} = \frac{kT\left(\ln(L/2r) + v_{\perp}\right)}{4\pi\eta L} \quad [13]$$

$$D_r = \frac{\langle \theta_r^2 \rangle}{2\tau} = \frac{kT\left(\ln(L/2r) - v_r\right)}{\frac{1}{3}\pi\eta L^3} \quad [14]$$

The rotational diffusion coefficient is the mean square angular displacement in time in radian^2/sec. We multiply it with the square of the half length of the cylinder. This would represent the square of the arc traced out by the cylinder as it rotates and the units are m^2/sec. This allows us to compare the rotational diffusion with the axial and normal displacements.

From the equations [3], [7], [9], [11], we calculate that, in a Newtonian fluid a spherical particle of a given volume has a higher diffusion coefficient than a thin cylinder of the same volume. Similarly, a sphere of a given radius has a higher diffusion coefficient than a cylinder of the same radius (figure 4.1). This implies that spherical particles might be better drug carriers than cylindrical particles as they are more mobile than rods for the same amount of drug they carry. However, the results we present in this chapter shows that rods have higher axial and normal diffusivities in certain viscoelastic fluids where the characteristic length scale of the mesh is of the same order or higher than the length scales of the rod. The equation that relates the mean square displacement of a particle in a liquid to the viscosity of the liquid is termed the generalized Stokes-Einstein equation (GSE). Taking the logarithm of equation [4] gives $Log\langle r^2 \rangle = Log\tau + Log 4D_s$, an equation of a line of slope one and intercept Log ($4D_s$). Therefore, a plot of the Log(*msd*) over Log(τ) of a particle in a Newtonian fluid is a line of slope one with a particle diffusion coefficient given by the intercept of this line. The viscosity of the fluid can be calculated from the diffusion coefficient using the GSE equations. However, in viscoelastic fluids the energy of the particle is converted to stored elastic energy by the colloidal structures and dissipated when deformed by a perturbative shear. Particles exhibit frequency dependant subdiffusive motion, or, the plot of the Log(*msd*) over Log(τ) of the particle in a complex fluid has a changing slope with slope less than one at small time intervals and slope of one at long time intervals. The frequency dependant viscoelastic moduli of the fluid can be computed from the *msd* of by using the analytic fourier domain representation of GSE (Mason, 2000).
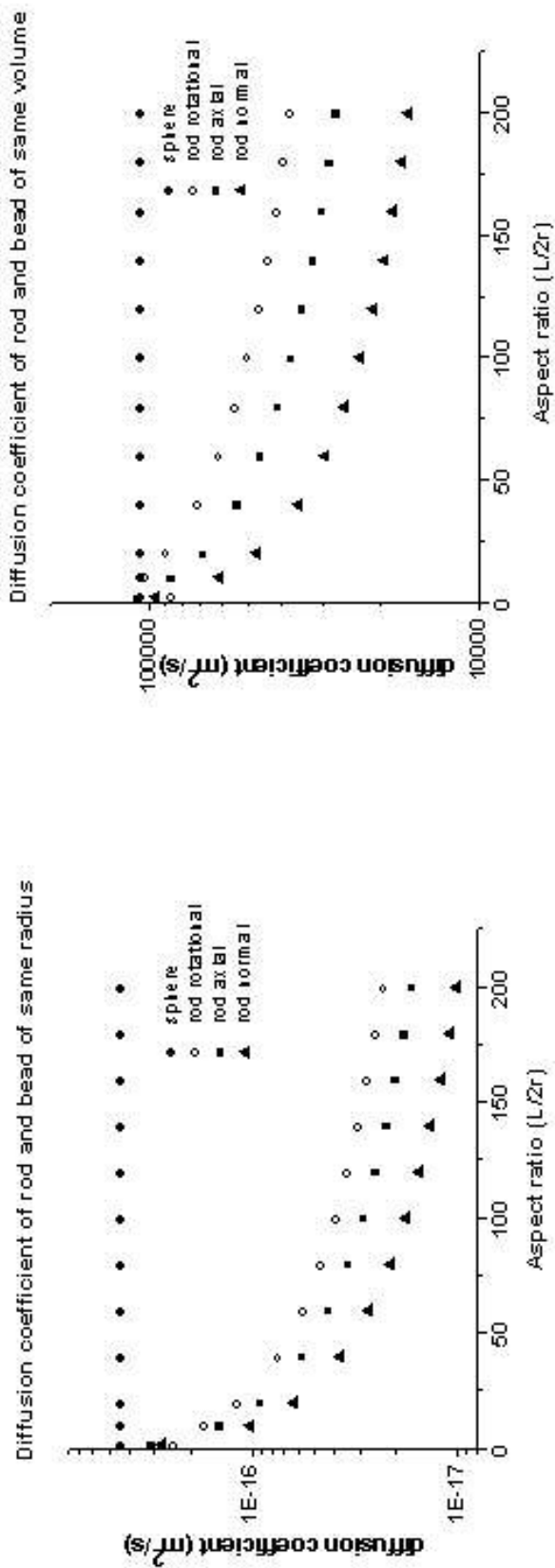
Figure 4.1. In the top figure, we compare the diffusion coefficients of a sphere and rod of the same radius and varying aspect ratio. Spherical particle has a higher diffusion coefficient than a rod of the same volume. In the bottom figure, we plot the diffusion coefficient of a sphere and rod of the same radius. The diffusion coefficient of a sphere is again higher than that of a rod.

However, the bulk apparent viscosity of the fluid can be calculated simply by considering the diffusive part (slope 1) of the plot of Log(msd) over Log(τ). The diffusion coefficient is calculated from the intercept of this line and the viscosity from the GSE equations. Equations [5], [12], [13], [14] can be multiplied by the relevant geometric factors and re-written to equal $\dfrac{kT}{\eta}$, a constant for a given fluid at a given temperature. In this chapter, we will address this quantity as the shape corrected mean square displacement.

$$D_s = \frac{3\pi a \langle r^2 \rangle}{2\tau} = \frac{kT}{\eta} \quad [15]$$

$$\frac{2\pi L \langle x_{\parallel}^2 \rangle}{2(\ln(L/2r) - v_{\parallel})\tau} = \frac{kT}{\eta} \quad [16]$$

$$\frac{4\pi L \langle x_{\perp}^2 \rangle}{2(\ln(L/2r) + v_{\perp})\tau} = \frac{kT}{\eta} \quad [17]$$

$$\frac{\pi L^3 \langle \theta_r^2 \rangle}{6\tau(\ln(L/2r) - v_r)} = \frac{kT}{\eta} \quad [18]$$

3. Materials and methods

Spherical particles 1 μm and 500 nm in diameter were purchased from Dynal Biotech (Invitrogen).

3.1 Gold nanorods

Gold nanorods 5 μm long, 200 nm in diameter were custom made in our lab (by Kwan Skinner) using the following technique. Commercially purchased AAO membranes with rated pore sizes of 200 nm are first sealed on one side via the thermal evaporation of a thin film of silver. This serves as the base for the subsequent deposition of the nanowires and as an active working electrode in the electrochemical cell. The AAO membrane is then

mounted into a homemade cell attached to a commercially purchased potentiostat (Radiometer Analytical PST050) as the working electrode with platinum and Ag/AgCl (Sat. KCl) as the counter and reference electrodes, respectively. The cell is filled with a silver plating solution (Technic Silver 1025) and a sacrificial layer of silver is deposited into the AAO to fill the branched portion of the membrane by setting the current density of the system to ~1 mA/cm^2 for half an hour. The silver plating solution is removed and the cell is rinsed 3 times with distilled water. The cell is then filled with a gold plating solution (Technic Gold 24) and Au segments are deposited by setting the current density to ~ 0.55 mA/cm^2 for 1 hr. At completion the gold plating solution is removed and the cell is rinsed twice with distilled water. The membrane is taken out of the cell, and the evaporated thin film of silver and the sacrificial layer are both removed by immersing the cell into concentrated nitric for approximately 15 seconds. The membrane is then rinsed with distilled water, and the process is repeated once more before submerging in 3M NaOH for 30 minutes to completely dissolve the AAO membrane leaving the Au nanowires free in solution. The solution with the wires is then washed with ethanol 3 times by centrifugation for 4 minutes at 4000 rpm. Finally, 0.01 v/v% sodium dodecyl sulfate (SDS) is added to the nanowires and sonicated for approximately 1 hour to aid in nanowire monodispersity for subsequent experiments. The rods were then imaged in a scanning electron microscope. The average length of the rods were 4.5 ± 0.2 μm and the average diameter 230 ± 20 nm. The gold rods were functionalized with an alkane thiol to prevent possible chemical interaction with the DNA network and proteins in the extract. The rods were incubated in fluorescently labeled DNA solution and 2 mg/ml rhodamine-BSA solution for 1 hr at room temperature. Upon

inspection under a fluorescence microscope, the rods did not show any signs of adhered DNA or BSA.

3.2 Microtubules

Tubulin and rhodamine tubulin were obtained from cytoskeleton Inc. Microtubules were polymerized by incubating tubulin in BRB80 buffer (80 mM K-Pipes/1mM MgCl2/1mM EGTA, 50%Sucrose in pH 6.8) in a 37C bath for 20 minutes. EDC was diluted to 4 mM into the MT solution and incubated for another 30 minutes. Sodium phosphate was added to 0.1M (pH 6.8) and incubated further for another 60 minutes. The length of the microtubules ranged widely from 5 microns to 12 microns.

3.3 Sucrose: Newtonian Standard solution

2M sucrose solution was prepared by quantitatively adding 34.23 g of sucrose (dried at 80ºC for 12-16 hours) to a 50 mL volumetric flask. Approximately 25 mL of distilled water was added to the flask and the resulting solution was heated to ~80 – 90 ºC. The solution was occasionally agitated to encourage dissolution. Small amounts of water were added until the sucrose was fully dissolved. Sodium azide was added to the solution (final concentration, 0.05%) in order to discourage microbial growth. The solution was diluted to volume at room temperature. A published model exists for predicting the viscosity of a sucrose solution as a function of the sucrose concentration and the solution's temperature (M.Mathlouthi and J.Génotelle, 1995). The model is a fourth-order polynomial fit and predicts viscosity values to within 1%, provided that solubility and temperature constraints are met. The expected viscosity for a 2M sucrose solution at 22.9 ºC is 23.5 mPa s. The percent error for the test solution is 17.4% from the expected value. This error could have been introduced during the preparation of the sucrose solution, or may be attributed to

evaporative losses around the sample-air interface on the rheometer during testing. Evaporation would contribute to a higher concentration of the test solution and thus a higher viscosity.

3.4 DNA solution: Viscoelastic standard

λ-DNA was purchased from Invitrogen (cat# 25250-010) and concentrated to a maximum concentration of 1.44 mg/mL by alcoholic precipitation. λ-DNA derived from the λ-bacteriophage, is 48512 base pairs in length and has a molecular weight of 32 M Da. Dilutions of λ-DNA solutions were made using a storage buffer solution containing 10 mM Tris-HCl (ph 7.4), 5 mM NaCl, 0.1mM EDTA, and 0.05% Sodium Azide. The viscosity of the buffer solution was assumed to be equivalent to that of water. Stock λ-DNA solutions were stored at 4ºC and allowed to equilibrate at least overnight before rheological experiments. The approximate mesh size of this DNA solution was calculated to be 150 nm.

3.5 Xenopus egg extract: CSF extract

Cytostatic Factor (CSF) extract was prepared from xenopus frog eggs using the protocol by Murray (Murray, 1991). 3 to 12 days before preparation, the adult female Xenopus were injected with 100 Units Pregnant Mare Serum Gonadotropin. 16 hrs before eggs are needed, frogs were injected with 500 Units Human Chorionic Gonadotropin. Frogs were placed in separate 4 liter containers with 2 liter of 1X MMR (100 mM NaCl, 2 mM CaCl$_2$, 2 mM KCl , 1 mM MgCl$_2$, 5 mM HEPES, pH 7.8, 0.1 mM EDTA) at 16°C, out of direct light, until egg collection and extract preparation. The frogs are then removed to containers containing water and the eggs are checked for quality. Stringy, white and puffy eggs were removed to ensure the quality of the extract. The good eggs were collected in a 400 ml beaker. The eggs were washed in fresh MMR till all the debris was removed. The

outer jelly coating of the eggs was then removed by letting the eggs sit in a dejellying buffer (1X XB salts, 40 mM NaOH, 2% (w/v) Cysteine) for 5 mins. As soon as the eggs packed down to one-third of their original volume, the dejellying solution was poured off and the eggs were quickly washed 3 or 4 times with XB solution (100 mM KCl , 0.1 mM $CaCl_2$, 10 mM HEPES, pH 7.7, 50 mM Sucrose, 1 mM $MgCl_2$). Puffy and lysed eggs were remove during all the washes. The eggs were then washed 3 times in CSF-XB (100 mM KCl , 0.1 mM $CaCl_2$, 10 mM HEPES, pH 7.7, 50 mM Sucrose, 5 mM EGTA , 2 mM $MgCl_2$) and 3 times in CSF-XB-LPC(50 ml CSF-XB, 50ul of 10mg/ml Leupeptin, Pepstatin and Chymostatin). Using a cut-off Pasteur pipette, the eggs were transfered into 1 ml of CSF-XB-LPC containing 100 μg/ml cytochalasin D in 13 x 51 ultraclear tubes. The eggs were then packed down in the tubes by centrifuging in a clinical centrifuge for 1 min at 200 g and then increasing the centrifugation to 800 g for 30 sec. Excess buffer was removed and the eggs were centrifuged in the ultracentrifuge at 16,000 g (8300rpm in an SW41 rotor) for 15 min at 16°C. The tubes with crushed eggs were placed on ice. Prior to collecting the cytoplasmic layer, the sides of the tubes were wiped with 95% ethanol. The cytoplasmic layer, the muddy or straw colored layer in the middle of the tube was collected by puncturing the tube near the bottom of the layer with an 18 gauge needle (on a 1 cc syringe), and the extract gently drawn out. The collected extract was transferred to a 5 ml snap cap tube and its volume estimated. 1/1000 volume of protease inhibitor (LPC) and cytochalasin stocks (10mg/ml), and 1/20 volume of 20X Energy Mix (150 mM creatine phosphate, 20 mM ATP, 20 mM MgCl2) was added to the extract.100 μl aliquots of the extract were flash frozen in liquid nitrogen and stored in the -80 freezer.

The frozen aliquot of extract was thawed right before experiments and 10 μm Nocodazole was added to prevent microtubule polymerization. The cytochalasin already added to the frozen extract prevents actin polymerization.

3.6 Macroscopic rheology measurements

The viscometry mode of the Bohlin rheometer software tests for a material's response to varying stresses or shear rates. Approximately 1.5mL of 2M sucrose was placed on the lower plate of the rheometer and the upper cone was lowered to a gap of 30 microns. Inspection of the external edges of the sample insured no under- or over-filling of the sample chamber. The cone (60mm diameter, 1° cone angle) rotated unidirectionally until a steady state value was achieved. For a controlled-stress experiment, the viscosity was calculated by dividing the average obtained shear rate by the input stress [bohlin manual].

Newtonian fluids, such as the 2M sucrose solution used here, exhibit independence of their viscosities to varying input stress/shear rates. Shear stresses ranging across four orders of magnitude, from 0.01 Pa to 10 Pa, were applied to the standard 2M sucrose solution and resulted in a population of 8 viscosities ranging from 27.0 − 28.1 mPa s. A single-factor analysis of variance shows statistically that varying the input shear rate does not influence sucrose's viscosity ($p = 0.58$, where $p < 0.05$ denotes statistical significance). From the above value, a mean viscosity of 27.6 mPa s with a standard error of 0.13 mPa s is obtained. Bulk viscoelastic measurements of the DNA solution were performed using the Bohlin rheometer as explained above. These experiments gave a value of 0.2 Pa s for the bulk apparent zero shear viscosity of the DNA solution. Similar viscoelastic measurements performed on Xenopus egg extracts gave a value of 0.02 Pa s for the bulk apparent zero shear viscosity.

4. Data acquisition and analysis

Trace amounts of carboxy modified beads and alkane thiol modified gold nano rods were added to the different solutions. 2 µl drop of each of the sample was loaded between 2 coverslips with a spacing of 150 µm. The sample was then placed gently on a Nikon inverted microscope with a 60X objective and observed under bright field. Movies of particles diffusing at the center of the sample space (to avoid edge effects) were captured using a Pulnix camera at frame rates of 120 fps. Fluorescent microtubules were observed under a Nikon spinning disc confocal microscope using a 60X water immersion objective. Images were taken with a Cool snap (roper sci.) camera at 1 fps. The particles were tracked using the video spot tracker program written by the CS department at UNC-CH (www.cs.unc.edu/Research/nano/cismm/ download/spottracker/video_spot_tracker.html). For the beads, the tracker program outputs the x and y position coordinates in the plane of focus over time. If x_1, y_1 and x_2, y_2 are the positions of the bead at times $t = t_1$ and $t = t_2$ respectively, the radial mean square displacement of the bead during time $\tau = t_2 - t_1$ is given by

$$\langle r^2 \rangle = (x_2 - x_1)^2 + (y_2 - y_1)^2 \quad [14]$$

For the cylindrical objects, the tracker program outputs the x and y position coordinates and the orientation angle of the rod. If x_1, y_1, θ_1 and x_2, y_2, θ_2 are the positions and orientations of the rod at time $t = t_1$ and $t = t_2$ respectively (figure 4.2), then the mean square displacements and angular rotation of the rod during $\tau = t_2 - t_1$ is given by

$$\langle x_\parallel^2 \rangle = (s \sin \phi)^2$$
$$\langle x_\perp^2 \rangle = (s \cos \phi)^2 \quad [15]$$
$$\langle \theta_r^2 \rangle = (\theta_2 - \theta_1)^2$$

where,

$$s = \sqrt{(x_2 - x_1)^2 + (y_2 - y_1)^2}$$
$$\phi = 90 - \theta_1 - \alpha \qquad [16]$$
$$\alpha = \tan^{-1} \frac{(y_2 - y_1)}{(x_2 - x_1)}$$

The tracking program is capable of finding the centroid of diffusing 1 micron beads with ~ 20 nm accuracy and that of fixed 5 micron long, 200 nm diameter rods with ~40 nm accuracy. However, the noise in the tracking increases when the rods diffuse out of focus (accuracy not estimated). The mean square displacements over time for the rods and beads were calculated from the output of the spot tracker program using custom written Matlab codes.

5. Results and discussion

5.2 Multiple particle tracking

5.2.1 2M Sucrose

The mean square displacement (*msd*) in time for the multiple beads and rods were obtained as described in the methods section. The Log of *msd* averaged over multiple particles, with the standard deviation as error bars was plotted against Log(τ) (figure 4.2). The plot of Log(*msd*) against Log(τ) for beads generated a line of slope 0.96. A similar plot for the axial, normal and rotational *msd*'s for rods generated lines of slope 0.94, 0.93 and 0.97 respectively (figure 4.3). The slopes close to one indicate that both the beads and rods are purely diffusive in the Newtonian sucrose solution. The mean square displacements of both beads and rods were multiplied by the relevant shape factor (eqns. [15]-[18]). The shape corrected *msd*'s were plotted in figure 4.4. The displacement curves of rods and beads overlay each other within errors. This is expected as the shape corrected displacement is an indicative of the fluid property and in this case that of the viscosity of sucrose.
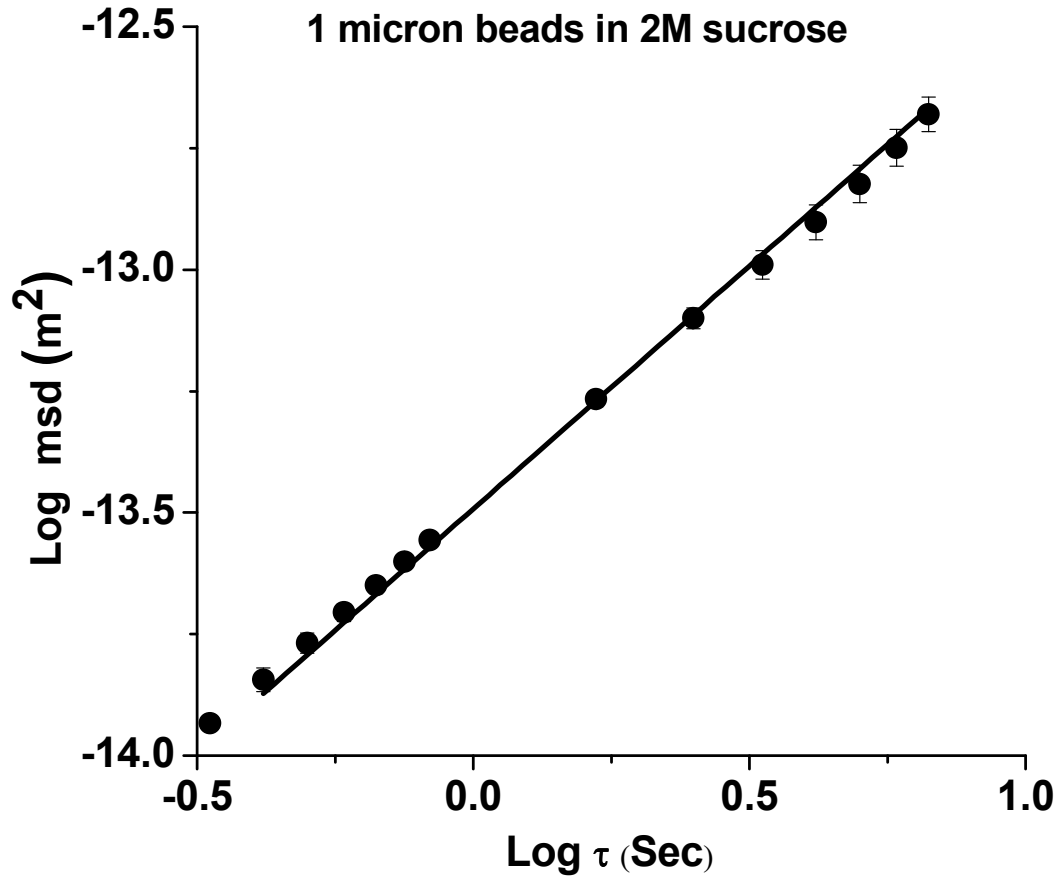
Figure 4.2. The Log of *msd* averaged over multiple 1 micron spheres, with the standard deviation as error bars is plotted against Log(τ). This plot is a line of slope 0.96. The slope close to one indicates that the beads are purely diffusive in the Newtonian sucrose solution.

Gold rods (L=5µm,r = 200nm) in 2M sucrose
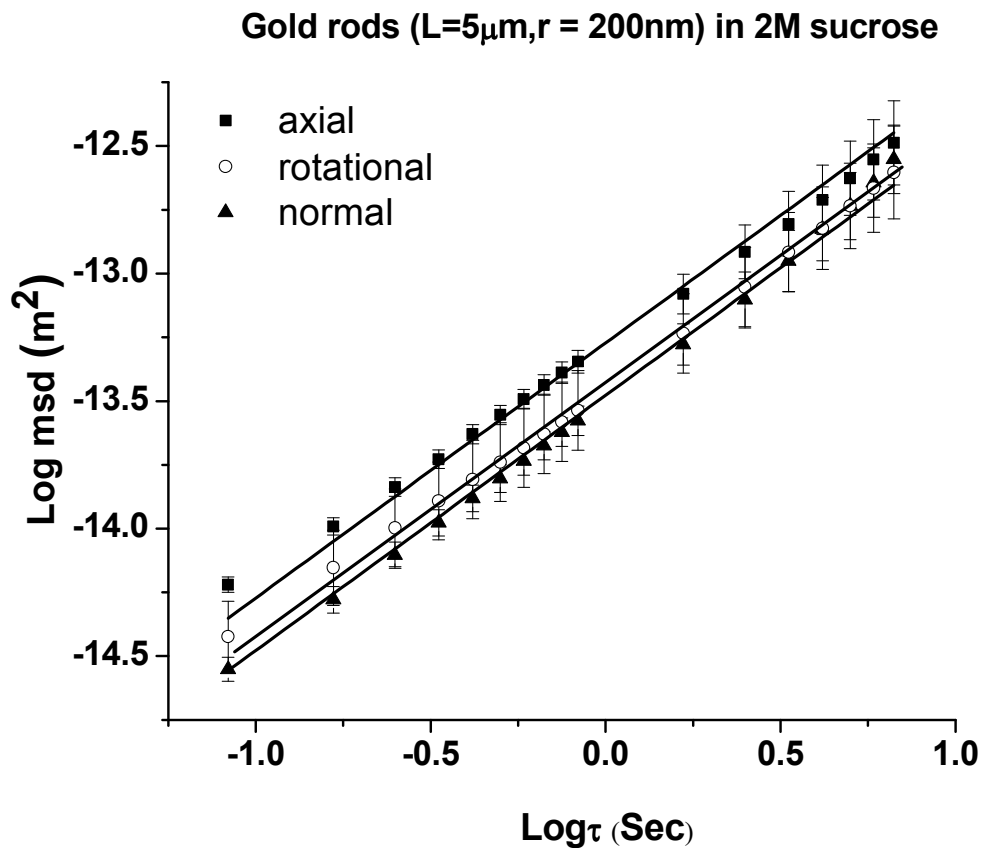
Figure 4.3. The Log of *msd* averaged over multiple rods, with the standard deviation as error bars was plotted against Log(τ). The plot of Log(*msd)* against Log(τ) for the axial, normal and rotational *msd*'s for rods generated lines of slope 0.94, 0.93 and 0.97 respectively. The slopes close to one indicate that the rods are purely diffusive in the Newtonian sucrose solution.

Figure 4.4. The mean square displacements of both beads and rods were multiplied by the relevant shape factor and their shape corrected *msd*'s are plotted in the above figure. The displacement curves of rods and beads collapse to form one master curve within errors. This is expected as the shape corrected displacement is an indicative of the fluid property and in this case that of the viscosity of sucrose.
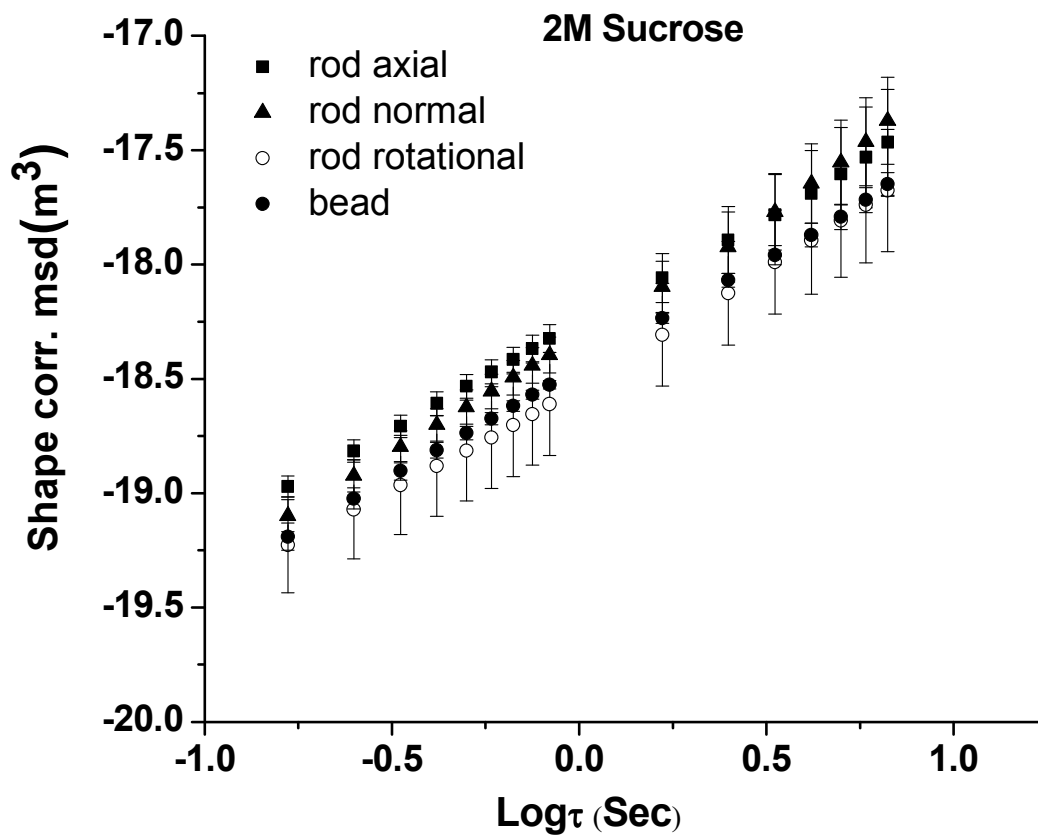
The diffusion coefficients of beads and rods were obtained from the intercept of the *msd* plots. Using the generalized Stokes-Einstein equation, we obtained the viscosity of the solution as measured by the beads and rods (table 4.2). The viscosity of the sucrose solution as measured by 1micron bead was 22.37 mPa s and the axial, normal and rotational diffusion of the rod was 20.0 mPa s, 19.2 mPa s and 23.61 mPa s respectively. These values are in agreement with the viscosity (23.06 mPa s) of 2M sucrose at room temperature. This is the first example of using rod like particles as probes in microrheology. These viscosity measurements of sucrose solution act as a control by characterizing the maximum deviation in viscosity values as measured by beads and rods. The good agreement in viscosity values also validates the drag equation for rods as derived by Tirado and Garcia de la Torre.

|	1 micron bead	Gold rods (L = 5µm, 2r = 200 nm)		
		Axial	Normal	Rotational
Diffusion coefficient (m^2/s)	1.95 ± 0.03E-14	2.12 ± 0.07E-14	1.67 ± 0.03E-14	2.30 ± 0.15E-14
Viscosity (Pa s)	0.022	0.020	0.019	0.023

Table 4.2. The diffusion coefficients of beads and rods were obtained from the intercept of the *msd* plots. Using the generalized Stokes-Einstein equation, we obtained the viscosity of the solution as measured by the beads and rods. These values are in agreement with the viscosity (23.06 mPa s) of 2M sucrose at room temperature.

5.2.2 DNA solution

Thermal motion of 500nm and 1 micron beads was observed in the DNA solution and their *msd*'s over time is plotted in figure 4.5.

Beads in 1.4mg/ml DNA soln
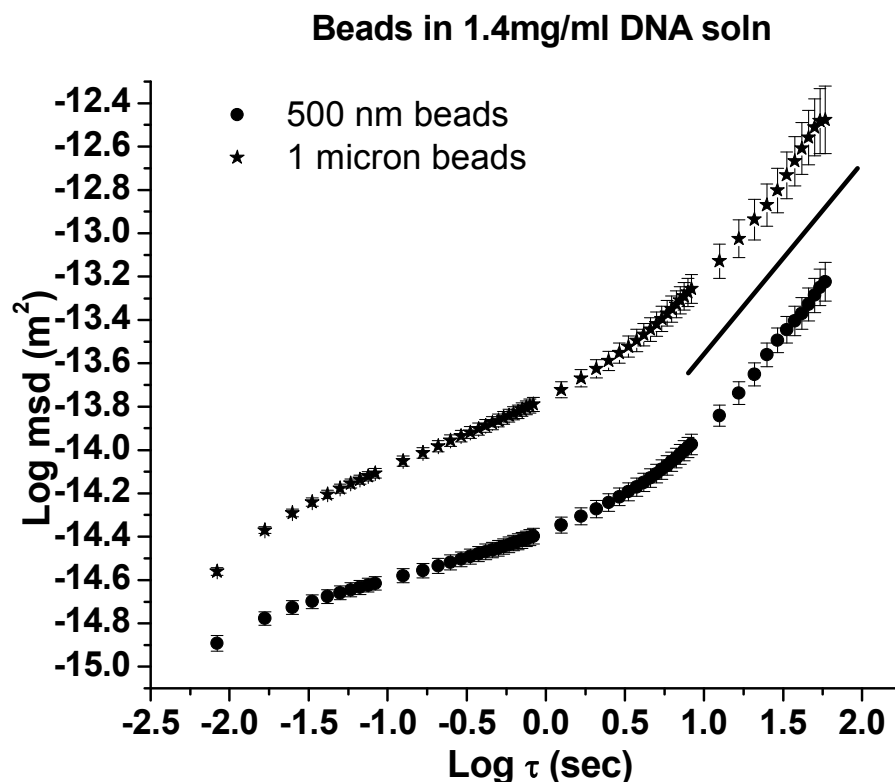
Figure 4.5. The *msd* over time of 500nm and 1 micron beads is plotted in figure. In the DNA solution, the particle movements were sub diffusive at short observation times followed by a cross over to diffusive behavior at long times. Solid line indicates slope 1.

In the non-Newtonian DNA solution, the particle movements were sub diffusive at short observation times followed by a cross over to diffusive behavior at long times. The displacements over time of the 1micron, 500nm diameter beads were shape corrected and plotted in the figure 4.7. In the viscoelastic DNA solution, their shape corrected *msd*'s did not overlay indicating that the different beads probe different fluid behavior of the same DNA solution. This is due to a size dependant interaction between the probes and the fluid. The GSE is based upon the assumption that the complex fluid can be treated as a continuum

around the probe or equivalently, the length scales of the colloidal structures giving rise to the elasticity (mesh size) are smaller than the size of the particle. From preliminary calculations, we obtain a mesh size for the DNA solution to be ~150 nm. From Schnurr et al.'s calculations, it is reasonable to consider a ratio of probe size to matrix structural size of at least 20 times as sufficient for continuum viscoelasticity to be valid (Schnurr et al., 1997). This is not the case for the beads. The diffusion coefficients of beads were obtained from the intercept of the diffusive part (slope 1) of the *msd* plots. The bulk apparent viscosity of the solution as measured by the different probes was calculated from the diffusion coefficients (table 4.3). The viscosity values measured by 500nm beads and 1 micron beads were 0.57 Pa s and 1.53 Pa s respectively. We attribute this variation in measurements to the size of the probe and a failure in assumption of viscoelastic continuum. The 500 nm bead, due to its smaller size is capable of navigating through the polymer mesh more easily than a bigger 1 μm bead. As a result, the 500nm beads measure a lower value of bulk apparent viscosity. However, both these values are higher than the bulk apparent zero shear viscosity of 0.2 Pa s measured using the rheometer for the DNA solution. We speculate that this could be due to a chemical interaction between the carboxy modified beads and the DNA network. DNA molecules adhering to the beads increase their diameter rendering them less diffusive. Beads could also be adhering to the entangled DNA mesh, becoming locally bound. Chae and Furst performed microrheology experiments in f-actin solution with both polystyrene (PS) and BSA coated polystyrene (PS-BSA) microspheres of sizes ranging from 0.1-1.0 microns. They observed that their PS particles showed a size dependant scaling in their rheology measurements but their PS-BSA did not. Further, the diffusion coefficients of the PS-BSA beads were much higher than that of PS beads of equal size. They further hypothesize that

this is consistent with the formation of a polymer-depleted shell surrounding the probes by exclusion or orientation of actin filaments near probes due to their long length and rigidity. Probe surface chemistry can not only bring about a size dependency in rheology measurements, it can also provide unexpected results for measured viscoelastic moduli due to chemical interaction between probe and fluid. Further experiments using PEG modified beads have to be performed to verify if this is the case for the above results.

The *msd*'s of gold nano rods in DNA solution were plotted in figure 4.6.
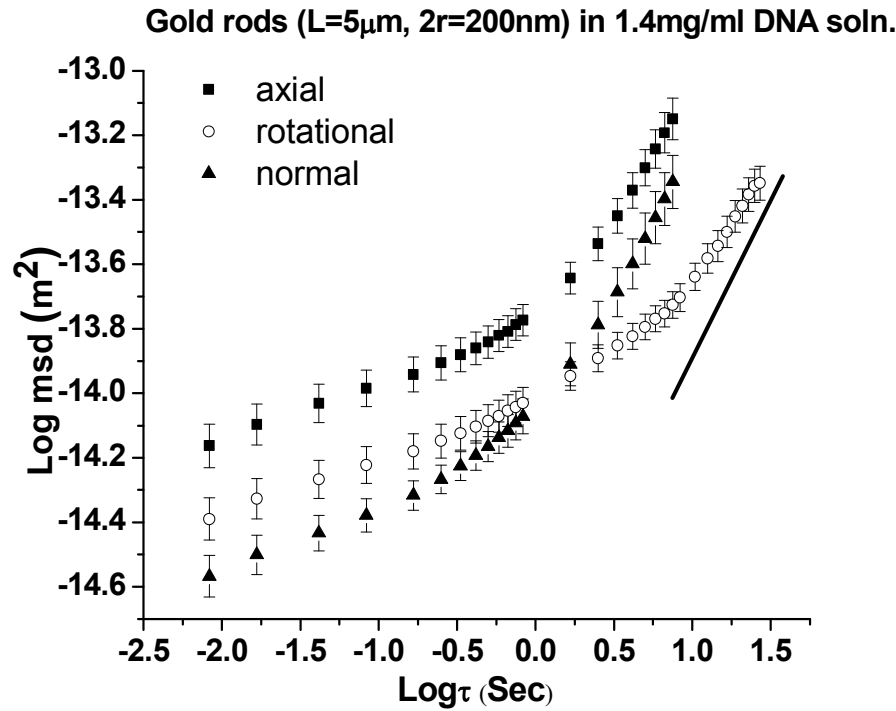
Figure 4.6. The *msd* over time of gold rods is plotted in this figure. In the DNA solution, the particle movements were sub diffusive at short observation times followed by a crossover to diffusive behavior at long times. Solid line indicates slope 1.

The shape corrected *msd*'s of axial normal and rotational motion of rods plotted in figure 4.7 did not overlay with each other or with that of the beads displaying a probe size effect in the thermal motion of the rods in the DNA solution.
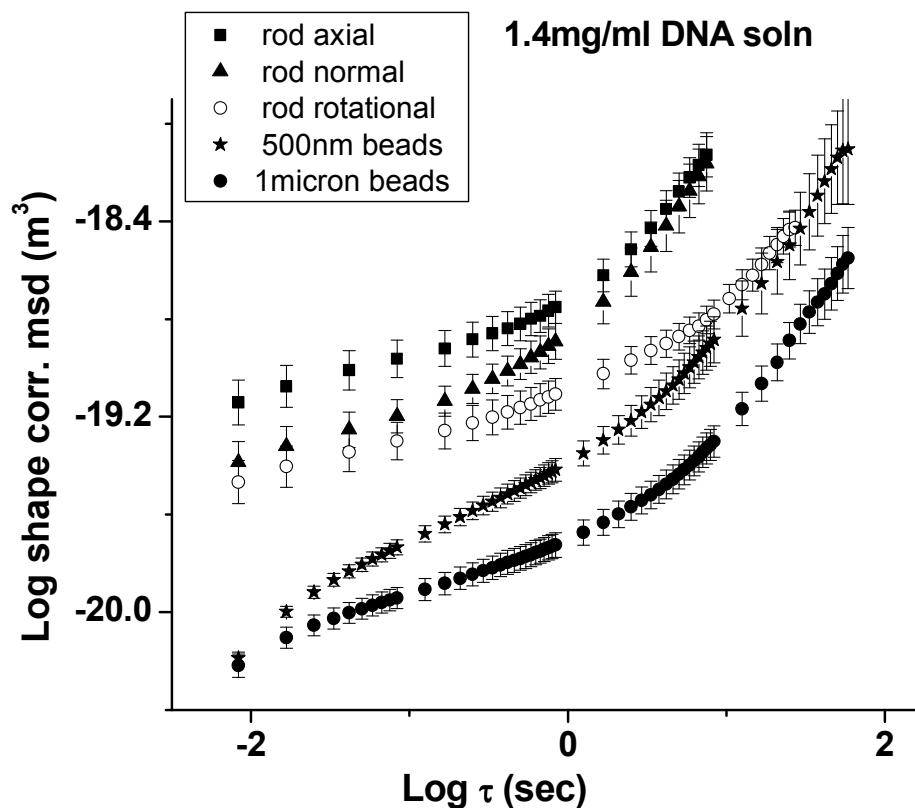
Figure 4.7. *msd*'s of beads as well as rods in 1.4mg/ml DNA solution were multiplied by their respective geometric factor. The shape corrected *msd* curves did not collapse to one curve indicating a probe effect in the microrhelogy measurements.

The axial and normal motion of rods measured viscosity values of 0.074 Pa s and 0.086 Pa s, much lower than the bead and rheometry measurements. We interpret this to mean that the 200nm diameter rods navigate the 150nm DNA mesh probing the buffer more often than the DNA network. However, the rotational diffusion of rod measured a higher viscosity value of

0.26 Pa s. During rotational diffusion the rod encounters the mesh more often than it does axially and normally and therefore measured a higher viscosity value.

	500nm bead	1 μm bead	Gold rods (L = 5μm, 2r = 200 nm).		
			Axial	Normal	Rotational
Diffusion coefficient (m²/s)	1.51E-15	2.84E-16	5.28E-15	3.13E-15	1.84E-15
Viscosity (Pa s)	0.57	1.53	0.07	0.09	0.27
$\dfrac{microvis\cos ity}{macrovis\cos ity}$	2.88	7.68	0.37	0.43	1.35

Table 4.3. The diffusion coefficient of rods and beads in 1.4mg/ml DNA solution. The apparent viscosity of the solution as measured by the particles are compared. The ratio of viscosity measured by different probes to the macroscopic viscosity shows that carboxy modified beads measure a higher than expected viscosity for the DNA solution. The axial and normal motion of rods measured viscosity values lower than rheometry measurements. The 200nm diameter rods navigate the 150nm DNA mesh probing the buffer more often than the DNA network. The rotational diffusion of rod measured a higher viscosity value. During rotational diffusion the rod encounters the mesh more often than it does axially and normally and therefore measured a higher viscosity value.

5.2.3 CSF extract

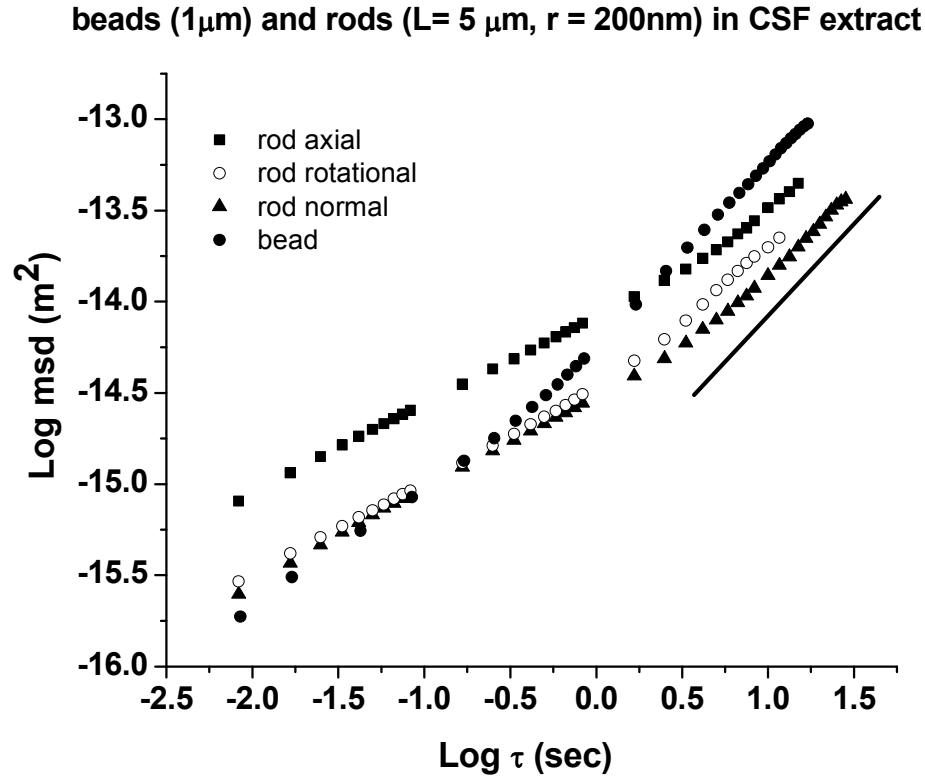The motion of 1micron beads were tracked in the extract and the *msd* over time was plotted in figure 4.8. The *msd* plot of the bead was a line of slope 0.86 at short τ, changing to a slope1 at long τ, indicating that the extract is predominantly viscous.

beads (1μm) and rods (L= 5 μm, r = 200nm) in CSF extract

Figure 4.8. The *msd* over time of 1 micron bead and gold rod is plotted above. The *msd* plot

of the bead was a line of slope 0.86 at short τ, changing to a slope 1 at long τ, indicating that

the extract is predominantly viscous. The axial, normal and rotational *msd*'s of the rods were

curves of slope 0.48, 0.60 and 0.57 at shorter τ (sub diffusive) and slope of 1 at long τ

(diffusive). The solid line indicates slope of 1.

The apparent viscosity as measured by 1um beads was 0.30 Pa s. This value is almost an

order of magnitude higher than 0.02 Pa s measured using the rheometer. The higher viscosity

value could arise from chemical interactions between carboxy beads and the proteins in the

extract. The axial, normal and rotational *msd*'s of the rods plotted in figure 4.8 were curves

of slope 0.48, 0.60 and 0.57 at shorter τ (sub diffusive) and slope of 1 at long τ (diffusive).

The measured viscosities were, 0.12 Pa s, 0.19 Pa s and 0.21 Pa s respectively. These values are also an order of magnitude higher than the viscosity of 0.02 Pa s measured using the rheometer. We conclude that chemical interactions between the probe and the proteins in the extract is not likely the reason as our preliminary studies show that BSA does not adhere to the alkane thiol modified gold rods. This deviation could be due to the shape and size of the rod leading to a physical interaction between the probe and the mesh network. Valentine et al. (Valentine at al., 2005) have performed rheology measurements on crude interphase xenopus egg extract measuring a viscosity value in the range 10-30 mPa s. They saw no correlated particle movements indicating that the filaments that are responsible for the macroscopic elastic response are well separated, with a mesh size larger than particle diameter of 1 um. However, they observed some subdiffusive particle dynamics, suggesting that local microstructure may provide some resistance to tracer movement. The extract was treated with cytochalasin-D as well as Nocodazole to inhibit actin and microtubule polymerization. Intermediate filaments may be present in the extract forming the micron scale network. Since the length of our rod is 5 microns, there is a high probability that the motion of our rods is restricted by these microstructures leading to the higher apparent viscosity measurements.
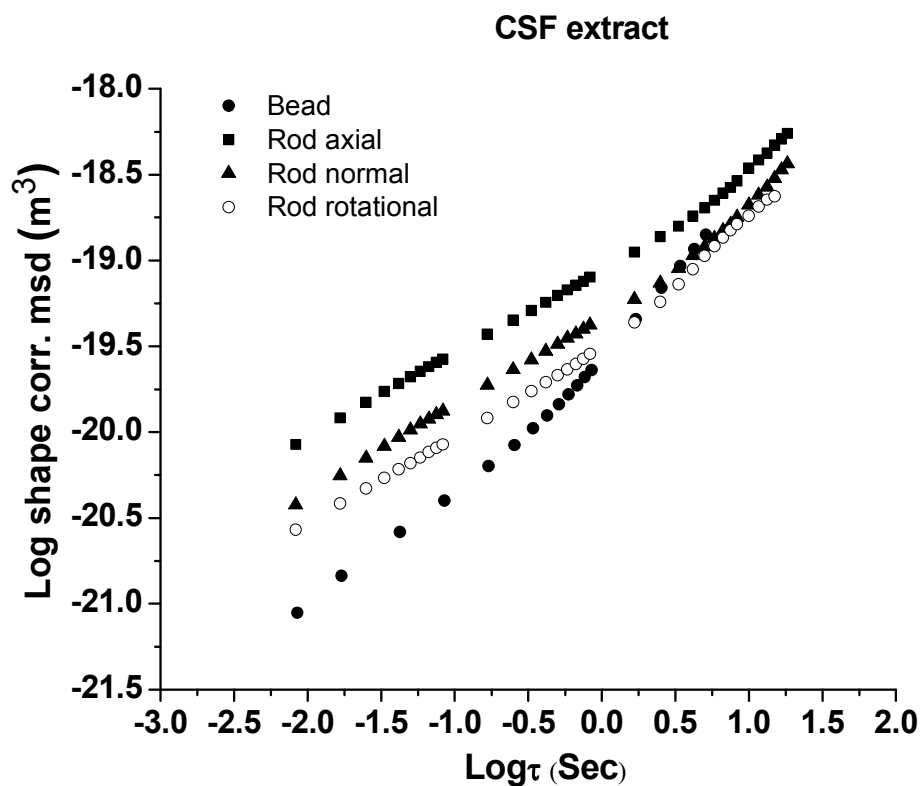
CSF extract

Figure 4.9. *msd*'s of beads as well as rods in CSF extract were multiplied by their respective geometric factor. The curves for bead, normal rod motion and rotational rod motion collapsed, but, the axial motion of rod did not. This indicates a probe effect in the microrhelogy experiments.

|	1 μm bead	Gold rods (L = 5μm, 2r = 200nm)		
		Axial	Normal	Rotational
Diffusion coefficient (m²/s)	1.44 E-15	3.14E-15	1.37E-15	2.26E-15
Viscosity (Pa s)	0.30	0.12	0.19	0.22
$\dfrac{microvis\cos ity}{macrovis\cos ity}$	15.2	6.2	9.9	10.9

Table 4.4. The diffusion coefficient of rods and beads in CSF extract. The apparent viscosity of the solution as measured by the particles are compared in the above table. These values are an order of magnitude higher than the macroscopic viscosity. This is probably due to the rod motion being restricted by microstructures in the extract leading to the higher apparent viscosity measurements.

5.2.4 Microtubule diffusion in 2M sucrose

To take our study a step further, we wished to observe the motion of microtubules in viscous and viscoelastic fluids, especially the cytoplasm. This poses many challenges. Exposures of 300ms-500ms are required to obtain high contrast images of MT's which can be tracked using the spot tracker software. This reduces our temporal resolution to 1-2fps. Movies could be taken only for 70-100s due to photobleaching of the fluorescent MT's. Further, the heating of the sample by the laser also introduces large drift in our samples. We observed MT diffusion in Sucrose solution as a control to figure out the feasibility of these experiments. The axial, normal and rotational *msd*'s of microtubules were plotted over time. Line fits to the *msd*'s had slopes of 0.86, 0.90 and 0.69 for axial, normal and rotational motion (figure 4.10). The diffusion coefficients of microtubule and measured viscosity of sucrose solution was obtained from the *msd*'s. The axial, normal and rotational diffusion of MT's measured values of 73.29 mPa s, 49.90 mPa s and 90.00 mPa s for the viscosity of sucrose. These values are much higher than 23 mPa s, the viscosity of 2M sucrose at RT. To ensure that addition of MT's did not alter the properties of sucrose solution, we tracked 1micron beads in the same sample. The viscosity value measured by beads was 24.5 mPa s consistent with pure sucrose solution, indicating that addition of MT's did not alter the solution properties. One reason could be error in estimating the length of the diffusing MT's

which are tilted out of the plane of focus. These microtubules would appear shorter than their actual length. The derived viscosity is inversely proportional to the length of the rod in the GSE. Using a smaller value for the length of the rod would give a higher viscosity value. The other reason could be the inability of the spot tracker to detect the movement of the centroid of the fluorescent MT. These difficulties will have to be addressed before using MT's as probes for rheology studies.
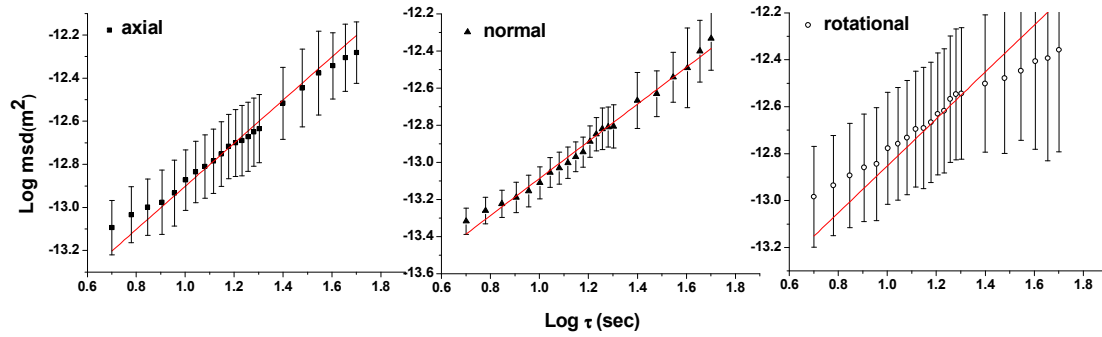
Figure 4.10. The axial, normal and rotational *msd*'s of microtubules plotted over time. Line fits to the *msd*'s had slopes of 0.86, 0.90 and 0.69 for axial, normal and rotational motion.

6. Conclusion

A new microrheological approach of using rod shaped particles as probes was presented in this chapter. The good agreement between our measurements of viscosity of 2M sucrose and expected values validates this approach. The deviation from expected values in complex solution necessitates further studies. Due to the asymmetry of rod shaped particles, there are 2 scales of length dependant interaction with the mesh network of complex fluids. In purely viscous fluids, the length of the rod contributes explicitly to the drag on the rod.

The drag force acting on a rod is higher than that on a sphere of the same volume. However, in DNA solution, the rod experiences a drag lesser than that experienced by a sphere of the same volume. On the other hand, rods experience high resistance to mobility in extracts probably due to the interaction between the network and rod length. In the previous chapter (**Chapter III**) we used flow to align motile actin filaments and noted that velocities greater than 50 μm/s producing torques greater than 100 pNnm on a micron long filament is required for filament alignment. Although physiological velocities are much lower, we expected the high viscosity of the cytoplasm to compensate and produce higher drag forces that bring about the same phenomena of filament orientation. Based on our observations in this chapter, we cannot assume that currently available measurements of cytoplasmic viscosity will apply to actin or microtubules. Rheological measurements of cytoplasm using rods of dimensions similar to actin and microtubules have to be performed. More over the surface chemistry of the particle also affects thermal motion. To include these effects, stabilized microtubules and actin filaments have to be used as rheological probes. The current study is very relevant to biology and medicine especially in the context of cytoskeletal organization in the cell, rod shaped macromolecular drug delivery and mobility of rod shaped pathogens in the complex cytoplasm and nucleus. Some specific examples are discussed below. The mechanical properties of xenopus egg extract change with cell cycle, very possibly, similar to the changes in vivo (Rankin and Kirschner, 1997). Performing the above experiments in extract arrested at different cell cycle stages would elucidate how these mechanical properties change with cell cycle. Gene delivery by synthetic vectors after uptake into the cytosol takes advantage of diffusion to reach the nucleus. Cytoskeletal structures hinder this process and the extent of restriction can be expected to be dependant on the length of the gene. Successful

delivery requires thorough characterization of the length scales to come up with the optimum length DNA sequence. Listeria monocytogenes, the rod shaped pathogenic bacteria moves rapidly thorough the host cell by polymerizing an actin comet tail using protein Act-A (Theriot et al., 1992). Beads coated with Act-A are typically used to study the mechanism and force generation of Listeria motility. Considering that the length scale of the mesh network in the cytoplasm is of the order of microns, and that Listeria is typically 2 μm long, it might be necessary to use rod shaped particles in these studies.

CHAPTER V

CONCLUSIONS AND FUTURE DIRECTIONS

In the current study, we first applied dielectrophoresis to pattern the deposition of actin filaments and manipulate motile actin filaments during a motility assay. Even though the maximum force that can be applied using this technique is an order of magnitude lower than motor forces, the torque due to DEP was capable of aligning the filaments during motility. Moreover, dielectrophoresis as a technique for patterning and maneuvering filaments is an important step towards biomolecular integration with NEMS. By applying physiologically relevant flow induced drag forces to align filaments and direct motility, we showed that drag forces might be crucial in the organization of cytoskeletal filaments and motor proteins within the cell. Drag forces can act on filaments when they are transported and arranged by motors (mitotic spindle formation) or due to cytoplasmic flow (formation of pseudopodia). The maximum drag force applied was gain an order of magnitude lower than motor forces. However, these moderate forces created torque on the long actin filaments that steered motile filaments and directed their motility. More over, the capability to incorporate a motor filament motility assay is important from a nanotechnology perspective. There is an increasing interest towards building on-chip, integrated, biomotor-based analytical system where, a single device consists of control electronics, chemical and physical barriers, all typically integrated in microfluidic channels. Further integration of biomotor functionality in microfluidics and control electronics may play an important role in using filaments as transport, separation and force sensing systems in micro total analytical systems. Studies of cytoskeletal systems based on motor filament interactions require higher forces than obtained by the techniques we used. When multiple motors interact with a filament, for example, kinesin and dynein with microtubules, the mechanism by which the motors switch on and off and take turns to interact with the microtubule is of great interest. It is hypothesized that this

role change by the motors could be triggered by a force feed back mechanism. To corroborate this hypothesis, it would be required to apply forces of the order of tens of pNs for long periods of time to a large population of interacting motor-filament systems. Magnetic traps can apply force to a large population of magnetic beads attached to filaments or motors and can apply force of the order of nano Newtons. Forces can be applied for long periods of time without significant heating of the biological fluids. Magnetic trap is a useful force technology to probe and answer many biological questions. Further studies will involve using this technology for studying motor filament interactions.

For any study involving cytoskeletal systems, it is pertinent to understand the inherent forces that affect these systems. Probing the rheology of complex fluids with cylindrical particles is a novel way to understand the characteristics of non-Newtonian fluids. Due to the asymmetry of the probes, their interaction with the mesh network of complex fluids is very different from that of spherical particles. In purely viscous fluids, the length of the rod contributes explicitly to the drag on the rod. However, in complex fluids the smaller diameter rod is capable of navigating through the mesh network causing a break down of the generalized Stokes-Einstein equation. On the other hand, the length of the rod interacting with the network can lead to restricted mobility. In the current study, there is a possibility of chemical interaction between the mesh network and probes. This can be prevented by modifying the probes with poly ethylene glycol (PEG). Further studies will involve using PEG-modified particles as microrheology probes.

REFERENCES

- Allen, C. and G. G. Borisy (1974). "Structural polarity and directional growth of microtubules of Chlamydomonas flagella." J Mol Biol **90**(2): 381-402.

- Amos, L. and A. Klug (1974). "Arrangement of subunits in flagellar microtubules." J Cell Sci **14**(3): 523-49.

- Ando, T., N. Kodera, et al. (2001). "A high-speed atomic force microscope for studying biological macromolecules." Proceedings of the National Academy of Sciences of the United States of America **98**(22): 12468-12472.

- Asbury, C. L. and G. van den Engh (1998). "Trapping of DNA in nonuniform oscillating electric fields." Biophysical Journal **74**(2): 1024-1030.

- Asokan, S. B., L. Jawerth, et al. (2003). "Two-dimensional manipulation and orientation of actin-myosin systems with dielectrophoresis." Nano Letters **3**(4): 431-437.

- B.Schnurretal. (1982). "MaterialsResearchSociety,Pittsburgh,." 463.

- Bausch, A. R., F. Ziemann, et al. (1998). "Local measurements of viscoelastic parameters of adherent cell surfaces by magnetic bead microrheometry." Biophysical Journal **75**(4): 2038-2049.

- Berg, J. S., B. C. Powell, et al. (2001). "A millennial myosin census." Molecular Biology of the Cell **12**(4): 780-794.

- Block, S. M., C. L. Asbury, et al. (2003). "Probing the kinesin reaction cycle with a 2D optical force clamp." Proceedings of the National Academy of Sciences of the United States of America **100**(5): 2351-2356.

- Cameron, L. A., M. J. Footer, et al. (1999). "Motility of ActA protein-coated microspheres driven by actin polymerization." Proc Natl Acad Sci U S A **96**(9): 4908-13.

- Chen, D. T., E. R. Weeks, et al. (2003). "Rheological microscopy: Local mechanical properties from microrheology." Physical Review Letters **90**(10).

- Cheney, R. E. (1998). Purification and assay of myosin V. Molecular Motors and the Cytoskeleton, Pt B. **298:** 3-18.

- Cheney, R. E., M. K. Oshea, et al. (1993). "Brain Myosin-V Is a 2-Headed Unconventional Myosin with Motor- Activity." Cell **75**(1): 13-23.

- David-Pfeuty, T., H. P. Erickson, et al. (1977). "Guanosinetriphosphatase activity of tubulin associated with microtubule assembly." <u>Proc Natl Acad Sci U S A</u> **74**(12): 5372-6.

- Delatorre, J. G., M. C. L. Martinez, et al. (1984). "Monte-Carlo Study of Hydrodynamic Properties of Flexible Linear-Chains - Analysis of Several Approximate Methods." <u>Macromolecules</u> **17**(12): 2715-2722.

- Dennis, J. R., J. Howard, et al. (1999). "Molecular shuttles: directed motion of microtubules along nanoscale kinesin tracks." <u>Nanotechnology</u> **10**(3): 232-236.

- Desai, A., A. Murray, et al. (1999). "The use of Xenopus egg extracts to study mitotic spindle assembly and function in vitro." <u>Methods Cell Biol</u> **61**: 385-412.

- Duffy, D. C., J. C. McDonald, et al. (1998). "Rapid prototyping of microfluidic systems in poly(dimethylsiloxane)." <u>Analytical Chemistry</u> **70**(23): 4974-4984.

- Duke, T., T. E. Holy, et al. (1995). ""Gliding assays" for motor proteins: A theoretical analysis." <u>Physical Review Letters</u> **74**(2): 330-333.

- Elson, E. L. (1988). "Cellular mechanics as an indicator of cytoskeletal structure and function." <u>Annu Rev Biophys Biophys Chem</u> **17**: 397-430.

- Evans, E. (1993). "New physical concepts for cell amoeboid motion." <u>Biophys. J.</u> **64**: 1306-22.

- Evans, L., T. Mitchison, et al. (1985). "Influence of the centrosome on the structure of nucleated microtubules." <u>J Cell Biol</u> **100**(4): 1185-91.

- Faretta, M. R. and B. Bassetti (1998). "Active filaments dynamics in motility assays for motor proteins: Pure and anomalous diffusion." <u>Europhysics Letters</u> **41**(6): 689-694.

- Fricke, H. and H. J. Curtis (1937). "The Dielectric Properties of Water-Dielectric Interphases." <u>Journal of Physical Chemistry</u> **41**(5): 729-745.

- Fukui, Y. and S. Inoue (1997). "Amoeboid movement anchored by eupodia, new actin-rich knobby feet in Dictyostelium." <u>Cell Motility and the Cytoskeleton</u> **36**(4): 339-354.

- Gardiner, C. W. (1983). <u>Handbook of stochastic methods</u>, Springer-Verlag.

- Gibbons, F., J. F. Chauwin, et al. (2001). "A dynamical model of kinesin-microtubule motility assays." <u>Biophysical Journal</u> **80**(6): 2515-2526.
- Gittes, F., B. Mickey, et al. (1993). "Flexural rigidity of microtubules and actin filaments measured from thermal fluctuations in shape." <u>J Cell Biol</u> **120**(4): 923-34.

- Goodman, A., Y. Tseng, et al. (2002). "Effect of length, topology, and concentration on the microviscosity and microheterogeneity of DNA solutions." J Mol Biol **323**(2): 199-215.

- Green, N. G. and H. Morgan (1999). "Dielectrophoresis of submicrometer latex spheres. 1. Experimental results." Journal of Physical Chemistry B **103**(1): 41-50.

- Guyon, E., J.-P. Hulin, et al. (2001). Physical Hydrodynamics, Oxford University Press.

- Hess, H., J. Clemmens, et al. (2001). "Light-Controlled Molecular Shuttles Made from Motor Proteins Carrying Cargo on Engineered Surfaces." Nanoletters **1**(5): 235-239.

- Holzwarth, G., K. Bonin, et al. (2002). "Forces required of kinesin during processive transport through cytoplasm." Biophysical Journal **82**(4): 1784-1790.

- Howard, J. (2001). Mechanics of Motor Proteins and the Cytoskeleton. Sunderland, Sinauer Press.

- Howard, J., A. J. Hudspeth, et al. (1989). "Movement of microtubules by single kinesin molecules." Nature **342**(6246): 154-8.

- Hu, Y. L., S. Li, et al. (2002). "Roles of microtubule dynamics and small GTPase rac in endothelial cell migration and lamellipodium formation under flow." Journal of Vascular Research **39**(6): 465-476.

- Huang, J. D., S. T. Brady, et al. (1999). "Direct interaction of microtubule- and actin-based transport motors." Nature **397**(6716): 267-270.

- Huang, Y. and R. Pethig (1991). "Electrode Design for Negative Dielectrophoresis." Measurement Science & Technology **2**(12): 1142-1146.

- Hunt, A. J., F. Gittes, et al. (1994). "The Force Exerted by a Single Kinesin Molecule against a Viscous Load." Biophysical Journal **67**(2): 766-781.

- Hunt, A. J. and J. Howard (1993). "Kinesin Swivels to Permit Microtubule Movement in Any Direction." Proceedings of the National Academy of Sciences of the United States of America **90**(24): 11653-11657.

- Janmey, P. A. (1998.). "The cytoskeleton and cell signaling - component localization and mechanical coupling." Physiol. Rev. **78**: 763-781.
- Jarvis, J. B., C. A. Jones, et al. (1998). "NIST Technical Note 1509." NIST Technical Note 1509.

- Jones, T. B. (1995). <u>Electromechanics of particles</u>. Cambridge ; New York, Cambridge University Press.

- Kapitein, L. C., E. J. Peterman, et al. (2005). "The bipolar mitotic kinesin Eg5 moves on both microtubules that it crosslinks." <u>Nature</u> **435**(7038): 114-8.

- Kersey Y.M., H., P.K., Palevitz, B.A., Wessels, N.K. (1976). "Polarity of actin filaments in characean algae." <u>Proceedings of the National Academy of Sciences of the United States of America</u> **73**: 165-167.

- King, G., F. S. Lee, et al. (1991). "Microscopic Simulations of Macroscopic Dielectric-Constants of Solvated Proteins." <u>Journal of Chemical Physics</u> **95**(6): 4366-4377.

- Kondo, H., S. Ishiwata. (1976). "Uni-directional growth of F-actin." <u>J Biochem</u> **79**: 159-171.

- Kriegmaier, M., M. Zimmermann, et al. (2001). "Dielectric spectroscopy of Schizosaccharomyces pombe using electrorotation and electroorientation." <u>Biochimica Et Biophysica Acta-General Subjects</u> **1568**(2): 135-146.

- Kural, C., H. Kim, et al. (2005). "Kinesin and dynein move a peroxisome in vivo: a tug-of-war or coordinated movement?" <u>Science</u> **308**(5727): 1469-72.

- Landau, L. D., E. M. Lifshitz, and L. P. Pitaevskii (1980). <u>Statistical Physics</u>. Oxford, New York, Pergamon Press
.
- Langford, G. M. (2002). "Myosin-V, a versatile motor for short-range vesicle transport." <u>Traffic</u> **3**(12): 859-865.

- Lifshitz, E. M. and L. D. Landau (1987). <u>Fluid Mechanics</u>, Butterworth-Heinemann.

- Limberis, L., J. J. Magda, et al. (2001). "Polarized Alignment and Surface Immobilization of Microtubules for Kinesin-Powered Nanodevices." <u>Nanoletters</u> **1**(5): 277-280.

- Limberis, L. and R. J. Stewart (2000). "Toward kinesin-powered microdevices." <u>Nanotechnology</u> **11**(2): 47-51.

- Litjens, P., C. I. Kroner, et al. (2003). "Cytoplasmic regions of the beta(3) subunit of intergrin alpha(IIb)beta(3) in platelet adhesion on fibrinogen under flow conditions." <u>Journal of Thrombosis and Haemostasis</u> **1**(9): 2014-2021.
- Lodish, H. F. and J. E. Darnell (1995). <u>Molecular cell biology</u>. New York, Scientific American Books : Distributed by W.H. Freeman and Co.

- Macneal, R. K. and D. L. Purich (1978). "Chromium (III)-nucleotide complexes as probes of the guanosine 5'-triphosphate-induced microtubule assembly." <u>Arch Biochem Biophys</u> **191**(1): 233-43.

- Mason, T. G. and D. A. Weitz (1995). "Linear viscoelasticity of colloidal hard sphere suspensions near the glass transition." <u>Physical Review Letters</u> **75**(14): 2770-2773.

- McDonald, J. C., D. C. Duffy, et al. (2000). "Fabrication of microfluidic systems in poly(dimethylsiloxane)." <u>Electrophoresis</u> **21**(1): 27-40.

- Mehta, A. D., R. S. Rock, et al. (1999). "Myosin-V is a processive actin-based motor." <u>Nature</u> **400**(6744): 590-593.

- Miles, J. B. and H. P. Robertson (1932). "The Dielectric Behavior of Colloidal Particles with an Electric Double-Layer." <u>Physical Reviews</u> **40**(4): 583-591.

- Miller, R. D. and T. B. Jones (1993). "Electro-Orientation of Ellipsoidal Erythrocytes - Theory and Experiment." <u>Biophysical Journal</u> **64**(5): 1588-1595.

- Montemagno, C. and G. Bachand (1999). "Constructing nanomechanical devices powered by biomolecular motors." <u>Nanotechnology</u> **10**(3): 225-231.

- Morgan, H. and N. G. Green (1997). "Dielectrophoretic manipulation of rod-shaped viral particles." <u>Journal of Electrostatics</u> **42**(3): 279-293.

- Morgan, H., M. P. Hughes, et al. (1999). "Separation of submicron bioparticles by dielectrophoresis." <u>Biophysical Journal</u> **77**(1): 516-525.

- O'Konski, C. T. (1960). "Electric Properties Of Macromolecules. V. Theory Of Ionic Polarization In Polyelectrolytes." <u>Journal of Physical Chemistry</u> **64**(5): 605-619.

- Perrin, F. (1936). "Brownian movement of an ellipsoid (II). - Free rotation and depolarisation of fluourescences. - Translation and diffusion of ellipsoidal molecules." <u>JOURNAL DE PHYSIQUE ET LE RADIUM</u> **7**: 1.

- Pohl, H. A. (1978). <u>Dielectrophoresis : the behavior of neutral matter in nonuniform electric fields</u>. Cambridge ; New York, Cambridge University Press.

- Ramos, A., H. Morgan, et al. (1999). "The role of electrohydrodynamic forces in the dielectrophoretic manipulation and separation of particles." <u>Journal of Electrostatics</u> **47**(1-2): 71-81.
- Rankin, S. and M. W. Kirschner (1997). "The surface contraction waves of Xenopus eggs reflect the metachronous cell-cycle state of the cytoplasm." <u>Curr Biol</u> **7**(6): 451-4.

- Riveline, D., A. Ott, et al. (1998). "Acting on actin: the electric motility assay." European Biophysics Journal with Biophysics Letters **27**(4): 403-408.

- Riveline, D., C. H. Wiggins, et al. (1997). "Elastohydrodynamic study of actin filaments using fluorescence microscopy." Physical Review E **56**(2): R1330-R1333.

- Smith, P. E., R. M. Brunne, et al. (1993). "Dielectric-Properties of Trypsin-Inhibitor and Lysozyme Calculated from Molecular-Dynamics Simulations." Journal of Physical Chemistry **97**(9): 2009-2014.

- Soong, R. K., G. D. Bachand, et al. (2000). "Powering an inorganic nanodevice with a biomolecular motor." Science **290**(5496): 1555-1558.

- Spiegelman, B. M., S. M. Penningroth, et al. (1977). "Turnover of tubulin and the N site GTP in Chinese hamster ovary cells." Cell **12**(3): 587-600.

- Spudich, J. A., S. J. Kron, et al. (1985). "Movement of myosin-coated beads on oriented filaments reconstituted from purified actin." Nature **315**(6020): 584-6.

- Stracke, R., K. J. Bohm, et al. (2000). "Physical and technical parameters determining the functioning of a kinesin-based cell-free motor system." Nanotechnology **11**(2): 52-56.

- Stratton, J. A. (1941). Electromagnetic theory. New York, London,, McGraw-Hill book company inc.

- Straub, F. B. (1942). Studies of the Institute of Medical Chemistry **2**: 3-16.

- Suzuki, H., A. Yamada, et al. (1997). "Control of actin moving trajectory by patterned poly(methyl methacrylate) tracks." Biophysical Journal **72**(5): 1997-2001.

- Svoboda, K., C. F. Schmidt, et al. (1993). "Direct Observation of Kinesin Stepping by Optical Trapping Interferometry." Nature **365**(6448): 721-727.

- T.G.Mason, H. G., andD.A.Weitz, (1997). J.Opt.Soc.Am: 139.

- Takashima, S., H. M. Fishman, et al. (1977). Electrical properties of biological polymers, water, and membranes. New York, New York Academy of Sciences.

- Talbott, J. W. and E. K. Stefanakos (1972). "Aligning Forces On Wood Particles In An Electric Field." Wood and Fiber **4**(3): 193-203.
- Tanaka, H., K. Homma, et al. (2002). "The motor domain determines the large step of myosin-V." Nature **415**(6868): 192-5.

- Tang, J. X. and P. A. Janmey (1996). "The polyelectrolyte nature of F-actin and the mechanism of actin bundle formation." Journal of Biological Chemistry **271**(15): 8556-8563.

- Taunton, J., B. A. Rowning, et al. (2000). "Actin-dependent propulsion of endosomes and lysosomes by recruitment of N-WASP." J Cell Biol **148**(3): 519-30.

- Theriot, J. A. (1994). "Actin filament dynamics in cell motility." Adv Exp Med Biol **358**: 133-45.

- Theriot, J. A. (1994). "Regulation of the actin cytoskeleton in living cells." Semin Cell Biol **5**(3): 193-9.

- Theriot, J. A. and T. J. Mitchison (1991). "Actin Microfilament Dynamics in Locomoting Cells." Nature **352**(6331): 126-131.

- Theriot, J. A., T. J. Mitchison, et al. (1992). "The Rate of Actin-Based Motility of Intracellular Listeria-Monocytogenes Equals the Rate of Actin Polymerization." Nature **357**(6375): 257-260.

- Tirado, M. M. and J. Garciadelatorre (1979). "Translational Friction Coefficients of Rigid, Symmetric Top Macromolecules - Application to Circular-Cylinders." Journal of Chemical Physics **71**(6): 2581-2587.

- Tirado, M. M. and J. Garciadelatorre (1980). "Rotational-Dynamics of Rigid, Symmetric Top Macromolecules - Application to Circular-Cylinders." Journal of Chemical Physics **73**(4): 1986-1993.

- Valberg, P. A. and D. F. Albertini (1985). "Cytoplasmic Motions, Rheology, and Structure Probed by a Novel Magnetic Particle Method." Journal of Cell Biology **101**(1): 130-140.

- Vale, R. D. and R. J. Fletterick (1997). "The design plan of kinesin motors." Annu Rev Cell Dev Biol **13**: 745-77.

- Valentine, M. T., Z. E. Perlman, et al. (2005). "Mechanical properties of Xenopus egg cytoplasmic extracts." Biophys J **88**(1): 680-9.

- VanKampen, N. G. (1981). Stochastic processes in physics and chemistry, North-Holland.
- Venier, P., A. C. Maggs, et al. (1994). "Analysis of Microtubule Rigidity Using Hydrodynamic Flow and Thermal Fluctuations." Journal of Biological Chemistry **269**(18): 13353-13360.

- Visscher, K., M. J. Schnitzer, et al. (1999). "Single kinesin molecules studied with a molecular force clamp." Nature **400**(6740): 184-189.

- Wanka, F. and E. J. J. Van Zoelen (2003). "Cellular organelle transport and positioning by plasma streaming." <u>Cellular & Molecular Biology Letters</u> **8**(4): 1035-1045.

- Wanka, F. and E. J. J. Van Zoelen (2003). "Force generation by cellular motors." <u>Cellular & Molecular Biology Letters</u> **8**(4): 1017-1033.

- Washizu, M. and O. Kurosawa (1990). "Electrostatic Manipulation of DNA in Microfabricated Structures." <u>Ieee Transactions on Industry Applications</u> **26**(6): 1165-1172.

- Washizu, M., T. Nanba, et al. (1990). "Handling Biological Cells Using a Fluid Integrated-Circuit." <u>Ieee Transactions on Industry Applications</u> **26**(2): 352-358.

- Washizu, M., S. Suzuki, et al. (1994). "Molecular Dielectrophoresis of Biopolymers." <u>Ieee Transactions on Industry Applications</u> **30**(4): 835-843.

- Wegner, A., and G. Isenberg (1983). "2-fold difference between the critical monomer concentrations of the two ends of actin filaments in physiological salt conditions." <u>Proc Natl Acad Sci U S A</u> **80**: 4922-5.

- Whitesides, G. M. (2003). "The 'right' size in nanobiotechnology." <u>Nat Biotechnol</u> **21**(10): 1161-5.

- Yamada, S., D. Wirtz, et al. (2000). "Mechanics of living cells measured by laser tracking microrheology." <u>Biophysical Journal</u> **78**(4): 1736-1747.

- Yildiz, A., J. N. Forkey, et al. (2003). "Myosin V walks hand-over-hand: single fluorophore imaging with 1.5-nm localization." <u>Science</u> **300**(5628): 2061-5.

- Zicha, D., I. M. Dobbie, et al. (2003). "Rapid actin transport during cell protrusion." <u>Science</u> **300**(5616): 142-145.